Characterization of lithium peroxide formation in lithium air battery electrode via titration techniques and EIS

by

Jeremiah Deboever, B.S.

Thesis

Presented to the Faculty of the Graduate School

of Oregon Institute of Technology

in Partial Fulfillment

of the Requirements

for the Degree of

Master of Science in Renewable Energy Engineering

Oregon Institute of Technology

July 2014

Final approval form

ACKNOWLEDGEMENTS

ABSTRACT

Lithium-oxygen (Li-O$_2$) batteries have attracted attention in the last decade for their remarkable theoretical energy density of 3,500 Wh kg-1 when mass of lithium and oxygen are counted which is over 10 times higher than that of conventional lithium-ion (Li-ion) batteries. However, cells have not yet demonstrated to be rechargeable as the internal reactions are highly unstable. The oxygen-rich environment in combination with a wide potential window and the presence of lithium promote uncontrolled and irreversible reactions in the cell. A fundamental understanding of the mechanisms behind the various complex reactions was the approach taken in this thesis. The targeted reaction should result in the reversible formation of lithium peroxide (Li$_2$O$_2$). Here, the characterization of Li$_2$O$_2$ formation in air electrode via titration techniques and electrochemical impedance spectroscopy (EIS) was proposed as a Master of Science thesis study. This research evaluated various carbon materials with different surface area and pore volumes and correlated it to the discharge capacity, yield of the desired discharge product (Li$_2$O$_2$), discharge-charge voltage profiles and the impedance spectra of the cell. Three testing techniques, life cycle testing, Li$_2$O$_2$ titration and EIS, provided the different perspectives on the complex chemical mechanisms in Li-O$_2$ batteries. The results of this study showed slight variation in Li$_2$O$_2$ yield across the different carbon cathodes. Furthermore, the electrolyte decomposition was confirmed to be the main factor to the overall yield. As expected, the specific capacity significantly varied from carbon to carbon and the voltage profiles were demonstrated to be dependent on the carbon cathode. Lastly, the impedance spectrum showed to correlate to the discharge capacity of the battery but not directly to the Li$_2$O$_2$ yield.

TABLE OF CONTENTS

LIST OF TABLES

LIST OF FIGURES

x

I. Introduction

The need of energy storage when using renewables rises from the variability and unpredictability of the natural sources of energy. Although multiple types of energy storage systems exist, electrochemical energy storage have been highly sought after for their versatility in implementation, high energy densities and overall efficiency.

One of the driving forces to this field has been the automotive industry with hybrid and electrical vehicles (HVs and EVs) requiring high gravimetric and volumetric energy density, high power and high energy efficiency. By taking advantage of efficient and quieter electrical motors, EVs offers a number of benefits compared to conventional petroleum-based vehicles. Emissions due to transportation are drastically diminished when recharging the energy storage system through the cleaner power of the grid. However, the limiting factors to this promising transportation change are the state-of-the-art energy density, efficiency, and life cycle of energy storage system [1]. Although subsidies from petroleum companies are still limiting the push of electric vehicles [2], the interest from consumers has recently helped raise funding for energy storage research.

As a consequence of this growing need in the automotive industry as well as within the national electrical grid, various research initiatives in the U.S. have been established over the last decade. A few programs from the Advanced Research Projects Agency - Energy (ARPA-E) within the Department of Energy (DOE) have supported research groups in energy storage across the country [3]. The Battery for Electrical Energy Storage in Transportation (BEEST) program has for objective of meet or beat the performance and price of petroleum vehicles to enable large penetration of EVs [4]. A more recent collaborative program funded by the DOE Energy Innovation Hub – Batteries and Energy Storage is the Joint Center for Energy Storage Research (JCESR) [1]. Based off the Argonne National Laboratory in Illinois, the objective of JCESR is to investigate viable research projects and bring any optimistic results as close as possible to market. To achieve this goal, a roadmap consisting of four stages (electrochemical storage concepts,

crosscutting science, systems analysis and translation, cell design and prototyping) was set to clarify viable technologies and combine efforts towards moving those technologies forward. Any projects funded by the center enter into an agreement that defy one of the academic downfalls: inter-group collaboration. Thus, the growing interest followed by various means of financial support has made the field of next generation energy storage very promising.

Prior to going into the state-of-the-art, a brief introduction of the relevant research milestones that have shaped the batteries of today is presented [5]. The first reported chemical battery was the voltaic pile developed in 1800 by Alessandro Volta. Sixty years later, Gaston Plante discussed about the first practical battery: the lead acid storage battery and it took nearly a century later for Waldemar Junger and Karl Berg to develop an alternative chemistry: the first nickel-cadmium battery [5]. While various electrochemical storage systems were being developed, Evereday Battery Company developed the first widely used 9 V battery in 1956 [5]. It is not until 1979 that John Goodenough at Oxford perfected the first lithium ion battery – Lithium Cobalt Oxide and Lithium Manganese Dioxide [5]. Besides this major scientific breakthrough, Sony was the first company to commercialize the technology. Seventeen years later, Goodenough further improved the stability of lithium ion batteries with the lithium iron phosphate battery [6]. In consequence, over the last few decades, the energy density of lithium-ion batteries have made them highly desirable for commercialization products. Over the last 35 years, their energy density has only been improving on average 5% every year and their theoretical values has been very closely approached [4, 5]. To meet future needs, efforts have been focused on the next generation of batteries – aka 'beyond lithium-ion' batteries.

Increasing the performance of electrochemical energy storage systems has been sought for a few decades by many different groups. Current graphite-based Li-ion cells have been one of the most popular chemical batteries both on the market and from the research stand point. However, the theoretical capacity of graphite (372 mAh/g [5]), even if achieved, still falls short of the possible future goals set by the US DOE and Department of Defense

2

(DOE). As a matter of fact, the current rate of capacity improvement is only 5% a year which falls short of the 2020 goal set by JCESR [1].

While lithium ion batteries have a limit on their optimization that most likely will not meet our future needs, researchers have been focused on novel chemistries beyond lithium ion batteries. The JCESR highlights four research directions that may meet future needs [1]. The first one is multivalent ion intercalation in conventional chemistries. By replacing the monovalent lithium ion with a multivalent element such as magnesium or aluminum, the capacity stored can nearly double or triple depending on the chemistry. The second concept is to replace solid electrodes with liquid solutions or suspensions. A current example of this concept are redox flow batteries. The third concept is 'designer organic molecules' used to create tailored structure-function relationships (solid electrolyte interface (SEI) layers, redox couples, etc.). The last concept highlighted by JCESR is the one this work is most focused into: chemical transformation. The objective of this approach is to investigate traditional intercalation with high energy chemical reactions. Chemistries such as sodium-sulfur, lithium-sulfur or metal-air can provide a greatly improved energy density and possibly justify the incorporation of energy storage in high energy demand technologies with weight and volumetric limitations (i.e. electrical vehicle).

A. Metal-Air Batteries

A number of currently researched chemistries for novel electrochemical energy storage have been categorized as metal-air batteries. The interest is from the highly reactive metals in air. If these reactions are controlled, a very large amount of energy can be harvested from them. Regarding alkali metals, from least to most reactive, lithium-sodium-potassium metals can undergo highly exothermic reactions when exposed to water, halogens, nitrogen, oxygen or hydrogen gas. The most commonly known is the reaction with water since alkali metals will spontaneously form a strong aqueous base (OH⁻) and hydrogen gas as shown in Eq. (1).

$$2M_{(s)} + 2H_2O \rightarrow 2MOH_{(aq)} + H_{2\,(g)} \qquad (1)$$

3
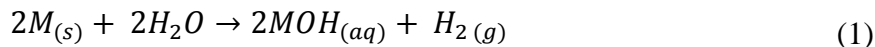
Where M is an alkali metal. The exothermic behavior of this reaction increases as we go down the group IA, thus explaining the explosive nature of the reaction with high concentration of hydrogen gas. This violent reaction with water can hardly be controlled but its effect will be discussed later in this work.

This work focuses on the reaction of an alkali metal with oxygen. When combined with this gas, the metals can form various form of oxide, peroxide and superoxide compounds, some being more stable than others. This reaction can be electrochemically controlled and the products are relatively reversible in some cases. The advantage of this reaction over conventional ionic intercalation is that it utilizes a reactant stored externally and that the reaction has a theoretical energy density not limited by a maximum ionic intercalation.

Conventional lithium ion batteries are based on an ionic intercalation principle that take advantage of the small size of Li ions (0.9 Å [8]). Used in one or both electrodes, intercalation compounds have a structure into which lithium ions can be intercalated and removed upon discharge and charge, respectively [8]:

$$xLi + M_zB_y \rightleftharpoons Li_xM_zB_y \tag{2}$$

Where M_zB_y is the transition metal compound. In other words, as the cell is being discharged, lithium ions formed at the negative electrode (anode) migrate to the positive electrode (cathode) and enter the crystalline structure of the metal compound. Upon the charging cycle, the reaction reverse and lithium ions exit the crystalline structure of the cathode material. Thus, the available intercalation sites ratio of the host material affect the overall theoretical capacity of conventional lithium ion batteries. Goodenough further discusses the difficulties associated with the lithium transport in batteries based on lithium-insertion compounds [9]. Various crystalline structures, such as layered, spinel or olivine framework structures, have been investigated to mitigate this limitation though improvement in the energy density has been limited [10].

In contrast, metal-air batteries utilizes a low packing porous carbon that allows diffusion of oxygen and leaves extensive reaction sites for discharge products to form, which increases the overall energy density of the material. Zheng et al. investigate more specifically the theoretical energy density of one of the metal-air chemistries – lithium-oxygen – in terms of the porosity of the cathode material [11]. More details on the findings of his study are discussed in the following section.

B. Lithium-oxygen Batteries

There are four chemistry architectures of lithium-oxygen batteries that are currently pursued in research: aprotic, aqueous, mixed-electrolyte and fully solid-state batteries [12]. The first three architectures have an electrolyte in the liquid form while the last one is in the solid form. Aqueous and mixed-electrolyte lithium oxygen cells are both designed to promote the reaction of lithium with oxygen in the presence of water. However, an additional layer must be used to protect the lithium from spontaneously reacting. For that reason, as well as others later discussed, the work proposed in this work will mainly focus on aprotic reactions.

The highest theoretical specific capacity of Li-O_2 cells is 3862 mAh/g_{Li} [8]. With the high voltage of 2.9 – 3.1 V of lithium, the theoretical specific energy of Li-air cells for non-aqueous exceeds 11,000 Wh/kg_{Li} as shown in Eq. (3) and (4).

$$E = \frac{V * F}{m} \tag{3}$$

Where E is the specific energy, V is the voltage of the cell, F is the Faraday Constant, and m is the molecular mass of Li. By converting one Coulomb, the equation becomes

$$E = \frac{3V * \left(96500\frac{C}{mol}\right)}{6.9\frac{g}{mol}} * \frac{1\ Ah}{3600\ C} = 11,700\frac{Wh}{kg_{Li}} \tag{4}$$

In comparison with commercial batteries, Li-O_2 batteries become an obvious interest of research even if theoretical values are not reached. However, this remarkable 10 fold increase of the energy density is only considering the weight of lithium anode without any

5

other present constraints. Thus, an adequate estimation of the theoretical energy density of Li-O$_2$ cell must take into account the weight of the electrolyte, oxygen and other battery components. Zheng et al. presented in 2008 practical maximum theoretical specific energies of 1300 Wh/kg and 1400 Wh/kg for aqueous cells where the weight of the basic and acidic electrolytes, respectively, were considered in the calculations [11]. The paper uses for comparison the practical theoretical specific energy for non-aqueous Li-air battery with an organic electrolyte at 2790 Wh/kg, which is lower than the value in Eq. (4). Nonetheless, the estimation is still a significant improvement on the state-of-the-art lithium ion batteries. This theoretical approach investigates the feasible energy density in terms of the porosity of the carbon-based air cathode – which correspond to the maximum capacity of lithium ion batteries being limited by their intercalation capabilities. Even though practical values of energy density are far from the estimated theoretical value, these estimations remain relatively high in contrast to current batteries. Experimental energy densities for the different lithium-oxygen reactions are discussed later in this report. Moreover, Zheng et al. discuss about another cell property that is especially important in lithium-oxygen cells, that is of the volumetric capacities. Based on the minimum volume of air electrode required for the electrochemical reaction to occur, the maximum calculated volumetric energy densities are 1520 Wh/L, 1680 Wh/L and 2800 Wh/L in basic, acidic and organic electrolyte, respectively [11]. However, Almaden Institute in 2009 presented a volumetric density of 3400 Wh/L for Li-air cells with organic electrolyte [13].The slight disagreement between these calculated values come from their difference in the porosity assumption (100% and 70%). More recently, a paper by Christensen et al. demonstrates that the energy densities of different reactions categorized within lithium-air batteries are not as remarkable as the improvement seen on a specific energy stand-point [7].

i.   Lithium-oxygen chemical reactions

The requirements for an electrochemical mechanism to be qualified as a Li-O$_2$ battery are that lithium cation needs to directly react with oxygen anion and that the absorbed oxygen gas is regenerated upon the reverse reaction. The nature of the reaction renders a complex

mechanism of multiple reaction phases. As previously discussed, the presence of oxygen with an alkali metal can potentially form three types of groups: oxide, superoxide and peroxide. In the present case of monovalent lithium, the following equations shows the various oxidation states [14].

Lithium superoxide:
$$2\,Li^{(s)} + 2\,O_2 \;\rightarrow\; 2\,LiO_2 \qquad \Delta G^o = -140\;kcal\;(E^o = 3.0V) \qquad (5)$$

Lithium peroxide:
$$2\,Li^{(s)} + O_2 \;\rightarrow\; Li_2O_2 \qquad \Delta G^o = -145\;kcal\;(E^o = 3.1V) \qquad (6)$$
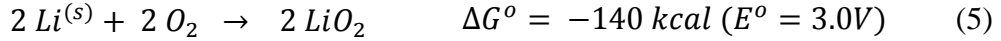
Lithium oxide:
$$2\,Li^{(s)} + \tfrac{1}{2}\,O_2 \;\rightarrow\; Li_2O \qquad \Delta G^o = -139\;kcal\;(E^o = 2.91V) \qquad (7)$$
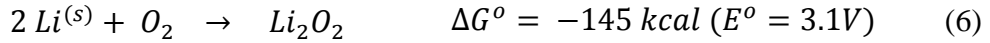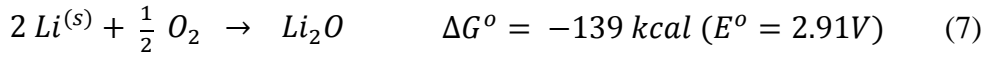
The kinetics of the oxygen reduction reaction (ORR) upon discharging is crucial to interpret any reaction mechanisms. Lithium superoxide (Eq. (5)) has recently been demonstrated to be an intermediate by Peng et al. [15]. Superoxide in the presence of lithium ions is unstable and thus disproportionates or further reduces electrochemically as follows [14]:

$$2\,LiO_2 \;\rightarrow\; Li_2O_2 + O_2 \qquad (8)$$
$$LiO_2 + Li^+ + e^- \;\rightarrow\; Li_2O_2 \qquad (9)$$
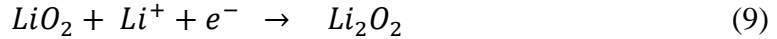
Experimental work has been published showing lithium peroxide has intermediate species to the peroxide formation demonstrating the described reaction mechanisms [16].

ii.   Literature Review

Prior to going into a review of the literature, the most influential publications are discussed to illustrate the development of the state-of-the-art. A lithium-oxygen-like battery was first observed in 1996 when Abraham et al. witnessed an increase in capacity in a lithium ion pouch cell [17]. He later noticed that a tiny pinhole in the cell was allowing oxygen to enter the cell and react with the lithium. Nearly a decade later, Read further investigated the reaction to discover the effect of oxygen diffusion on the rate capability and discharge capacity [18]. The same year, Peter Bruce and his group investigated the oxygen evolution in the aprotic lithium oxygen cell to confirm the reversibility of lithium peroxide [19]. The

last research milestone of the lithium oxygen reaction was in 2010 when Mizuno et al. questioned the formation of lithium peroxide in carbonate-based electrolyte solvent [20]. After analyzing the discharged products, carbonate species (lithium carbonate and lithium alkylcarbonate) were obtained correlating with a wide voltage gap between the discharge and charge plateaus and the formation of relatively irreversible products. Additional papers have been reviewed in this section to give a brief overview of each component comprised in a Li-O_2 cell, as demonstrated in Figure 1.
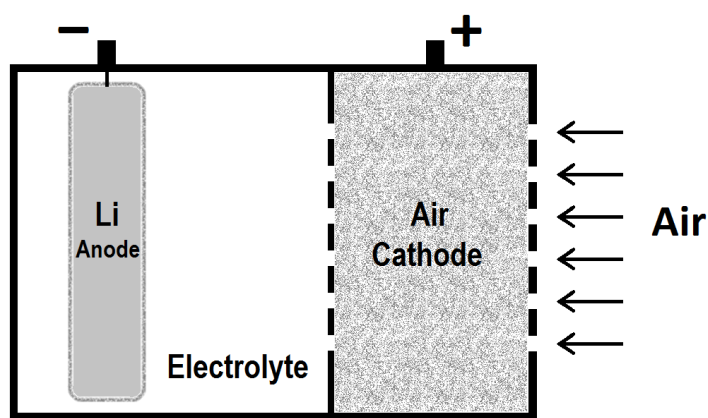
Figure 1: Fundamental structure of Li-air batteries

Lithium Electrode (anode)

Typically, lithium oxygen cells have a metallic lithium flat disc for the negative electrode as a source of lithium ions. During the discharge, lithium salts from the electrolyte provide a medium for the Li^+ to transfer between the two electrodes. The electrons travel through the electrical connection to the cathode and reduce O_2 to form lithium peroxide. Although a safety concern, the presence of lithium metal in a battery acts as the required source of ions for the reaction to occur. Commercialization of the battery will require an optimization of the size of the lithium metal to increase the safety of the technology without hindering the chemical reaction. Thus, the use of excess lithium metal allows focusing on the reactions at the cathode to establish a reversible system.

8

Nevertheless, research is still being pursued on the lithium electrode for the broader category of Li metal batteries [21]–[23]. Lithium degradation and dendrite formation are two common concerns in Li metal batteries. With high number of cycles, the progress of dendrites can create short-circuits between the cathode and the anode [24]. Furthermore, electrolyte incompatibility may lead to the formation of a resistive film barrier onto the anode [24] and reduce the diffusion of lithium ions. These two issues affect the cycle life and safety of the battery [24]. Although $Li-O_2$ batteries are comprised in the Li metal batteries category, the stability of the cathode and electrolyte are the current limitations in $Li-O_2$ batteries that must first be addressed.

Electrolyte

Fundamentally speaking, batteries require to have a layer between the positive and negative electrodes. The key properties of this separating layer can be summarized as electrically insulating, chemically inert to the electrodes and ionicaly conducting. Thus, in liquid electrolyte batteries, the layer is often comprised of a porous insulating separator and a liquid electrolyte. The latter is often composed of a solvent and a salt to create a good interconnection between the two electrodes and to allow the essential transfer of ions across the layer, respectively. Subject of a number of studies, the electrolyte composition has shown to have a large effect on the reaction in the cells and directly affect its reversibility [1]. Due to the large potential window that the lithium-oxygen cell operate at (2.0 V – 4.5 V) and presence of oxygen, decomposition and alteration of the electrolyte one of the causes that decreases the cell capacity with increasing number of cycles. Many approaches to the issue have been investigated (different solvent compositions, salt concentrations, small voltage window testing conditions, reduction of potential window using a catalyst, etc) thought no break-through have been discovered.

The current compositions of liquid aprotic electrolytes can be categorized into carbonate-based, ether-based, amide-based, sulfoxide-based and ionic liquids. Jake Christensen et al. extensively elaborated on the two categories in the review published in 2012 [7]. Multiple publications are reviewed concluding that carbonate solvents are intrinsically not suitable

for reversible reactions [7]. Side reactions (i.e. lithium carbonates formation) through the first discharge process are disadvantageous to the battery since these reactions are often irreversible and thus consume electrolyte [25]. Moreover, their non-reversibility and insulating effect are disadvantageous for the lithium-oxygen reaction.

Ether-based, amide-based and sulfoxide-based solvents have shown more promise towards developing a reversible reaction in Li-oxygen battery. Three types of solvents are explored in Christensen et al.'s review [7]: ethers, ionic liquid, and acetonitrile. Ether-based solvents (i.e. dimethoxyethane or DME) were demonstrated in the report as unsuitable solvents to achieve a reversible reaction though further research with lower charging currents is recommended before removing ethers as a possible solution. Controversially, recent research from different stand-out active research groups [19, 25–29] continue to utilize ether-based solvents such as DME or other glymes to improve the properties of Li-O$_2$ cells.

N,N-dimethylacetamide (DMA) was recently demonstrated to "resist chemical degradation" in the harsh environment of the O$_2$ [28]. Although providing a remarkable quality that few other solvents have, straight-chain alkyl amides solvents are often affected on the lithium side of the battery due to the unstable solid-electrolyte interphase (SEI) they create on the lithium anode [28]. However, the report discusses how the addition of lithium nitrate salts stabilizes the SEI layer. With test cells reaching over 80 cycles at a current density of 0.1 mA/cm^2, the presented results demonstrate a possible viability of using amide-based solvents in Li-O$_2$ batteries. Similarly, DME is another solvent that has shown to form lithium peroxide upon discharge in a relatively reversible manner [30]. Glyme-based electrolytes have shown to have a relatively stable chemistry that do not require an additive to stabilize it in lithium-air batteries [14, 15, 27, 31, 32]. Moreover, solvents with low donor number such as tetraethylene glycol dimethyl ether (TEGDME) are more prone to fully reduce O$_2$ to O$_2^{2-}$ [14].

Electrolyte salts have also shown to have an effect on the stability of the cells [27]. A research by Nasybulin et al. shows the different performance of salts in a 1.0 M glyme-

based electrolytes (TEGDME and BDG)[27]. Seven salts were assessed using TEGDME as the electrolyte solvent and KetjenBlack as the carbon electrode. The study investigates the cycling capacities of the first 20 cycles of each samples and it was found that LiTf and LiTFSI salts offer the best cycling behavior in this system [27].

Air Electrode (cathode)

The air electrode in lithium oxygen batteries must be designed with certain aspects to facilitate the reactions. It needs to be an electrically conductive, high surface area, chemically stable, and porous to allow fast oxygen diffusion to the reaction sites. Different materials, such as porous gold or various morphologies of carbon, have been investigated to provide those capabilities [33, 34]. Although porous gold has recently been demonstrated to have better reversibility, carbon-based materials have been applied the most in lithium oxygen batteries because for their light weight and high surface area. Thus, this study will focus on the carbon-based cathodes to better understand the electrochemical reaction. Composed of a carbon and a polymer binder, the material composition of the air electrode has attracted a lot of attention in the early development of $Li-O_2$ cells. The specific properties of the different carbon material have shown to be the most important factor in the value of the initial discharge capacity of the batteries. With extensive progress in that direction, the cyclability of the cells while maintaining a high capacity has lately been of interest and stability of the electrolyte has been the focus in the last five years [27].

A variety of carbon material has already been investigated for their first discharge capacity and the number of cycles at which they retain an acceptable capacity. Super P®, Ketjen Black, Graphites, Carbon NanoTubes or active coal have been explored under different conditions assessing their performance [5, 35]. Other types of carbon have also been studied and demonstrated in the literature, such as Shawinigan black, acetylene black or Black Pearls 2000 though their inferior performance has excluded them as plausible candidate [35].

Although it is obvious that decomposition of the electrolyte has a large effect on the overall reversibility of lithium-air batteries, the effect of the carbon material on the electrolyte is a topic that has just recently been addressed in the literature [31], [33]. A common observation from the early investigations of the various carbon materials suggests that high surface area carbons – such as KentjenBlack – have a higher first discharge capacity than a low surface area carbon – such as graphite or Super P. However, high surface area carbons have mesoporous structures with various chemical functionalities on the surface that are reactive. Thus, the discharge capacity and reversibility of the battery is not only related to the surface area but also to the chemical nature of the carbon material [37, 38].

iii.   Current limitations

The lithium-oxygen battery has great potential to revolutionize the way energy is stored; however, the technology is far from commercialization. The state-of-the-art have demonstrated lithium-oxygen batteries on an experimental and practical level [38] but none have shown practical lifespan. The high energy of the Li reaction with O_2 benefit the system by providing high energy density but also hinders the technology by not being stable. The oxygen reduction reaction (ORR) and oxygen evolution reaction (OER) generate corrosive species that affect the stability of the electrolyte and cathode material. These side reactions can occur and form side products that cannot be easily cycled. For that reason, carbonate-based electrolytes were found to be unsuitable in lithium-oxygen batteries. The cathode material has also been discussed to decompose and form lithium carbonate [39]. Many researches have concluded that carbon-based cathodes are relatively unstable and that an alternative material is required to obtain a reversible system [15, 25, 33, 34].

Five considerations were suggested to better understand the reaction mechanisms and to advance the technology [40]:

1) The chemistry is highly reactive and may never be completely reversible. However, a sufficiently stable system (little decomposition of electrolyte) is what should be sought after.

12

2) Understanding the nature of the degradation products is quite important. Optimization of the Li-O$_2$ battery performance will not be possible without a better understanding of the chemistry.

3) Carbon may not be the appropriate cathode material as it decomposes to lithium carbonate. Lithium carbonate is not promoted in gold-based electrodes.

4) A mediator that reduce the impedance of lithium peroxide can drastically improve the overall reaction and the cyclability of the cells.

5) Finally, the last approach to advance Li-O$_2$ cell chemistry that should be pursued is the CO$_2$ and H$_2$O tolerance with this chemistry as obtaining a very high purity of oxygen supply will be a challenge in a realistic system.

C. Scope of work

The direction that this work focuses on is understanding of the nature of products in lithium oxygen batteries and their degradation. More specifically, the work focuses on the characterization of the desired discharge product, lithium peroxide, to further understand the reaction mechanisms as a function of the carbon structure used in the air cathode. Three questions delimits the scope of work of this master's thesis:

How does the property of the carbon used in air cathodes affect the discharge capacity and voltage profile of lithium oxygen cells?

The properties of the carbon material used in lithium oxygen batteries have shown to affect the discharge capacity of the battery [34]. The proposed work is to investigate the relationship between the discharge capacity as well as the voltage profile of the cell in terms of the carbon material. A range of carbon properties (surface area and pore volume) are assessed in identical testing conditions.

How is the morphology of the carbon used in air cathodes affecting the lithium peroxide yield in lithium oxygen cells?

The yield of lithium peroxide has been demonstrated to vary between different electrolyte compositions and some carbon materials [39]. The proposed work

assesses how their morphology and properties affect the yield of Li2O2. Tubular, porous and planar carbons are assessed in identical testing conditions.

Can the cycling performance and Li_2O_2 yield be related to the impedance spectroscopy data?

The different discharge products evolve as a Li-O_2 cell is cycled and characterizing those products cannot be done without terminating the sample. The proposed work collects impedance measurements and assesses any correlation with the performance and elecrochemical yield of Li_2O_2 in the cell. Furthermore, the impedance of batteries with different carbons will also be assessed.

Three techniques will be utilized to investigate these questions: galvanostatic cycling, Li_2O_2 titration and electrochemical impedance spectroscopy (EIS). The titration technique in conjunction with the galvanostatic cycling will help assess the performance of the different carbons and EIS will provide insights on the impedance evolution due to the discharge products. Further information on each of these techniques can be found in the Experimental Work section. Prior to conducting this fundamental study, a laboratory station was established at the Oregon Tech. Wilsonville campus. A significant amount work was allocated in setting up the equipment and properly calibrate them to validate any work pursued in the laboratory.

The following chapter will cover the equipment established in the laboratory as well as the process to prepare each sample used in this study. The sample preparation methods and testing procedures are detailed in the Experimental Work chapter. The results produced during this study are categorized by testing techniques in the Results chapter and are correlated between one-another in the Discussion chapter. Finally, the contribution to the literature and future work is discussed in the Conclusion chapter. Additional practical documentations collected during this study can be found in the Appendices chapter.

II. Experimental Setup

A tangible outcome from the presented work is the establishment of a versatile laboratory station at the Wilsonville campus. Through the help of various funding sources, new equipment was acquired for direct use in this project. The recent relocation to new campus facilities required laboratory equipment to be re-calibrated and outfitted to the current need. Thus, this chapter discusses the design decision made to establish the battery research laboratory station. Although the presented work is focused on the lithium-oxygen cells, the laboratory station was set up to accommodate various types of batteries, fuel-cells or capacitor research.

A. Cathode Preparation Instruments

In battery fundamental research and more specifically in lithium-oxygen cells, a large amount of work goes in the preparation of electrode materials (cathode in the case of Li-O_2). Commonly, a 'slurry' of active material is created and applied to a substrate that acts as a current collector. Once dried, the final product can be used to be assembled in a cell. As one may expect, the material composition as well as the process in combining them has a crucial effect on the performance of the sample when tested.

To prepare a porous carbon cathode, the carbon material is crushed into a fine powder and mixed with the binder and solvent using a homogenizer. Once mixed, it is common to have slurry buildup on the sides of the vial in which it was mixed. This can affect the homogeneity of the slurry. By putting the vial in an ultrasonic bath, the buildup will settle back at the bottom of the vial. After layering the slurry onto a substrate, the cathode is placed in a vacuum oven where moisture is removed from it. The composition of the various slurries and the methodology is discussed in Chapter III as this section highlights the capabilities of the instruments used.

i. Homogenizer

In the slurry preparation for cathodes, a thorough mixing of the materials is crucial to create a more homogeneous suspension. Three compounds with specific purposes are required to

make lithium-oxygen cathode slurries: an active carbon, a binder and a solvent. A carbon powder is combined with a binder to appropriately create a stable layer that can withhold mechanical stress. The use of solvent in the process allows dissolving binder to create a more thorough homogeneity of carbon/binder composite on the nano-scale after the solvent evaporation. The use of high speed mixer can acquire the homogeneity required with high viscosity solutions.

A laboratory grade homogenizer is specifically designed to provide high-energy mixing that is capable of creating a relatively uniform slurry. Designed to operate between 500 and 25,000 rpm, the equipment is engineered to mix viscous suspensions that other instruments would not be able to (i.e. magnetic stirring bar). Figure 2 illustrates a commercial homogenizer capable of mixing at speeds up to 24,000 rpm.

Figure 2: IKA T-18 Basic Homogenizer commercially available from Cole Parmer.

By reverse-engineering this laboratory grade instrument, an alternative was found to achieve similar capabilities for a 10th of its cost. A variable speed Dremel operating between 5,000 rpm to 25,000 rpm provided the correct framework to a custom laboratory tool. A mixing bit was manufactured with a $1/8^{th}$ in. dia stainless steel rod to match the same design as the internal rotating bit from the homogenizer (Figure 3, right). The static outer tube found on the homogenizer was manufactured out of a $1/4^{th}$ SS tube and a $3/8^{th}$

16

hole was drilled through the side to provide a powerful fluid mechanics flow. However, securing the static outer tube in a perfectly aligned manner was found to be challenging and the contacts between the rotating bit and the tube created undesired particles in the mixture, as seen in the two translucent samples in Figure 4. Thus, the outfitted Dremel was tested with the rotating bit alone and adequate results were found in relatively lower viscosity solutions. For ease of use, the Dremel homogenizer was secured to a stand as shown in Figure 3, left. Additionally, a hot plate was placed underneath to provide heating capabilities – which reduces the solution viscosity.
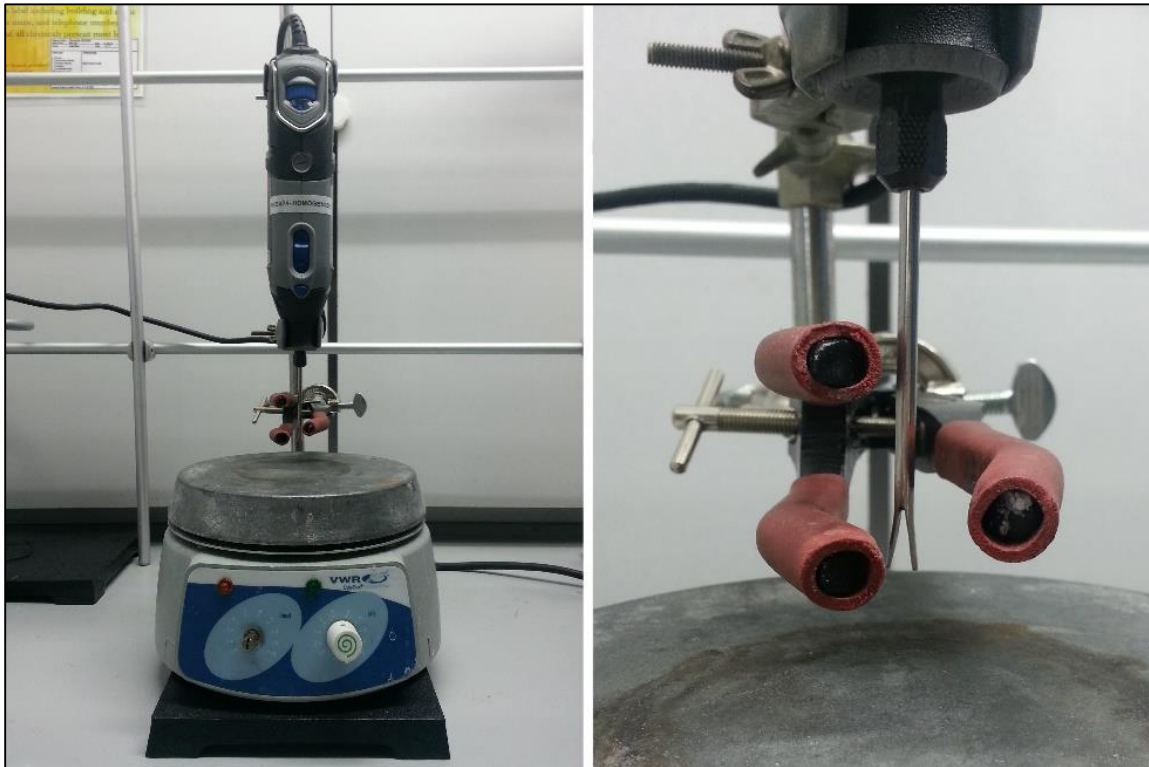
Figure 3: Custom Homogenizer. Outfitted Dremel on its stand (left). 1/8th SS mixing bit (right).
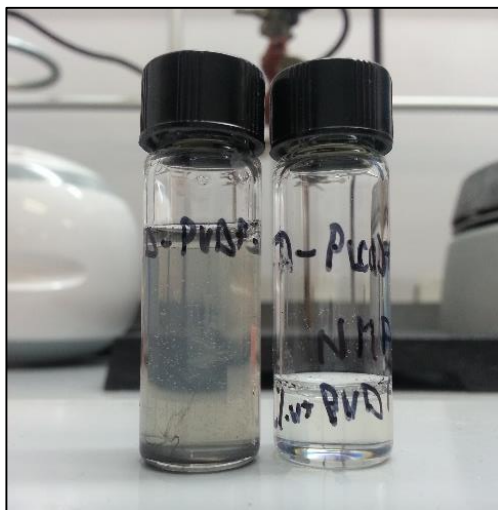
Figure 4: Binder solutions showing the introduction
of impurities when a 1/4" SS guard was used.

ii.   Ultrasonic bath

The purpose of an ultrasonic bath or sonicator) in the cathode preparation is to reduce the accumulation of slurry on the walls of a vial that could potentially alter its concentration. The instrument exposes the sample in a distilled water bath to vibrations over 20 kHz. This settles any build-ups and insures that the entirety of the slurry composition is homogenously mixed. A jewelry cleaner was found to provide similar capabilities to a laboratory-grade sonicator, as shown in Figure 5.

iii.   Vacuum oven

The last equipment addition discussed in the cathode preparation sub-section is a laboratory grade vacuum oven. As the presence of moisture in lithium oxygen cells has a drastic negative effect (discussed in details later), the combination of heat and low pressure allows to effectively remove moisture from electrodes and other components of the cells. A Shel Lab SVAC1 vacuum oven connected to a stand-alone rotary vacuum pump (Figure 6) allows to dry electrodes at vacuum levels of -29.8 inHg and temperatures up to 200 °C. Additionally, the oven was connected to high purity argon (99.998 %, refer to the specification sheet in the appendix) gas to reduce the exposition of electrodes to moisture when transferred to the glovebox.

Figure 5: Ultrasonic Bath.

Figure 6: Vacuum Oven for electrode drying.

B. Controlled Environmental Chamber (glovebox)

Due to the nature of this research, a controlled environmental chamber was established to reduce the decomposition of the materials as well as protect specific chemicals from moisture and oxygen. Storing metallic lithium as well as anhydrous electrolytes in an inert environment has provided longevity to the chemicals as well as enhanced laboratory safety. To serve that purpose, the VGB-3 MTI glovebox – previously acquired by the university – was put in proper working order. The initial approach of contacting the manufacturer to acquire documentation on the VGB3 was unsuccessful as MTI has not been recently retailing this system. Furthermore, the company was not able to provide any user manuals or specification sheets on the VGB3 glovebox. Thus, this sub-section discusses the design decisions that led to a fully working system.

i.   Custom Gas Connection

The foremost design made on the glovebox is the gas flow layout. Highlighting simplicity and practicality, the gas connection is based on multiple commercial design from various

manufacturers (MBraun, Inc, Innovative Technology, Inc.,…). As state-of-the-art commercial system features a purification system that continuously recirculate and purify the inert gas, this glovebox system is designed to operate more closely to a purge box (system requiring significant purging to maintain adequate levels of purity). Thus, the gas connections were designed to maximize the use of the gas while still maintaining this high level of purity.

The layout is designed to take advantage of the operating pressures of the working and transfer chambers as well as the pressure of the gas supply, as shown in Figure 7. By design, the working chamber pressure is set slightly higher than the atmosphere to encourage possible leakage outward. Also by design, the transfer chamber is placed under vacuum to maintain a good seal on the isolating doors. Finally, the gas supply is set to be three times the working chamber pressure to be able to provide enough back pressure in the case of a large leak. Therefore, the gas flow is designed to flow from the gas supply to the working chamber and finally to the transfer chamber. A vacuum pump is used to maintain a low absolute pressure inside the transfer chamber outputting the inert gas to the atmosphere.

Gas Supply
300 kPa

Isolating
Doors

Working Chamber
101.8 kPa

Transfer
Chamber
1.0 kPa

Atmosphere
101.0 kPa

Glove Ports
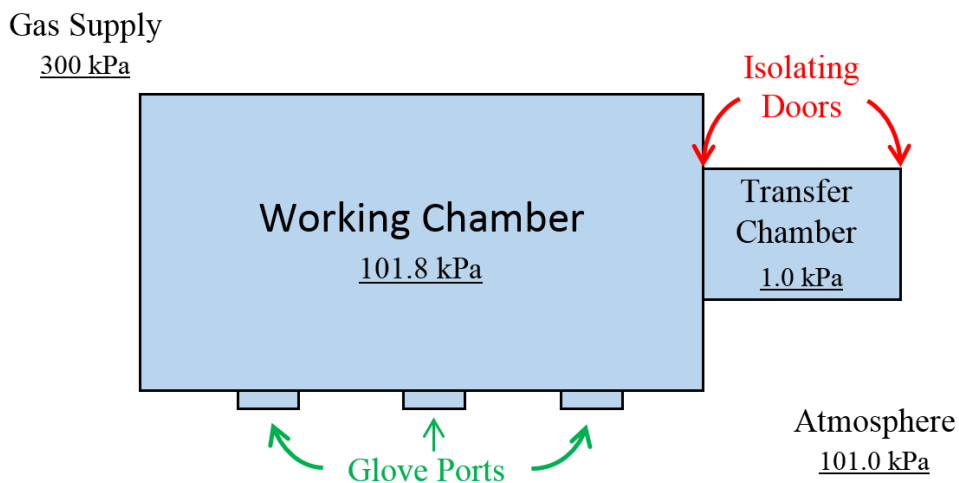
Figure 7: Simplified glovebox layout with working pressures.

To maintain a positive pressure in the working chamber, an automatic pressure controller (EQ-KJT-2V, MTI) packaged from MTI is placed in line with the gas flow. A pressure transducer (TG22-08, STNC Inc) is used to measure the pressure inside the working chamber with 0.1 kPa accuracy. The feedback is sent to a controller (AL-501, Yudian Automation) that operates two solenoid valves placed on the gas supply and between the working chamber and the transfer chamber. This configuration utilizes the positive pressure of the gas supply and the negative relative pressure of the transfer chamber to maintain the working pressure within a set boundary. The controller can be programmed to operate within a comfortable pressure during use and at higher pressure when the system is idle. Furthermore, the controller also features alarms and output channels that can be used in the future to further automatize the gas supply system.

Another key feature of this custom gas flow system is the 2 three-way valves on the gas supply and the transfer chamber. A three-way valve is used for the argon gas supply to allow line purging capabilities without introducing air to the working chamber, as shown in Figure 8. As gas tanks need to be periodically changed, it was important to design the connection to be purged before reconnecting it to the glovebox. Similarly, a three-way valve is placed between the working chamber and the transfer chamber to manually control the transfer chamber pressure, as shown in Figure 9. This valve is placed in parallel with the solenoid valve from the automatic pressure controller to avoid interfering with one another.

All the gas connections are designed with Swagelok compression fittings to reduce the chances of leaks. The connection on the solenoid valves from the automatic pressure controller were replaced with ¼" SS tubing compression fitting and a compression fitting adapter was placed in-line with the vacuum pump to also provide versatility. The following figure (Figure 10) recapitulates the piping and instrumentation diagram (P&ID) of the glovebox system. Technical drawings such as the glovebox mechanical sketch and P&ID drawing can be found in the appendix.
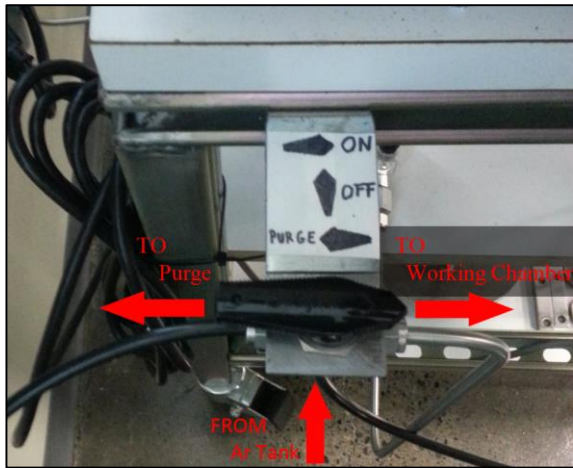
Figure 8: Three-way valve used to purge the lines before connecting a new gas tank. Currently allowing flow from the Ar tank to the working chamber.
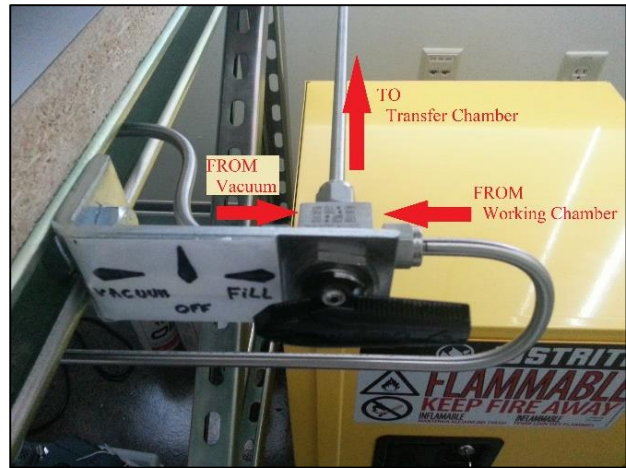
Figure 9: Three-way valve used to manually control the transfer chamber pressure. Currently allowing the flow from the vacuum pump to the transfer chamber.
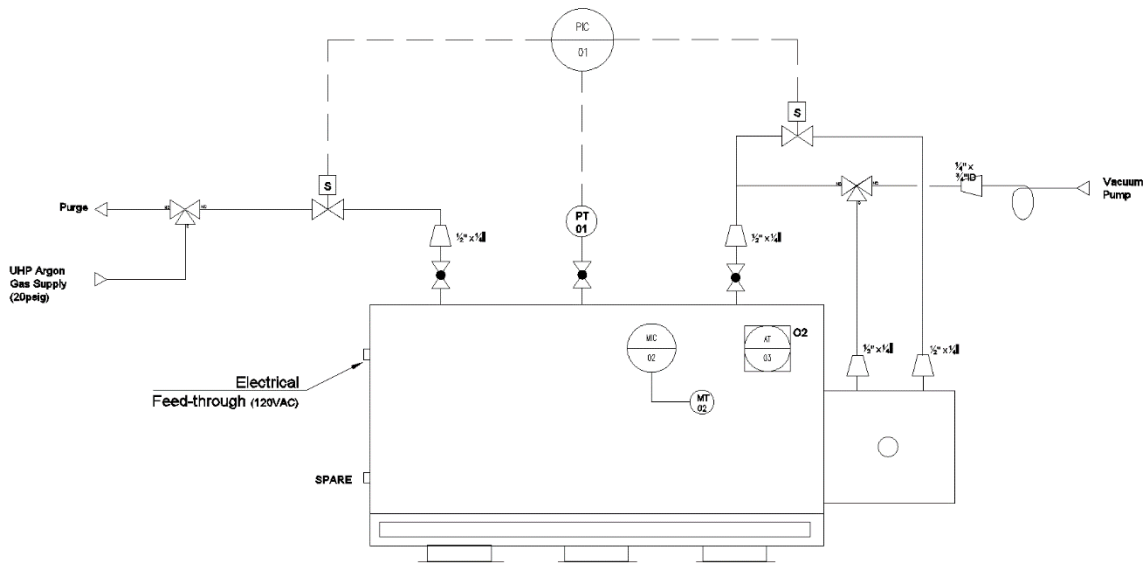
Figure 10: Piping and Instrumentation Drawing for the inert gas system

ii.   Gas Monitoring Instruments

Two instruments were added to the glovebox system to monitor the inertness of the environment. An oxygen and a moisture sensor allows to accurately measure the concentrations in the glovebox to preserve cell components such as lithium metal,

electrolyte, salts or dried cathodes. The addition of these two instruments has been crucial in the operation and condition of the glovebox.

An oxygen sensor from Omega Alpha (Series 3000 Trace Oxygen Analyzer) is used to monitor the oxygen concentration within three auto adjusting ranges: 0 – 100 ppm (0.01 %), 0 – 1,000 ppm (0.1 %) and 0 – 10,000 ppm (1 %). Based on a similar concept as fuel cells, a constant gas flow passes by a membrane that reacts with the oxygen to generate a current signal. This feedback is then used to output a reading on the display. An optional pump was acquired with the instrument to insure the proper gas flow through the sensor. The instrument is a stand-alone system with the capability to be installed externally (1/4" compression fitting). However, the output of the pump was designed with a hose barb that would be fed back to the glovebox. To avoid uncertainties with the measurement and reduce the possibilities of leaks, the instrument was located inside the working chamber. In addition, the instrument was placed by the gas outlet furthest away from the fresh gas supply to measure the highest oxygen concentration possible. Alarms with output signals are accessible on the sensor to incorporate the instrument in the automation of the overall glovebox.

The second instrument used to monitor the gas purity inside the working chamber is a moisture sensor packaged from MTI (EQ-RH-800). A dew point transmitter (EA2-TX-100, Mitchell Instruments) uses impedance technology to measure the moisture concentration in a gas. A hygroscopic single layer between a permeable gold film and a base electrode has moisture dependent impedance that is characterized to accurately measure moisture. Programmed to measure concentration from 0.1 to 999.0 ppm of moisture, the sensor outputs a 4-20 mA signal that is then read by a controller (AL-501, Yudian Automation). Again, the controller features two sets of alarms and outputs that can be used in the future to automatically control gas supply. The sensor was originally designed to simulate its designed location inside a recirculating system with constant gas flow by being placed in-line between the working chamber and the transfer chamber. It was quickly observed that the high velocity and sporadic gas flow made the moisture

reading erratic. Thus, the instrument was placed inside the working chamber and secured next to the gas pump outlet of the oxygen sensor. The estimated gas flow speed by the sensor is slightly lower than the recommended speeds though only the response of the reading is affected by it. Further testing is discussed in the following section.

iii.   System Performance Improvements

Various design decisions were made to medicate gas leaks and high concentration of oxygen and moisture in the glovebox. Although documentation was not available, technicians and engineers at MTI Corp assumed that the VGB3 glovebox is not intended for lithium battery research because it was not designed to obtain low moisture and low oxygen concentration. The challenge of making the glovebox system as air-tight and low-diffusion as possible encouraged understanding physical phenomenon on a molecular level (i.e. partial pressures and Venturi effect on a molecular level). Since the working chamber is operated at positive pressure, one may omit the partial pressure of individual gases. As oxygen concentration decrease in the chamber, the pressure difference between the atmosphere and the chamber increases to the point that an absolute oxygen-free chamber will have a 3.09 psi gradient with the outside. Thus, diffusion as well as a Venturi effect of small leaks will have the tendency to increase the oxygen in the working chamber.

The most obvious leak-prone component of the system is the flexible gloves. The original set of gloves that were installed on the glovebox was made out of natural rubber. However, this material is not recommended for high gas impermeability and not compatible with certain chemicals [41]. Thus, a set of butyl ambidextrous extra-long gloves – the industry standard material – was installed on the three front glove ports to reduce the gas ingress. Additionally, butyl gaskets were placed on the three back glove ports for the same purpose. These additions showed drastic improvements on reducing leaks in the system when pressure was observed to be maintained overnight at the maximum gauge pressure (15 mbar or 1.5 kPa). Consequently, the rate of constant oxygen concentration increase associated with partial pressures was reduced from > 10 ppm/hr to below 1.5 ppm/hr.

24

After witnessing a relatively high moisture concentration inside the glovebox that was only reduced with a large quantity of purging gas (3X the volume of the glovebox), an active desiccant filter was designed to capture the moisture present in the environment. Commercially available glovebox recirculation system have a cost of a minimum of $10,000 featuring active moisture and oxygen purification systems. Using the system on campus, it was found that oxygen concentration has been able to be brought down to acceptable ppm level by purging with high purity argon gas. However, this method was found to be ineffective with the moisture present inside the system suggesting that moisture was not coming from outside the glovebox alone.

The first approach to resolve this concern was to leave a layer of molecular sieve exposed in the glovebox for an extended period of time. However, very minimal changes in moisture concentration were observed. Thus, the following approach to the problem was to design an active moisture purification system that would provide a steady flow through a bed of desiccant. A simple sheet metal tower was constructed around a computer fan that would actively circulate the gases through a filter system. A 12 V, 0.25 A computer fan provided the correct flow rate and size needed for the project. The final solution to this issue, as shown in Figure 11, illustrate a simplistic, small and ingenious moisture purification system that can reduce the moisture concentration down to acceptable levels.
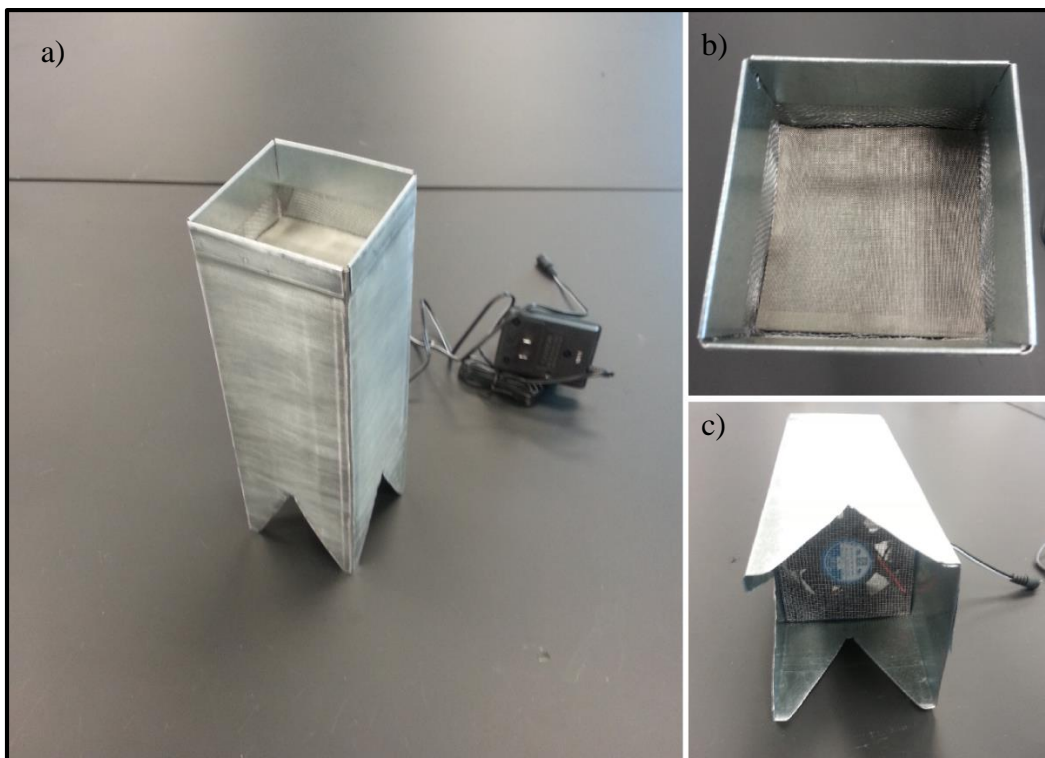
Figure 11: (a) Custom Moisture Filter System for the glovebox. (b) Metal mesh to contain the desiccant material. (c) 3 W computer fan.

The immediate results were that moisture concentration dropped down from 900 ppm_v to 350 ppm_v in one hour and the weight of the desiccant used increased after 40 hrs by 5%. The choice of desiccant material was made on a financial and design requirement basis. The common house-hold desiccant material was investigated for this system, though its inertness in the environmental chamber was questioned. Thus, the use of molecular sieves (4Å) was found to be the most appropriate desiccant. Furthermore, the benefit of molecular sieves is that they can be regenerated at high temperatures, making a virtually endless supply.

Another physical phenomenon that was sought after and resolved is the molecular weight of oxygen versus argon. The atomic weight of oxygen and argon gas are 32 g/mol and 40 g/mol, respectively. Thus, it was important to design the argon gas inlet to be located as high as possible and the outlet as low as possible inside the glovebox to circulate the

impurities in the glovebox. An internal tube was placed to direct incoming gas to a higher location (Figure 12).

Figure 12: Incoming gas redirection.

iv.   Operational Glovebox System

To conclude, the controlled environment chamber has achieved higher performance level than originally expected. Oxygen concentration has been observed as low as 40 ppm without extensive purging and moisture concentration has been maintained below 15 ppm and as low as 7.8 ppm with the desiccant filter. Gas consumption during active research has been on average 300 cu. ft. every three weeks which is remarkable when no commercial purification system is used.

A scale as well as a cutting board has been added inside the glovebox for battery assembling purposes. The Sartorius analytical lab balance (Practum124-1S, Sartorius) has both a readability and reproducibility of 0.1 mg. A layout of inside the working chamber is demonstrated in Figure 13. The new lithium metal as well as other chemicals are stored

near the incoming gas on the top left side of the picture. The sensors as well as the used chemicals are placed on the far right side of the glovebox near the gas outlet. An air-tight electrical power feed-through provides power to each of the instruments inside the glovebox.

Figure 13: Working chamber layout featuring the internal scale, the cutting pad, the desiccant filter and the O_2/H_2O sensors.

Lastly, a light fixture was designed to provide adequate lighting inside the glovebox. A simple folded sheet of metal is used to support an incandescent light without the use of any screws. A simple hook-cantilever combination allows the light to be suspended over the front glass of the glovebox, as shown in Figure 14.

Figure 14: Light fixture for the glovebox.

C. Battery Cycling Station

An 8-channel battery tester (CT2001A5V5mA, Landt Instrument) was used to cycle the batteries. To provide an ultra-high purity (UHP, 99.999%) oxygen supply to each cell, an oxygen supply system was custom-designed for the purpose.

A computer server racking frame was used to secure the oxygen supply system to the Landt Instrument battery tester. Holes in an aluminum bar helped attach each valve to the frame thus reducing torque on the fittings. To hold the cells upright, a brome holder was adapted to clamp each cell under their oxygen supply. A heat shrink used for electrical wiring was placed on each branch of the metal clamp to further reduce the chance of shorting the cell and also to reduce the damage cause when changing cells. An acrylic sheet was placed on top of the Landt Instrument to electrically insulate it from the cell and protect the instrument from any accidental leak from the cells.
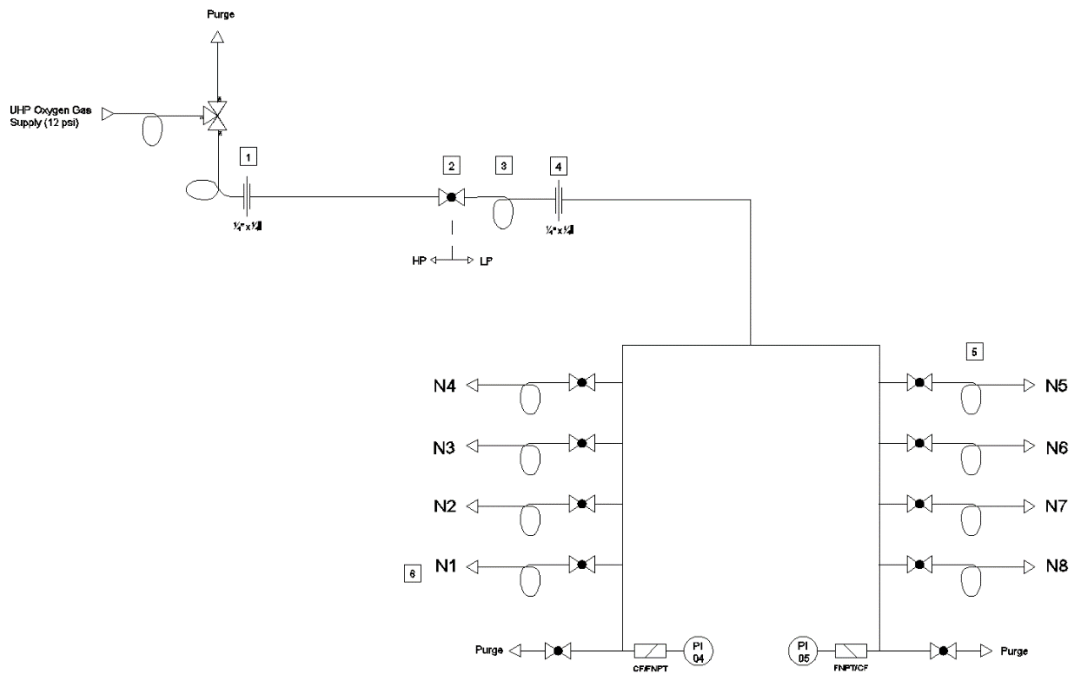
Figure 15: Oxygen supply system pipe & instrumentation diagram. Full drawing with legend may be found in the appendix.
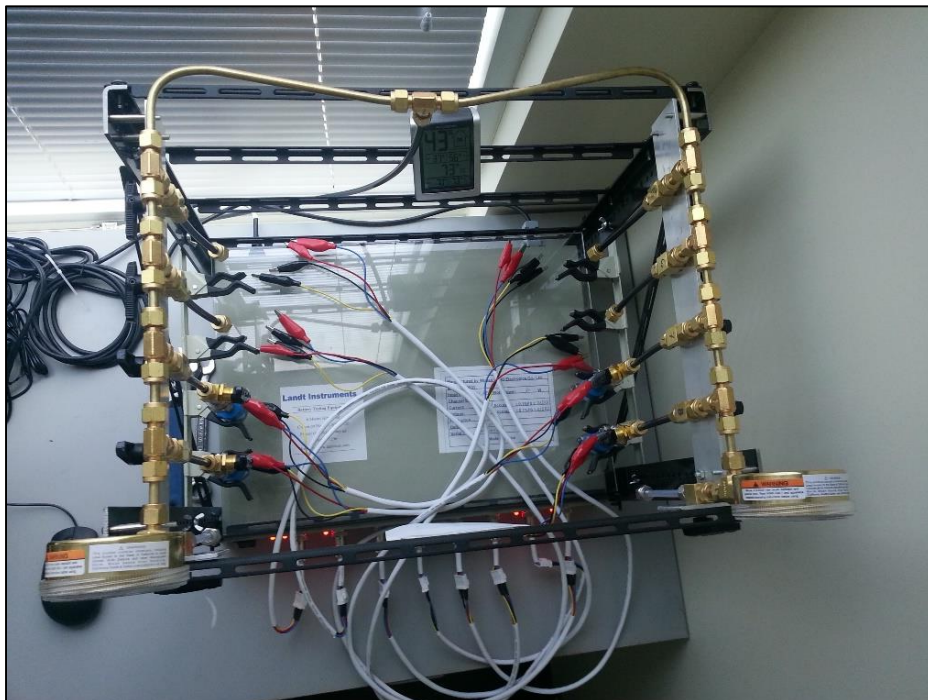
Figure 16: Top view of the oxygen supply system.

III. Experimental Work

This chapter discusses the experimental procedures used to conduct the proposed work in Chapter I. The sample preparation section covers the steps taken to prepare the electrolyte, the carbon cathode, the assembling process and the procedure to introduce oxygen to the samples. This section also comprises the material and the suppliers that were used for the study. The second section of this chapter details the testing technique procedures applied to characterize the samples. Galvanostatic cycling was used to assess the performance of the batteries; titration was used to determine the lithium peroxide yield; and electrochemical impedance spectroscopy helped assess the impedance evolution.

A. Sample Preparation

The key components in a lithium cells are the lithium metal anode, the electrolyte (salts in a solvent) and the air cathode (carbon/binder mix on a substrate). This section discusses the procedure used to prepare each of these components with chemicals commercially available.

i. Electrolyte preparation

Tetraethylene glycol dimethyl ether (Tetraglyme/TEGDME/4G, 99.91 %, BASF Corporation) essay had a water content of 88 ppm and was dried with molecular sieves (4 Å) for a week in the glovebox. Dimethoxyethane (monoglyme/DME/1G, anhydrous, 99.5 %, Sigma Aldrich) was used as received. Dimethyl carbonate (DMC, 99.5 %, Sigma Aldrich) was dried with molecular sieves (4 Å) for a week in the glovebox. Lithium trifluoromethanesulfonate (LiTf, 99.995%, Sigma Aldrich) was dried in a vacuum oven at 80 °C for 48 hours before bringing it inside the glovebox. Bis(trifluoromethane) sulfonamide lithium salt (LiTFSI, 99.95 %, Sigma Aldrich) was used as received since it was packaged in an inert environment. Each of these chemicals have been stored in the glovebox permanently with moisture concentration below 10 ppm. The electrolyte solution was prepared by actively mixing salts into the specific solvent and was left overnight to insure complete dissolution.

ii.   Air Electrode Preparation

Five variations in the air cathode were tested in this study. The carbons were combined with a binder solution to bind them onto a carbon paper substrate. The solvent used to mix the binder and carbon is then evaporated before using the cathode.

Ketjen Back, KB (EC-600JD, Akzo Nobel Polymer Chemicals) carbon was crushed with a pestle and mortar for 20 minutes to obtain a fine power. Acetylene Black, AB (AB 50%-01, Soltex Synthetic Oils & Lubricants of Texas, Inc.) carbon, Vulcan Black, XC72 (CV-XC72R, Clean Fuel Cells Energy, LLC) carbon, multi-walled carbon nanotubes, CNT (MCNT 8-15 nm, Cheap Tubes Inc.) and graphene nanoplatelets, Graph. (Grade 4 GNPs, Cheap Tubes Inc.) were used as received. The properties of each carbon as reported by the manufacturer can be found in Table 1.

Table 1: Properties of the carbon materials studied

Carbon	Morphology	Surface Area (m^2/g)	Pore Volume (cm^3/g)
Graphene Nanoplatelets (Graph.)	Planar	750	0
Multi-walled Carbon Nanotubes (CNT)	Tubular	233	0
Vulcan XC 72 (XC72)	Spongious	235*	0.32*
Ketjen Black (KB)	Spongious	1,400	7.6
Acetylene Black (AB)	Spongious	75	0.23[#]

* Properties not available from the manufacturer [42]
[#] Property not available from the manufacturer [44, 45]

A binder solution (3 wt%) was prepared by dissolving polyvinylidene fluoride, PVDF binder (Kyna 900, Arkema Inc.) and 1-methyl-2-pyrrolidinone, NMP solvent (Anhydrous, 99.5 %, Sigma Aldrich) with the homogenizer at elevated temperature (~80 °C) until it fully dissolved. The solution was cooled down to room temperature before use. To mix the slurry, each carbon was added to the binder solution with a 4:1 carbon to binder weight

ratio and additional NMP solvent included in the solution to acquire proper wetness. The slurries were spread with a SS spatula on carbon paper (Toray TGP-H-030, Fuel Cells Etc) and dried at room temperature for at least 48 hours in a covered petri dish to slow the evaporation. This process showed improved concentration of cracks found on the electrodes. The same slurry was used at multiple occasions sometimes over a few weeks after it was made and it was found that the drier the slurry was, the fewer cracks were found at higher loading. Due to the accuracy of the analytical balance, the loading of the electrodes were on average 2 mg/cm^2. The electrodes were punched with a ½" O'Brien Arch Punch (PerfectFit) outside the glovebox and dried for at least 36 hours in a vacuum oven at 70 ˚C. The oven was then purged with HP argon gas and the electrodes were placed in the transfer chamber of the glovebox where a deep dynamic vacuum was maintained for at least an hour before use. The electrodes were stored in the glovebox in separate vials. Table 2 recapitulates the proportion used for each carbon:

Table 2: Optimized mixing ratios for each carbon electrode slurries. Final carbon/binder weight ratio was 4:1.

Carbon	Binder Solution	Carbon	Additional NMP
Graphene Nanoplatelets	0.667 g	0.080 g	0.0 g
Multi-walled Carbon Nanotubes	0.667 g	0.080 g	0.650 g
Vulcan XC 72	0.667 g	0.080 g	0.800 g
Ketjen Black	0.667 g	0.080 g	1.765 g
Acetylene Black	0.667 g	0.080 g	0.500 g

iii.   Cell Assembly

A slightly adapted Swagelok design was used to house each cell [45]. A stainless steel tubing (1/2" dia, Swagelok) and rod (89535K15, McMaster-Carr) was inserted on either side of a perfluoroalkoxy, PFA, ½" union (PFA-820-6, Swagelok) to provide oxygen

access and closure for the cell, respectively. A SS conical compression spring (1692K22, McMaster-Carr) provided pressure on the cells and electrical connection to the SS rod. A ½" SS disk (2895T51, McMaster-Carr) placed between the spring and the cell provided a distributed even pressure across the battery. The original PFA ferrule sets in lieu of SS were used for the assembly since a good seal was obtained and it still permitted to be adjusted (for appropriate spring compression). A recapitulating figure can be found below (Figure 17).
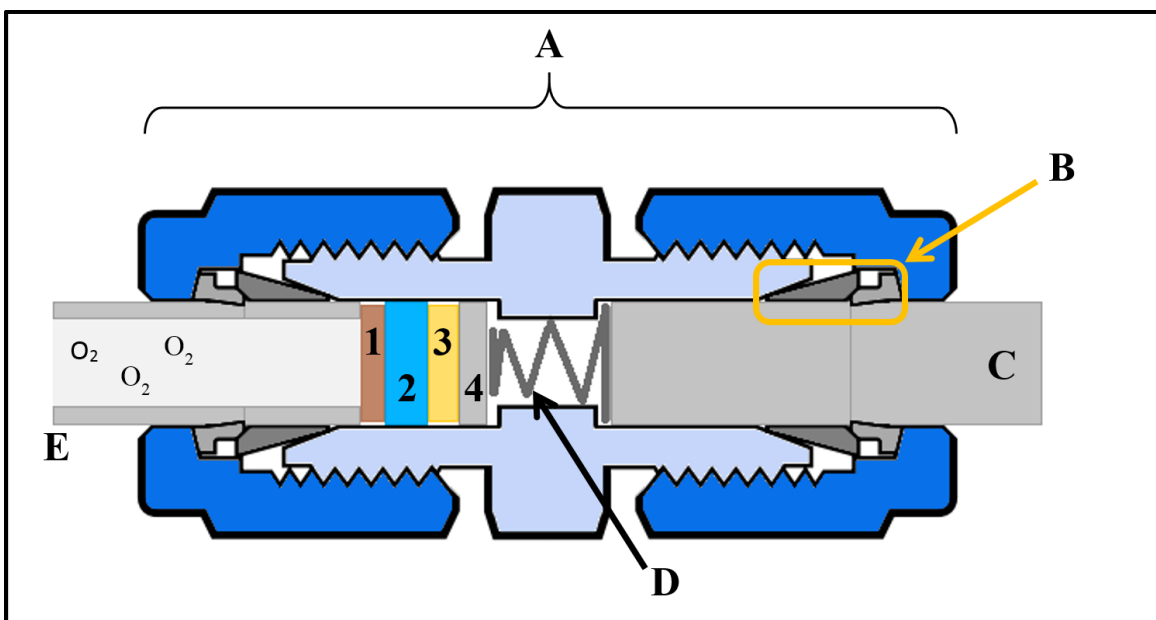
Figure 17: Cross-section assembly of a Swagelok cell design. (1- Air cathode, 2- Spacer/electrolyte, 3- Lithium Anode, 4- Stainless Steel Spacer, A- Swagelok PFA Union, B- PFA ferrule set, C- Stainless Steel rod, D- Stainless Steel Spring, E- Stainless Steel Tubing).

Concerning the electrochemical cell, the anode was a lithium metal foil (0.6 mm thick, GoodFellow) punched with a 3/8" arch punch inside the glovebox and used within 2 weeks of being punched. A ½" glass fiber paper (GF/B, Whatman) was used as separator soaked in electrolyte. A ½" polypropylene (PP) membrane (2500, Celgard) was used to prevent adhesion from the cathode on the glass fiber paper. Lastly, the carbon electrode was placed on top of the PP membrane with the carbon paper current collector facing the stainless steel tube. The cell was closed with the other side of the union with a close in-lined valve to isolate the electrochemical cell from the environment. The compression of the spring was

34

kept as consistent as possible by compression the SS rod as far as possible onto the internal lip of the union. The back of the ferrule set on the SS tube was placed at 0.6 inches from the end of the tube.

Once the samples were assembled, they were rested for 2 hours to allow the electrolyte to impregnate everywhere inside the cell wetting all the surfaces of the various carbons. The cells were then taken out of the glovebox for testing. The small volume of argon gas trapped between the electrodes and the valve (2.08 cm^3) was removed by applying the cell to a shallow vacuum (-25 inHg absolute pressure) and quickly replaced with UHP oxygen gas. At the operating pressure of 4 psig, the total number of moles of oxygen stored in that volume was 109 μmol though the valve was never shut off during testing. To attach the alligator clips of the battery tester onto each cell, two hose clamps were tightly secured on the SS rod and SS tube (see Figure 18). Lastly, a PFA flexible tubing was used to connect each individual cell to the oxygen supply system while still electrically insulating them from one another (Figure 18). The samples were connected vertically with the air cathode facing upward to reduce the loss of electrolyte and to insure its even distribution. Each cell was numbered and associated to a specific channel on the battery tester to avoid over-tightening their compression fitting, as recommended by Swagelok – Figure 18 shows channel 1 and 2. When connecting a new cell to the oxygen system, the oxygen system valve (top of Figure 18) was cracked-open to purge air out of the PFA tubing. The connecting nut was then tightening slowly reducing the leak. Once completely air tight, the valve on the Swagelok cell (bottom of Figure 18) was opened exposing the battery to the UHP oxygen gas. When the testing was concluded, the samples were disassembled inside to glovebox. For safety reasons, each electrode was placed in their respective waste containers.
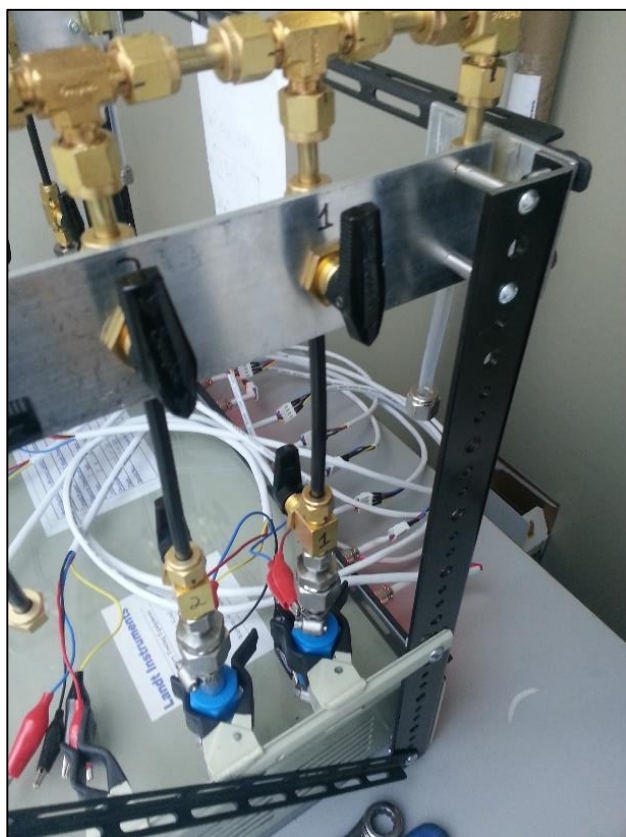
Figure 18: Fully Assembled Swagelok Cell connected to the oxygen supply system.

B. Testing Technique Procedures

Three testing techniques were used in this study: galvanostatic cyclic testing, iodometric titration and EIS. In this section, each technique procedures is detailed including the testing conditions and the equipment used to conduct the test. The results of these three testing techniques are categorized in the Results chapter.

i. Galvanostatic Cyclic Test

The foremost testing technique characterizing the effect of various carbon morphologies in a lithium-oxygen cell is a galvanostatic cyclic test. This repeatable test assesses the overall performance of cell at a specific cycling rate. A constant current (CC) per unit area (mA/cm^2) testing condition is used for the discharge and charge cycle as it allows comparative analysis of voltage behavior. The galvanostatic cyclic testing outputs a capacity-dependent voltage profile that highlights the different reaction potentials.

In the instance of a Li-O$_2$ chemistry, a distinct plateaus (leveled potential as the cell is discharged) in early cycles have been associated to specific chemical reactions. As discussed in Chapter 1, cells exposed to a CC condition demonstrate a discrete plateau around 2.7 V, which is associated with the formation of lithium peroxide either via disproportion or reduction of lithium superoxide species [16]. Figure 19 shows a common discharge profile with the associate reactions.
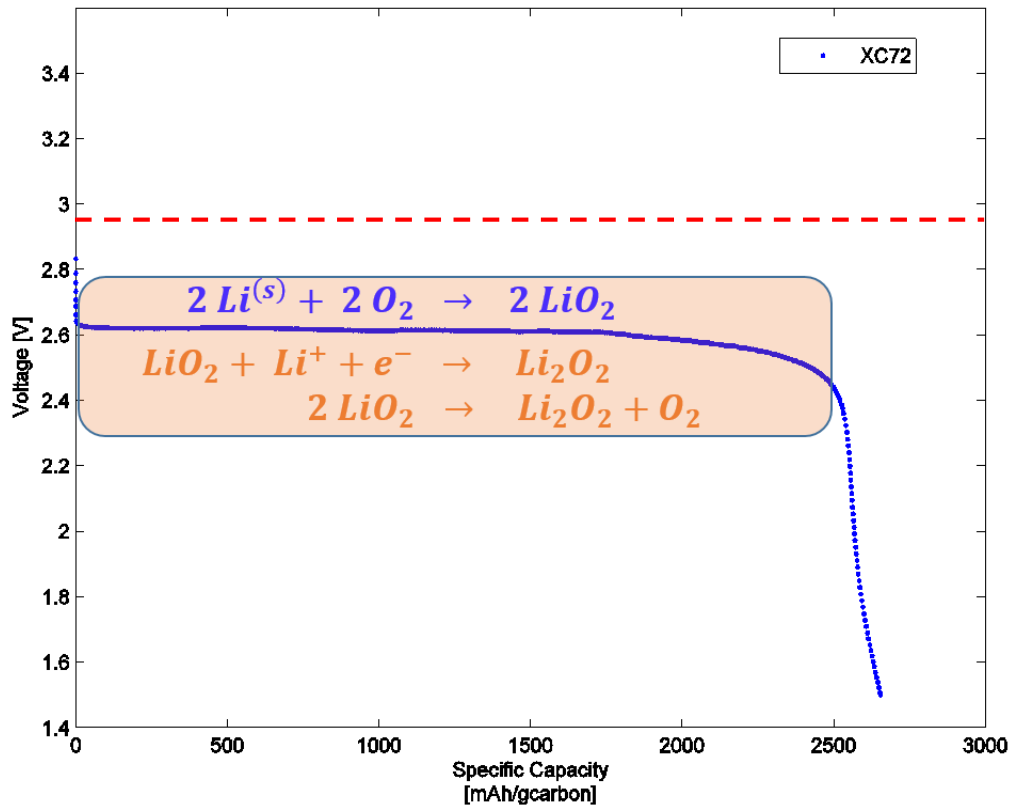
Figure 19: Voltage profile of a cell discharged down to 1.5 V showing the reaction potentials. The dashed red line shows the standard redox potential (U$_o$) of lithium peroxide formation (2.96 V).

The charge profile of lithium-oxygen cells is slightly more challenging to analyze and relate to specific reaction mechanisms. The oxygen evolution reaction (OER) theoretically disassociates lithium peroxide to form oxygen gas and lithium ions. However, side reactions can occur due to the corrosive nature of the oxidation of lithium peroxide [46]. This highly reactive form of oxygen has also more drastic effects with high surface area

carbon cathodes [46]. Figure 20 demonstrates the charging profile of Li-O_2 cell during their first cycle.
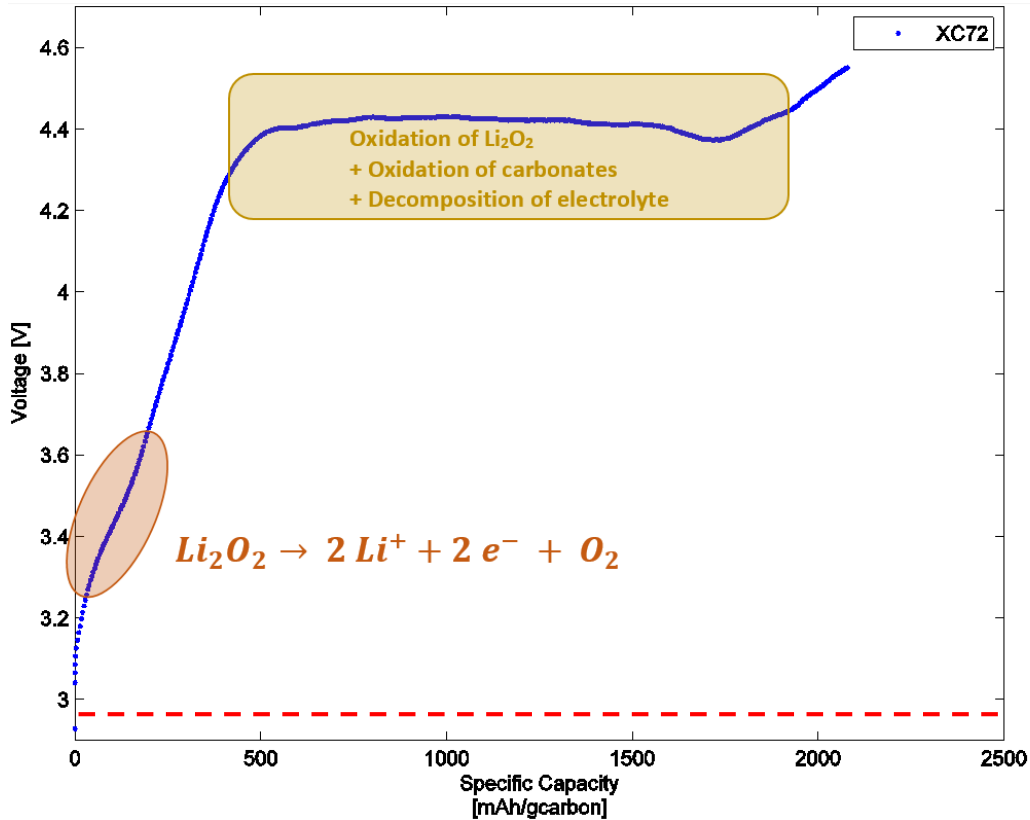
Figure 20: Voltage profile of a charge cycle showing the reaction potentials. The dashed red line shows the standard redox potential (U_o) of Li_2O_2.

The initial resistance corresponding to the low discharge plateau (compared to U_o) is due to diffusion rates of oxygen and lithium ions at a specific current density [18], [47]. The late increasing resistance is associated to the build-up of lithium peroxide reducing the charge transport to the electrode surface. On the charge step, the general resistance shown from the different of the charging plateau with the standard redox potential is also associated with the diffusion rates and the formations of insulating Li_2O_2 and side products.

Each cell were cycled with a Landt Instrument battery tester (CT2001A – 5 mA – 5V) at room temperature. The constant current rate used in the entirety of this work was 0.1 mA/cm^2 to reduce the limiting effect of oxygen diffusion, viscosity or conductivity of the

38

electrolyte. This value was iterated from findings published in 2006 on the rate capabilities concluding that rates under 0.2 mA/cm^2 had no correlation with those factors [18]. The cut-off voltage for the discharge cycle was set at 2.0 V to remain consistent with the literature [5, 10, 49]. The charging cycle was set at the same rate as discharge and the cut-off voltage was set at 4.55V to avoid compromising the charging capacity obtained with the voltage window of the electrolyte.

ii. Iodometric Titration

The benefit of electrochemical energy storage is the practical efficiency of a specific reversible chemical reaction. As previously discussed, the sought-after product of a lithium-oxygen cell reaction is lithium peroxide (Li_2O_2). However, side reactions have been observed to occur simultaneously and generate irreversible and also insulating byproducts – carbonate and hydroxide species [33].

Until recently, the evolution of lithium peroxide was only qualitatively analyzed with various techniques such as scanning electron microscopy (SEM), nuclear magnetic resonance (NMR), Fourier transform infrared spectroscopy (FTIR), X-ray photoelectron spectroscopy (XPS), Raman spectroscopy or X-ray diffraction (XRD) [29, 50]. Although providing information about the overall system, those techniques can only establish whether lithium peroxide is present comparatively to other discharge product. In August 2013, McCloskey et al. published about the first time a well-known analytical chemistry technique – hydrogen peroxide titration – was applied to a lithium-oxygen system [39]. Adapted to accurately and repeatedly quantify the formation of lithium peroxide in a cycled cell, this technique can be used to gain insights on the overall chemical process and determine the Li_2O_2 yield at various cycle.

By exposing a discharged air electrode to de-ionized water, lithium peroxide will react to produce hydrogen peroxide guided by the following reaction (Equ. (10)). McCloskey et al. also discussed the effect of the side reaction shown in Equation (11) and the oxygen

evolution was concluded to be negligent making the ratio of lithium peroxide to hydrogen peroxide one-to-one.

$$Li_2O_2 + 2H_2O \rightarrow 2LiOH + H_2O_2 \qquad (10)$$

$$Li_2O_2 + H_2O \rightarrow 2LiOH + \frac{1}{2}O_2 \qquad (11)$$
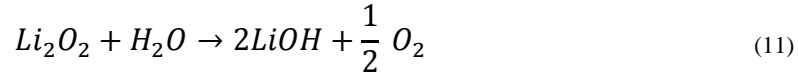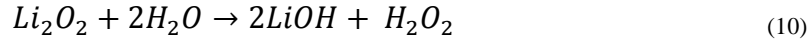
Thus, the formed hydrogen peroxide can be titrated very accurately using one of the various titration techniques. Although permanganate titration yields a higher accuracy, iodometric titration is less prone to react with organic solvents – which are used as an electrolyte (glymes, DMSO, ...) in a large number of Li-O$_2$ studies – making this technique more appropriate for quantifying lithium peroxide [39].

In presence of an acid and a molybdate catalytic solution, hydrogen peroxide reacts with iodide to form iodine which can afterward be titrated with a thiosulfate solution, as shown in Equ.(12) & (13).

$$H_2O_2 + 2KI + H_2SO_4 \rightarrow I_2 + K_2SO_4 + 2H_2O \qquad (12)$$

$$I_2 + 2Na_2S_2O_3 \rightarrow Na_2S_4O_6 + 2NaI \qquad (13)$$
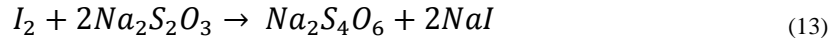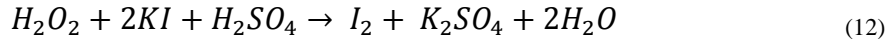
With the help of a starch indicator, the titration of iodine undergoes a drastic color change once the iodine has been reacted completely. Thus, the amount of the thiosulfate solution introduced in the solution is directly related to the quantity of iodine present which is therefore related to the quantity of lithium peroxide originally introduced in the vial.

In the proposed lithium peroxide titration technique, a number of controls were used to identify the accuracy and repeatability of the technique. The following is a summary of what was discussed in details by McCloskey et al. [39]:

1. The composition of the cathode may have an effect on the titration accuracy.
2. LiTFSI salts crystalizing on the electrodes did not have a catalytic effect in the titration yielding in accurate measurement of un-dried electrodes.

3. The solvent due to un-dried electrode did not have an effect on the titration accuracy if performed in a short period of time (>3 min.)
4. Side products such as lithium carbonate and lithium carboxylates did not affect the accuracy.
5. Constant yield of peroxide if the cell is discharged for more than 0.1mAh.

The theoretical quantity of lithium peroxide from in a discharge cycle can be found using Gibbs free energy equation, seen Equation (14).

$$\Delta G = -n\, F\, E \tag{14}$$

Where ΔG is Gibbs Free Energy or the energy from the reaction, n is the number of mole electron participating in the reaction, F is Faraday's constant and E is the potential at which the reaction occurred. This equation can thus be rearranged to assess the theoretical number of moles of lithium peroxide a cell should have produced given the capacity. Thus, the energy produced by a cell when discharged for 1 mAh is:

$$Energy = Capacity \cdot Potential = (-0.001Ah)(E) \quad [\text{V Ah}] \tag{15}$$

Using this value in Gibbs Free Energy equation, the total number of electron moles can be found as follow:

$$(-0.001Ah)(E) = -n\left(96{,}485\ ^{C}/_{mol\ e-}\right)(E) \tag{16}$$

$$n = -\frac{(-0.001Ah)}{\left(96{,}485\ ^{C}/_{mol\ e-}\right)} * \frac{3{,}600\ C}{1\ Ah} = 37.311 \quad [\mu mol\ e^{-}] \tag{17}$$

Given a 2 e$^-$/mole Li_2O_2 process, the quantity of lithium peroxide present in an ideal lithium-oxygen cell after a discharge capacity of 1 mAh is 18.667 μmol. This value will later be used to determine the yield of lithium peroxide of various cells.

iii.   Electrochemical Impedance Spectroscopy

The two techniques previously discussed in this section only assessed the performance of the cell as a whole. EIS measurements can provide insights on the evolution of various impedances within the cell at different points of the cycle. When assembled, each element of a cell reacts with one another and form surface layers that affect the overall charge transport. In contact with the electrolyte, the lithium will form a thin passive solid electrolyte interface (SEI) layer that protects the lithium from degradation. Understanding the charge transport mechanisms of various interfaces and their evolution during cycling can provide great information if combined with the two previously discussed techniques. For instance, the rapidly degrading discharge capacity can be studied with respect to developing internal interfaces.

EIS is a highly versatile analytical technique that has been applied to various types of system studies such as corrosion rates, interface reactions, mass transport and other reaction parameters. Described by Ohm's law (Z=E/I, where Z is impedance, E is potential and I is current), a system is exposed to a series of sinusoidal signals (voltage or current) over a specific range of frequencies and the response (current or voltage, respectively) is used to calculate the impedance of the system at that frequency. Combining both a real (resistance) and imaginary (capacitive and inductive) value, the impedances collected through this process can be plotted in a Nyquist plot and analyzed to find an equivalent circuit model. Based on the model, the kinetic parameters of various interfaces can be monitored as they vary within the system. This in-situ technique – tested in its environment – is especially powerful when associated with other techniques. Thus, the purpose of this analysis in this work is to monitor the evolution of interfaces as a cell is cycled and correlate any observations to the Li_2O_2 yield and capacity value from the cell.

Two types of EIS testing techniques can be used: galvanostatic and potentiostatic EIS. The GEIS test will expose the sample to a sinusoidal voltage at a certain magnitude around a constant value and the response current is measured to acquire the impedance data point.

42

On the other hand, a PEIS test will input a sinusoidal current of a certain magnitude around a specific value – either zero or at constant current – while recording the response voltage.

In the battery field, EIS has been utilized on a laboratory level to study the internal impedances evolution and correlate them to the deterioration of capacity [50]. More specifically, impedance spectroscopy has been used in prototype cell to assess the health of the battery at various cycles [51]. In the case of lithium-oxygen cells, EIS has been explored to assess the development of impeding layers within the cells [48, 51, 53–55]. As expected, the SEI layer forming on the lithium and the ionic transport to the cathode has the most obvious effect [51, 53]. The three major impedances found in the discussed lithium-oxygen cell are the electrolyte resistance, the SEI resistance and the mass transport resistance [52]. These impedances will increase throughout cycling [51, 54] and associating it with internal reactions can help understand the properties of the side products formed. Evolution of those impedances can also be correlated with the yield of lithium peroxide.

A SP200 Bio-Logic potentiostat was used to conduct all the EIS measurements in this study. The frequency range that were tested in each sample was 1 MHz to 0.1 Hz, unless otherwise stated. The voltage was kept constant at the sample's OCV and the magnitude of the sinusoidal voltage signal was 5 mV. Each sample was tested before and after the galvanostatic testing to provide an assessment of the development of the internal impedance of the cell. Lastly, the impedances of the electrical connection were characterized to confirm their negligibility in the overall cell impedance. Each connection within the design of the cell was modelled as shown in Figure 21 while the equivalent circuit of the electrochemical system can be found later in this report.
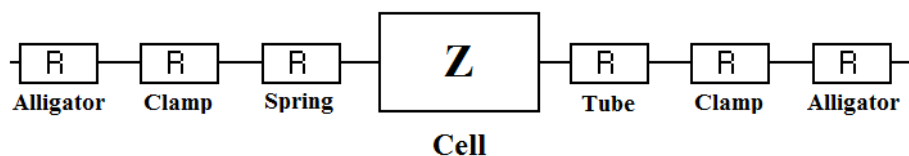
Figure 21: Equivalent circuit of all connections in an assembled Swagelok cell

43

Thus, a number of controls were performed to assess the contact resistance between each cell:

1. The first control that was run on the cell assembly was the impedance due to the alligator clips from the instrument and the stainless steel hose clamps on each electrode contact. To characterize this value, two hose clamps were attached on a single SS rod. The impedance found from all those connections was found to be between 0.03 Ω and 0.06 Ω. The variation was due to the alligator clip connection and is considered as negligible compared to other values.

2. The second control was used to characterize the impedance due to the spring connection. A stainless steel rod was used for each electrode in a Swagelok cell. A wide window of value was found varying from 0.354 Ω to 3.5 Ω. The lower value was found in a cell that was compressed to its maximum and the lower value was found in a cell with little pressure. The resistance found in the spring compressed that would simulate the compression of a full cell was found to be on average 0.5 Ω.

3. The last control characterizes the resistance between the tube and the cell. Since limited surface area is connected to the rest of the cell, the resistance is significantly higher. The impedance found between a stainless steel disk and the SS tube was on average 6.25 Ω. Since those two pieces have very high tensile strength which may not simulate the porous carbon cathode, a carbon paper layer was added to the control and the resistance was found to increase slightly (7.5 Ω). This may be due to the additional resistance between the SS disk and the carbon paper.

With a better understanding of the base-line impedances present in the cell, a model the lithium oxygen cell to further understand the reaction mechanisms and layer formation evolution. The results of this technique can be found in the following section and its analysis in the discussion section.

IV. Results

Beyond this, the objective of this section is to demonstrate the experimental results obtained from the evaluation of Li-O$_2$ batteries in the experimental setup described in Chapter III31. The results are categorized by each test: galvanostatic cycling, titration and impedance spectroscopy.

A. Galvanostatic cycling results

As previously explained in Chapter III, this test was conducted to assess the effects of various carbon materials in lithium oxygen batteries. Again, five carbon materials were tested to determine their effective capacity and their voltage profile. No additional mediators or catalyzers were used in the cells in order to be able to assess and compare the performance of the carbon materials alone. At least three specimens were tested for each sample to determine repeatability in the testing. The galvanostatic testing was pursued for the first, second and third cycles to assess the performance of the carbon cathode and to determine if repeatable cycling can be performed. The relevance of this test increases once compared to the other two tests conducted in this work.

i. First discharge cycle test

The first discharge cycle assesses the effect of the carbon material used in the cathode both on the discharge capacity and the potential at which the cell is discharged. Each of the cathodes was constructed similarly with a loading around 1.0-2.0 mg/cm^2 and a slurry composition of 4:1 carbon to binder. Table 3 recapitulates the statistical average of the first discharge specific capacities obtained for each carbon cathodes. Agreeing with the literature [34], KB cathodes have the highest specific capacity followed by Vulcan XC72, carbon nanotubes and acetylene black. Graphene nanoplatelets showed un-expected performance as the surface area of the carbon is relatively high.

Table 3: Average first discharge capacity for the different carbon cathodes

Carbon Cathode	First Discharge Capacity
Graphene Nanoplatelets	250
Multi-Walled Carbon Nanotubes	2,885
Vulcan XC72	2,439
Ketjen Black	6,795
Acetylene Black	2,659

The other insight that can be taken from this data is the activation potential at which the main reaction occurs. From Figure 22, each carbon has a very different discharge voltage plateau. CNTs show a relatively high reaction potential followed by KB, XC72 and AB. This variation in the voltage profile is related to the activation energy required for the reaction to occur [46], [55]. Thus, from this data, multi-walled carbon nanotubes cathode has the lower activation potential.

Figure 22: First discharge voltage profile of various carbon cathode. Graphene Nanoplatelets (Blue). Multi-walled carbon nanotubes (Green). Vulcan XC72 (Red). Ketjen Black (Fuchsia). Acetylene Black (Purple).

When the axes are adjusted, it becomes clearer that the discharge plateau for graphene shows a slopped potential, as shown in Figure 23. A possible approach for this observation

can be related to the increased polarization from high current density per electrode surface area related to low pore volume/high surface area material.
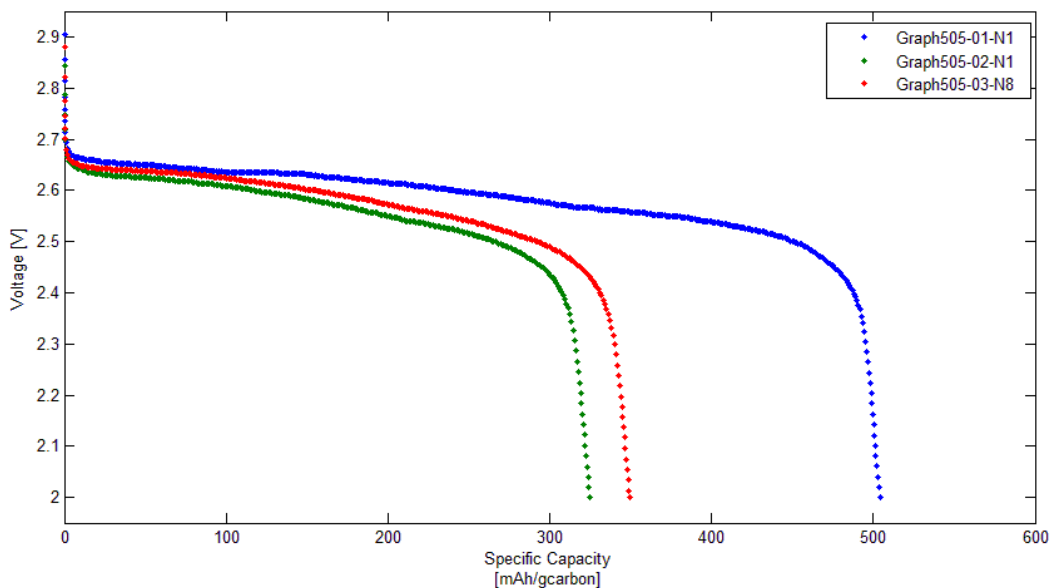
Figure 23: Graphene nanoplatelets discharge profile of multiple specimens demonstrating the constant decrease of voltage over the first discharge cycle.

ii.   Third discharge cycle test

The properties of carbon materials affecting the initial discharge capacity of the cell can be very insightful for designing primary batteries. However, the rechargeability of this battery chemistry is what will make this technology practical. Thus, additional cells were exposed to three discharge-charge cycles and stopped at a discharge state for titration. This limited cycle test allowed to evaluate the rechargeability of the various carbon cathodes and to determine how well the reaction could be reversed. The data produced from this test show the different charging voltage profiles as well as how it progresses within cycling. Figure 24 illustrates the statistical average of the specific capacity for the first three discharges for each carbon cathode. At least three specimens with repeatable data were taken for each cathode. Additional specimens were taken during this test though variability in the testing procedure excluded them from these results. An example of the reason for variability would be the drastic loss of oxygen supply to a number of specimens included erratic results. Thus, those samples were excluded from the results.
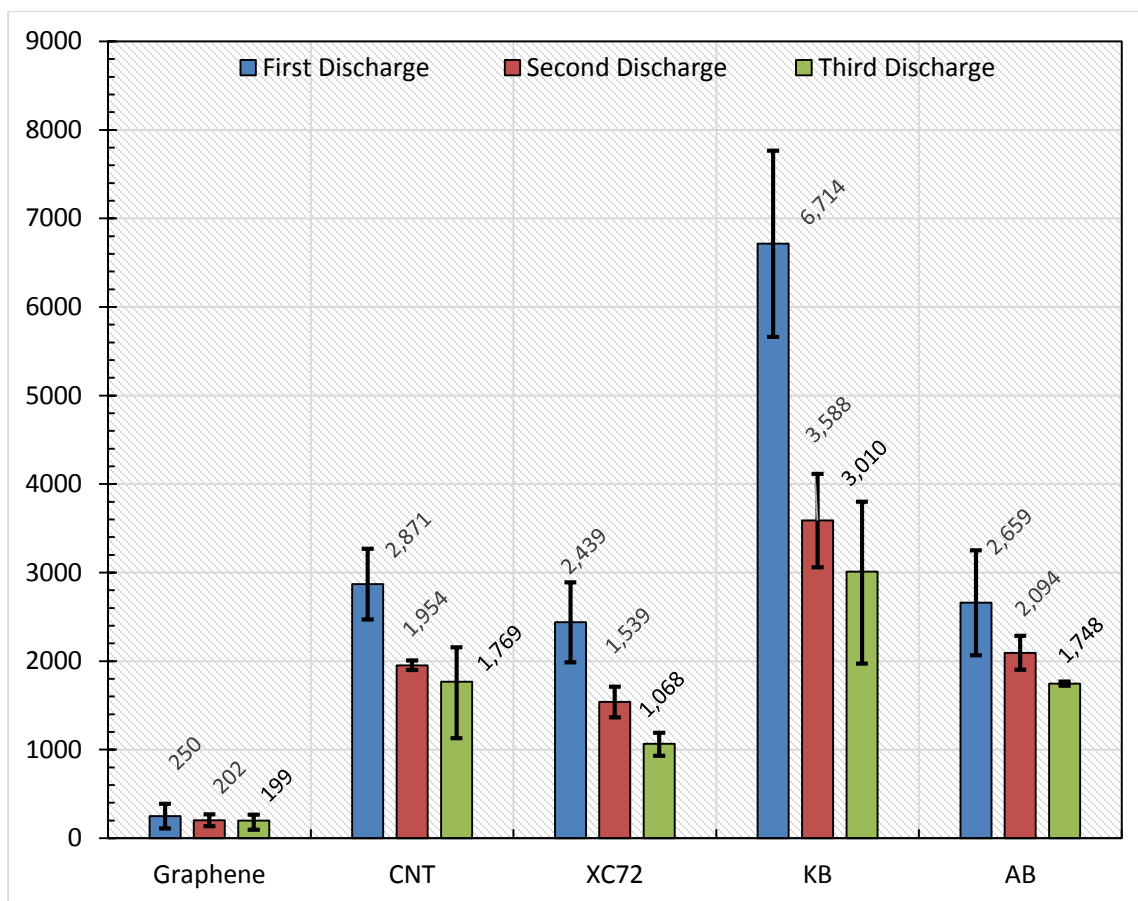
Figure 24: Discharge capacity of various carbon cathode for the first three cycles. BLUE: first discharge specific capacity. RED: second discharge capacity. GREEN: third discharge capacity. Values are represented in mAh/g_{carbon}. The error bar illustrates the standard deviation.

Acetylene black and Vulcan XC72 demonstrated a relatively consistent loss of capacity between the first, second and third cycle. In comparison, carbon nanotubes and graphene nanoplatelets demonstrated a more stable capacity retention after the initial discharge. Lastly, Ketjen black carbon had the largest capacity drop from its initial discharge approaching 50 % of the first discharge. Although a significant number of cells were tested to acquire these results, it is important to understand that this data only provide a glimpse on the cyclability of the carbon material.

The voltage profiles of the charge step are very different from carbon to carbon (Figure 25). Cathodes with Ketjen Black carbon demonstrate the lowest charging potential out of all the carbon on the first cycle charge. Multi-walled carbon nanotubes shows also a lower

charging voltage while Vulcan XC72 and acetylene black have similar charging profile with higher voltage. As expected, graphene nanoplatelets have the highest charging potential around 4.5 V.
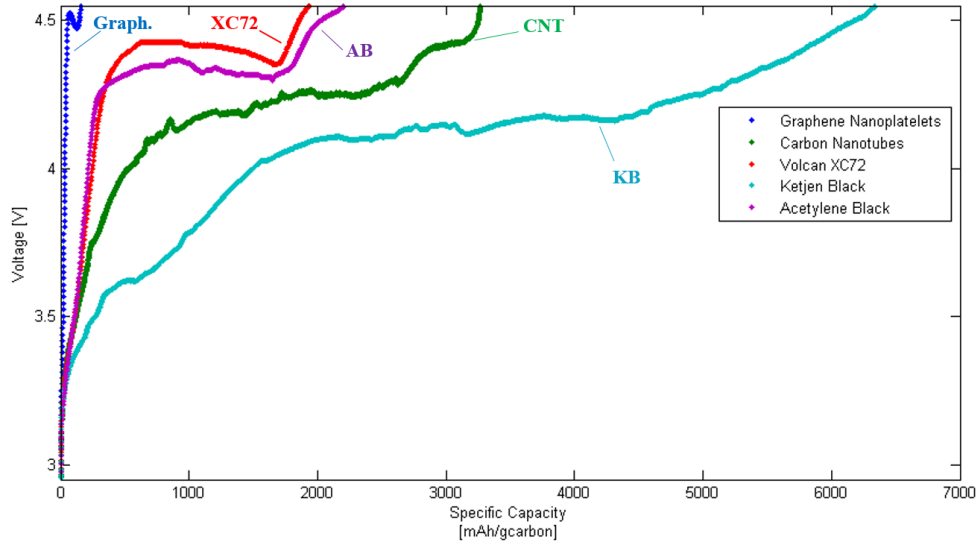
Figure 25: Voltage profile of the first charge cycle of various carbon cathode. Graphene Nanoplatelets (Blue). Multi-walled carbon nanotubes (Green). Vulcan XC72 (Red). Ketjen Black (Fuchsia). Acetylene Black (Purple).

The second charge cycle shows already a change in the internal reaction with the very different voltage profiles. Figure 26 groups the second charge cycle for the various carbon cathodes. The order of potential values over the whole discharge is still similar to the first cycle charge. However, the shape of the voltage profiles seem to be shifting between a distinct potential plateaus around 4.0 – 4.4 V for the first cycle and 4.3 – 4.5 V for the second cycle. This difference is clearly displayed on the profiles of CNT cathodes: the two distinct plateaus in the second cycle can also be found on the first cycle although the first one is more predominant in the first cycle. As it will be later discussed in more details, this shift in potential is mainly associated with side products layering the cathode and thus increasing oxidation voltage of lithium peroxide.

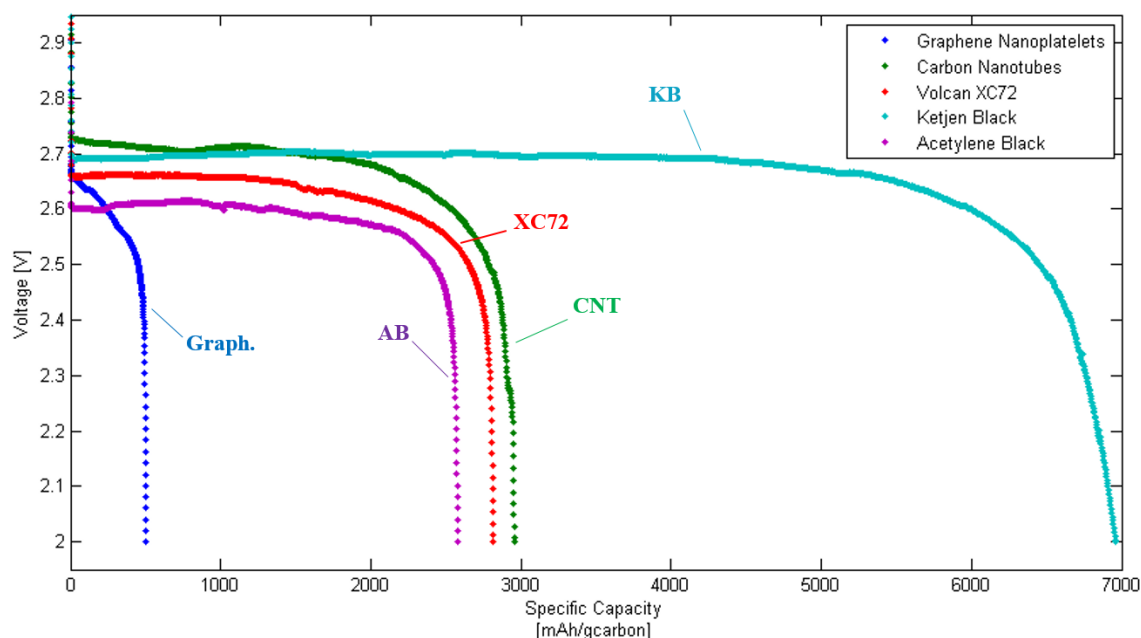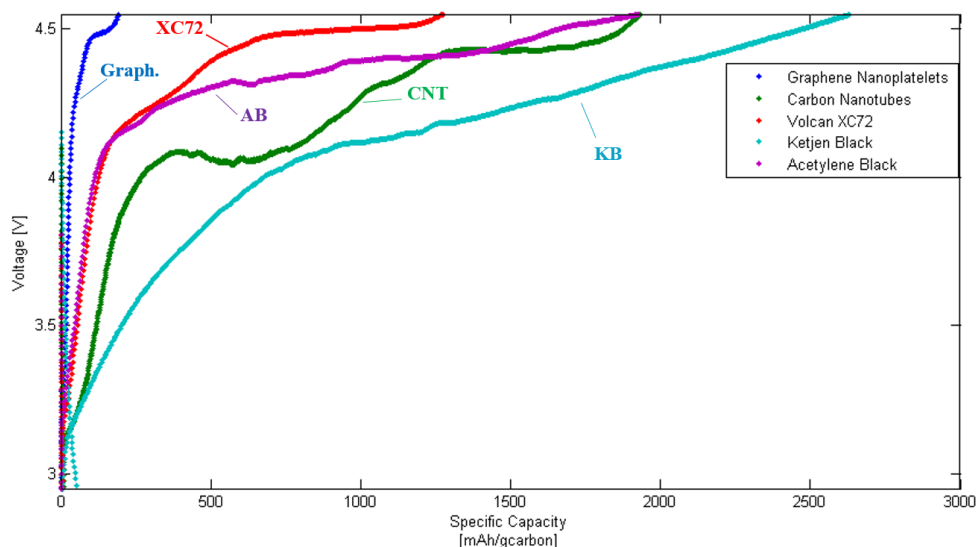Figure 26: Voltage profile of the second charge cycle of various carbon cathode. Graphene Nanoplatelets (Blue). Multi-walled carbon nanotubes (Green). Vulcan XC72 (Red). Ketjen Black (Fuchsia). Acetylene Black (Purple).

Similarly, when the discharge profiles are compared to one-another, the evolution of the voltage profile can help to understand the mechanism of the reactions (Figure 27). The first observation to draw is the evolution of the KB plateau. As shown in the inset figure, the potential of the KB cell at the early discharge stage is slightly higher in the third cycle and the discharge plateau is not as flat as in the first two cycles. This evolution suggests that the reaction occurring is more complex than the simple lithium peroxide formation. Layers of side products may be deposited on the carbon electrode requiring the reaction to behave slightly differently on KB cathodes. This could also be associated with the clogging of the pores as previously suggested. Although this would require confirmation with scanning electron microscopy, the main result from the evolution of the discharge profiles is the change from a flat plateau to a slopped one. This indirectly confirms the presence of side reactions and side products occurring in the cell after the initial cycle.

50
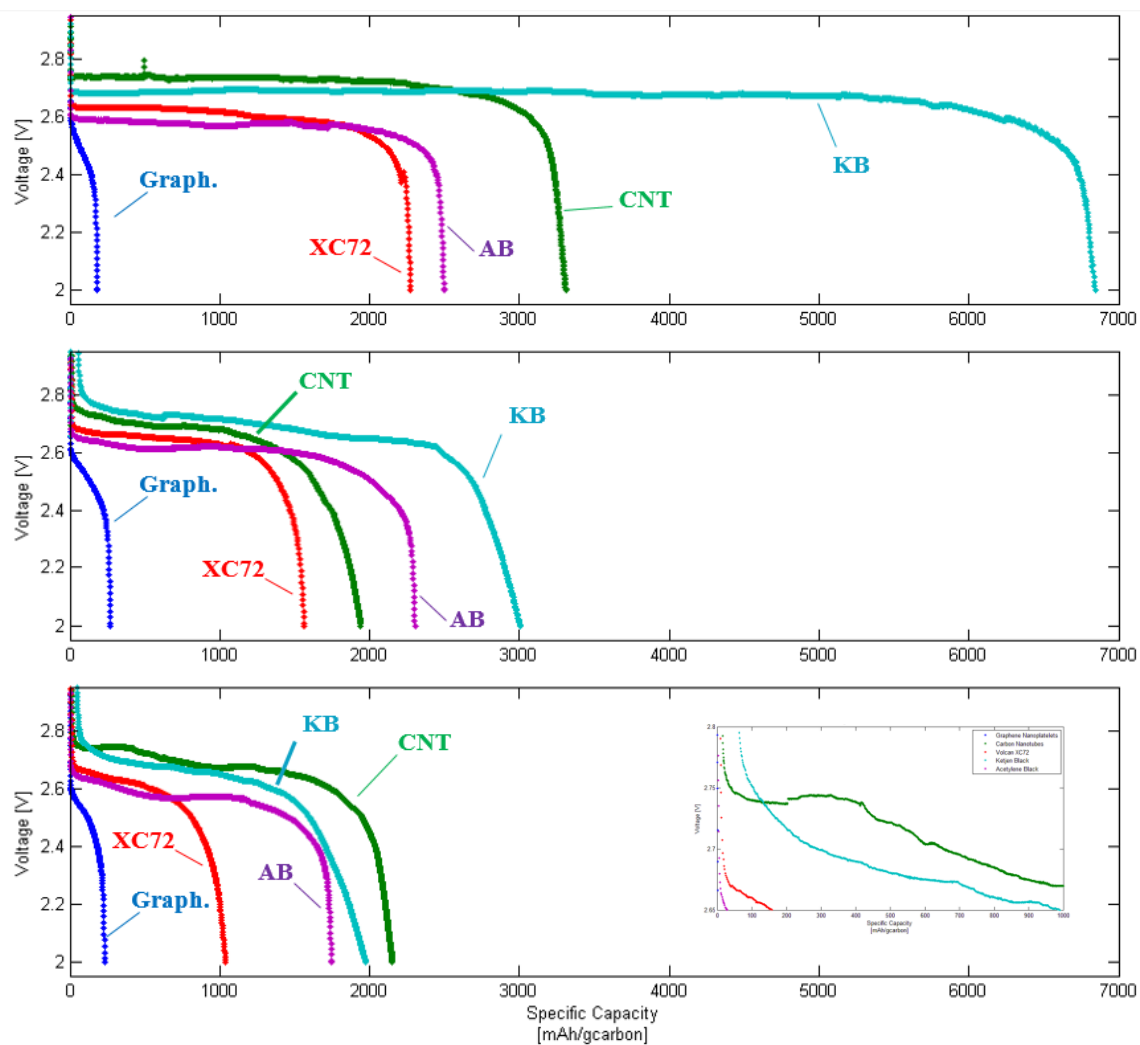
Figure 27: Discharge profiles for the first (TOP), second (MIDDLE) and third (BOTTOM) cycle of various carbon cathodes. Graphene Nanoplatelets (Blue). Multi-walled carbon nanotubes (Green). Vulcan XC72 (Red). Ketjen Black (Fuchsia). Acetylene Black (Purple). INSET: zoom on the activation potential for KB and CNT for the third cycle.

iii.   First discharge with different electrolyte composition

Since the data presented above show that the voltage profile is dependent on the carbon material, the effect from the electrolyte was also sought after. The hypothesis behind this test was that the electrolyte composition would also vary the voltage profile of the first discharge. Figure 28 shows the discharge voltage profiles of four cells with electrolyte variation: solvent, salt and salt concentration.

51

From Figure 28, the total capacity delivered from the cells are again grouped in two distinct trends. The 1.0 M LiTf samples have a specific capacity two fold higher than with the LiTFSI salt or higher LiTf concentration. As each sample were assembled identically side by side, tested at the same time and with electrodes from the same batch, the only variable resulting in this trend is the electrolyte composition. One would think that increasing the concentration of the salt would improve the reaction mechanisms in the cell but the presented data show contrary. Additional testing is suggested to further characterize the effect of the concentration of salts on the capacity of the cell.
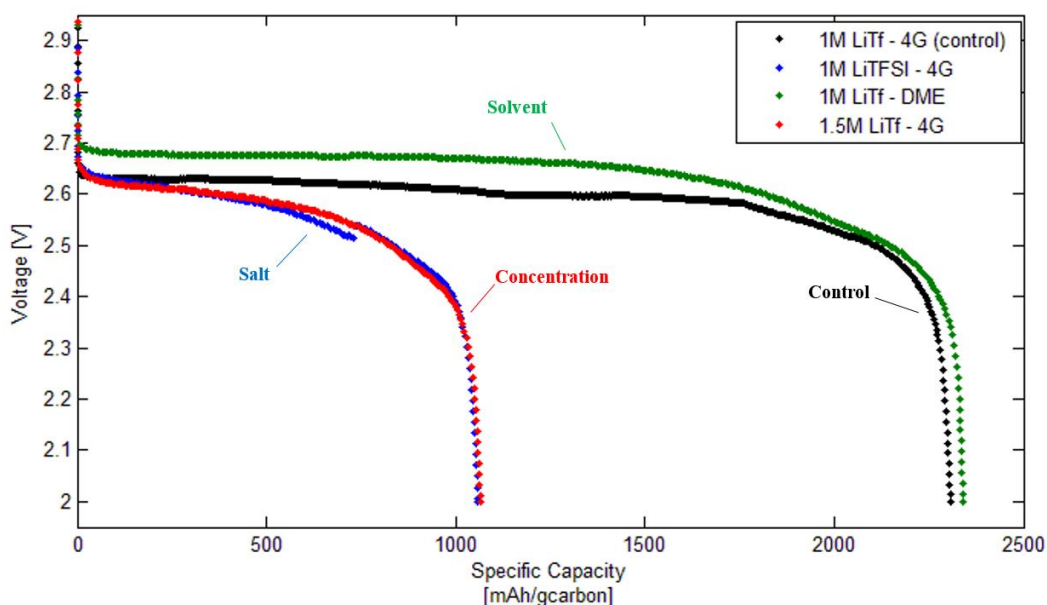
Figure 28: Voltage profile of the first discharge cycle for XC72 cathodes with different electrolyte compositions

iv.   First discharge at a higher current density

For all the samples tested in this study, a discharge rate of 0.1 mA/cm^2 was set based on the limited oxygen diffusion and ionic conductivity, as discussed in Chapter III. By maintaining the current density constant, other parameters of the battery were extracted to better understand their contribution to the overall process. However, a sample was tested to demonstrate that the current density has an effect on the performance of the battery. A cell was assembled with a XC72 carbon cathode and 1 M LiTf/4G electrolyte following

the same procedures as discussed in the previous chapter to set the current density as the only variant. A rate of 0.25 mA/cm^2 was arbitrarily chosen to estimate the effect of the discharge rate without being limited by the oxygen diffusion [18]. Figure 29 shows the galvanostatic voltage profile of the sample in comparison to a control with identical conditions.
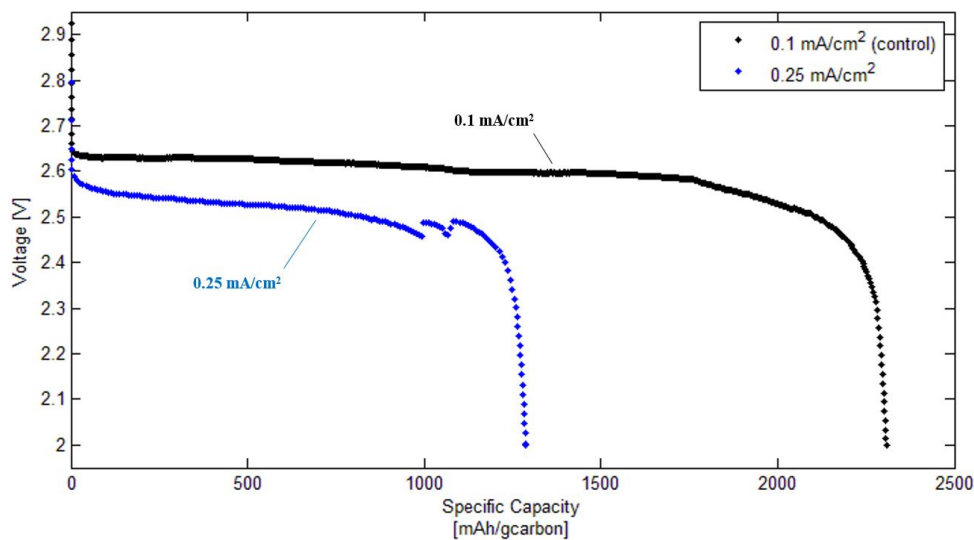
Figure 29: Voltage profile of XC72 cathode at various discharge rates

As expected, the potential decreased and the capacity also decreased at the higher discharge rate. The two abrupt changes in voltage at 0.25 mA/cm^2 sample are due to the changes in oxygen pressure when additional cell were connected to the oxygen supply system and are not intrinsic to the actual discharge process. The change of pressure was less than 1 psi at one time. Further testing conditions, such as operating O_2 pressure, voltage cutoffs or current density, may provide more insights on the battery performance and its dependence on the diffusion of Li+ ions and O_2.

B. Iodometric titration results

The previous section discusses the total capacity drawn from each cells with the various carbon cathodes. Furthermore, it discusses the chemistry of discharge and charge processes and investigates reversibility. However, the performance of the battery is only assessed on its overall characteristics, such as current, voltage and capacity, and not on the contribution from the desired reversible reaction (i.e. formation of lithium peroxide). As lithium oxygen batteries is supposed to feature a reaction between lithium and oxygen in a controlled and reversible manner, a relatively stable and reversible product of that reaction is lithium peroxide. However, the nature of the chemistry also produces side reactions that can be insulating and irreversible. Therefore, quantifying the yield of Li_2O_2 after discharging a cell can provide a true assessment on the performance of the battery. Furthermore, as part of the scope of this thesis work, the performance of the various carbon cathodes are tested to determine the lithium peroxide yield at different cycles, cell compositions and testing conditions.

i.   First and third discharge peroxide yield

Quantifying the lithium peroxide yield has only been recently applied to the field of research of lithium-air batteries [39]. As a result, carbon materials used in cathodes for lithium oxygen batteries have not yet been quantitatively studied for their lithium peroxide yield as they are discharged. This section studies the lithium peroxide yield as a function of the properties of the carbon material in the cathode after the first and the third discharge cycles. With respect to the study conducted by McCloskey et al. [39], the expected outcome is that a slight variation of peroxide yield will be observed at the first discharge and this difference will be more defined at the third discharge. To provide an accurate estimation on this testing, three specimens were tested for each carbon after the first and third discharge. The outcome of test is presented in Figure 30. A few limitations to the data presented must be discussed before analyzing the trends. The length of time between the end of the discharge and the titration varied due to the limited laboratory access (nights and

Sundays). The titration equipment was limited to 0.1 mL accuracy translating on average to 0.8 % lithium peroxide yield.
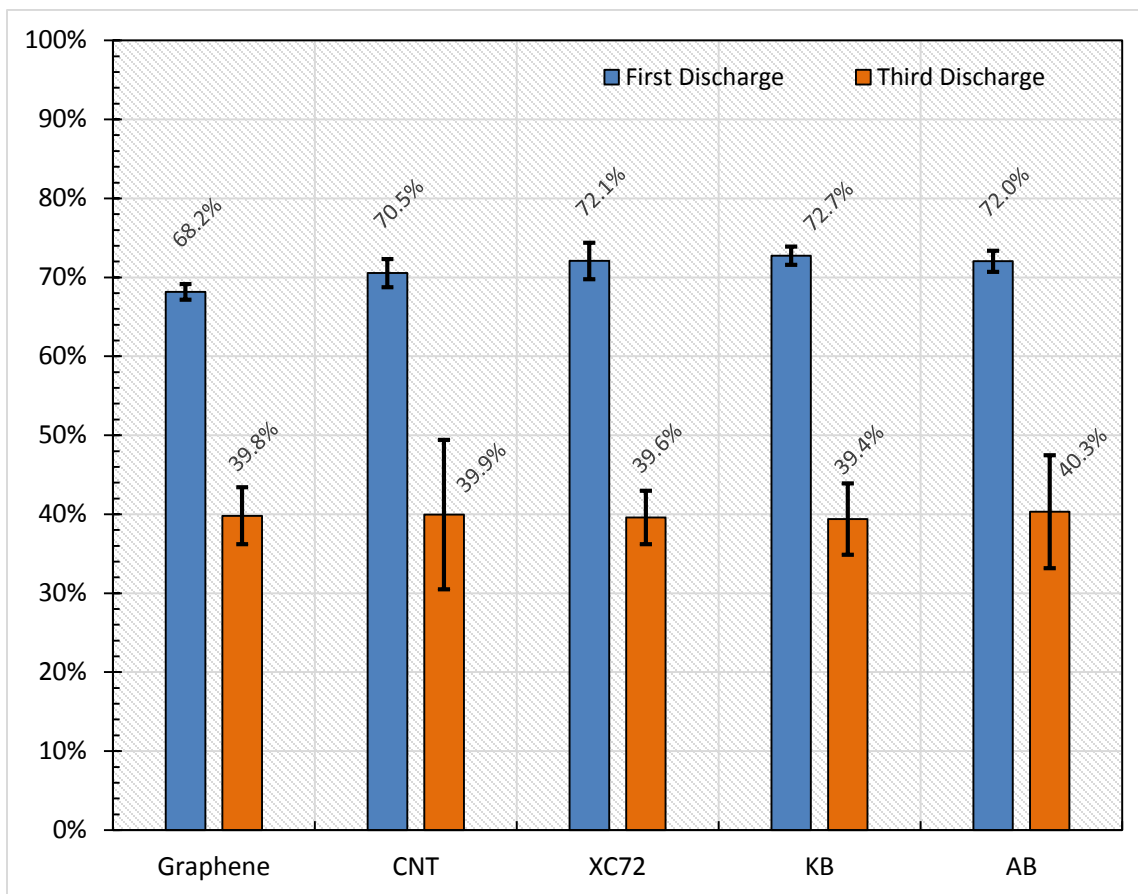
Figure 30: Lithium peroxide yield for the various carbon cathode at the first and third discharge cycle. The error bar illustrates the standard deviation.

Although some limitations on the accuracy of the data are presented, a significant trend is observed in the lithium peroxide titration results. A slight variation on the yield of peroxide between each carbon type is observed for the first and third cycles and the third cycle yield drops as expected. This important observation is further discussed in Chapter V. As the results slightly deviates from specimen to specimen, several tests are conducted to obtain statistical averages. Furthermore, this variation in the titration of lithium peroxide is accentuated on the third cycle (larger standard deviation of the data). This is mainly related to the length of the galvanostatic test of some samples that are individually well over 300

testing hours. Thus, the trends in the data in lieu of the very specific statistical average value is highlighted in this work.

    ii.   Peroxide yield of different cell composition

In the publication by McCloskey et al. introducing the titration of lithium peroxide, a range of peroxide yield is presented with different cell composition [39]. The study varies a few carbon materials, and electrolyte compositions demonstrating that each element effects the yield of peroxide. Since the previous section shows little effect from the carbon material on the lithium peroxide yield, different electrolyte composition is investigated here to determine how it effects the discharge process. Therefore, three variants are tested to demonstrate that the electrolyte has a larger effect on the peroxide yield [39]: the solvent, the salt and the salt concentration. Monoglyme (DME) is tested as an alternate solvent for its viscosity lower than tetraglyme. LiTFSI salt provides an alternative to lithium triflate salt and higher concentration of salt provides possible contribution from salt decomposition. The data acquired from this test can be found in Table 4. The results from this test revealed that the alternative solvent has similar yield of Li_2O_2. The current density was kept maintained at 0.1 mA/cm^2 to avoid effect from the ionic transport. This hypothesis is further tested with the increased salt concentration and the alternative salt.

Table 4: Effect of the electrolyte composition on the lithium peroxide yield of cells with Vulcan XC72 cathodes

Electrolyte Composition	Li_2O_2 Yield
1.0 M LiTf – 4G	70.2 %
1.0 M LiTf – DME	68.0 %
1.0 M LiTFSI – 4G	43.5 %
1.5 M LiTf – 4G	48.9 %

The outcome of the test presented different results. The use of a DME showed statistically identical peroxide yield with 4G while both the alternate salt and salt concentration showed lower yield. This is suspected to be related to the significant contribution from instability

of Li salts to the decreased yield of the lithium peroxide. This theory could be further tested using elemental analysis of the side products.

iii.   Peroxide yield with different testing conditions

Lastly, the lithium peroxide yield is measured in identical batteries with different testing conditions. This test is primarily used to assess the impedance evolution after a fast discharge though the lithium peroxide yield is recorded to provide some insights on the battery performance. The samples are titrated to determine how a higher current density would affect the yield of peroxide. Furthermore, two other testing conditions are used to further understand the overall chemistry: a discharged specimen to 1.5 V and a charged specimen to 4.55 V. The former may assess the reduction of lithium peroxide to lithium oxide at lower potentials and the later helps determine whether lithium peroxide can still be found at high voltages. Their peroxide yield can be found in Table 5.

Table 5: Effect of the current density on the lithium peroxide yield of cells. Controls are underlined.

Carbon	Current Density	Voltage Cutoff	Li_2O_2 Yield
XC72	0.1 mA/cm^2	2.0 V	70.2 %
XC72	0.25 mA/cm^2	2.0 V	78.1 %
XC72	0.1 mA/cm^2	1.5 V	70.0 %
KB	0.1 mA/cm^2	2.0 V	67.2 %
KB	0.1 mA/cm^2	4.55 V	51.9 %[*]

* Titration was conducted after the charge cycle and theoretical value was obtained from the difference between the discharge and charge capacity.

Given the complexity of the system, expectations from this test were unsupported but the outcomes demonstrated interesting results. The first observation is that higher lithium peroxide yield is found when discharged at a higher rate. This suggests that side reactions are suppressed at high rate compared to lithium peroxide formation. The second observation from this series of tests is the statistically identical lithium peroxide yield at 1.5 V cut-off voltage discharge. This suggests that the reduction of lithium peroxide to

lithium oxide does not occur with this carbon/electrolyte combination. The last test of this section was pursued to determine whether lithium peroxide was present when a cell was not fully charged to its previous discharge capacity. This test has significance for the third cycle discharge lithium peroxide yield test. In contrary to the literature [39], the presence of lithium peroxide at the charge state of the battery confirmed that some lithium peroxide was already present in the cell at the start of the second discharge cycle. This is an important observation suggesting that the lithium peroxide found at the third discharge may not have been cycled three times.

C. Electrochemical Impedance Spectroscopy results

When defining the scope of this work, electrochemical impedance spectroscopy was a technique that was suggested to further understand the reaction mechanism inside a cell and to correlate internal impedance evolution with the formation of lithium peroxide and side products in Li-O_2 batteries. Therefore, this chapter discusses the EIS data acquired on each specimen both in their pristine and terminated state.

i.   First and third discharge impedance

The first set of samples tested in the previous two techniques was the effect of carbon material in the cathode for the first discharge cycle. To further understand the system, an EIS measurement with a frequency range of 1 MHz – 0.1 Hz was also taken on each of the samples. Figure 31 and Figure 32 illustrates the internal impedance of cells before and after the discharge cycle respectively. The objective of this test is to illustrate the evolution of the impedance as discharge products are accumulated on the cathode. The anticipated outcome of this test would be a noticeable impedance shift that could be associated with the discharge products and more specifically with the lithium peroxide formation. The results demonstrated a more complex system that would require further testing to fully understand the test outcomes. In this section, general observations on the change in impedance are drawn but deeper understanding of the EIS cell spectrum, such as an equivalent circuit, can be found in Chapter V.

Figure 31: Initial impedance of various carbon cathode in a full cell. Graphene nanoplatelets (Blue). Multi-walled carbon nanotubes (Red). Vulcan XC72 (Green). Ketjen Black (Purple). Acetylene Black (Pink).
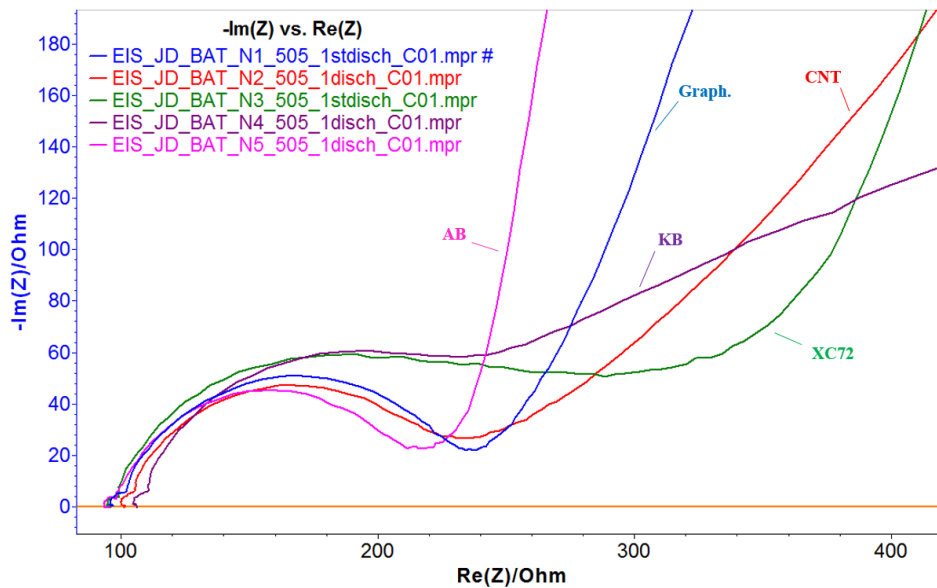
Figure 32: Impedance of various carbon after a full galvanostatic discharge. Graphene nanoplatelets (Blue). Multi-walled carbon nanotubes (Red). Vulcan XC72 (Green). Ketjen Black (Purple). Acetylene Black (Pink).

When comparing one-by-one the impedance of the pristine and discharged cells, a few observations can be drawn. The foremost is the general initial real impedance being very consistent around 100 Ω even after discharge. This suggests that the initial real impedance

59

is solely associated with the cell structure and not with the layers formed on the different surfaces. The second observation is the carbon-dependent ionic diffusion rate at low frequencies – more specifically the diffusion slopes. Last, the morphology of the carbon material appears to have an effect on the impedance of discharge products at low frequencies since a significant variation in the diffusion rates were obtained in discharged cells. Once the cells were charged again, this variation disappeared and the ionic diffusion rates of the different carbon electrodes became analogous again.

Similarly, the impedance after the third discharge was also recorded to assess how limited cycling would affect the impedance inside the cell. Figure 33 and Figure 34 show the impedance of batteries with the various carbons at their pristine state and at the end of their galvanostatic cycle test, respectively. The first point to draw is a comparison between the two sets of samples at their pristine state (Figure 31 and Figure 33). The initial real impedance is found to be very similar around 100 Ω while the impedance at the beginning of the diffusion part (around 300 Ω) seems to be larger than the first set of samples (around 240 Ω). This discrepancy is suggested to be related to the cell's exposition to oxygen, time-wise and pressure-wise. This is further explained in Chapter V.
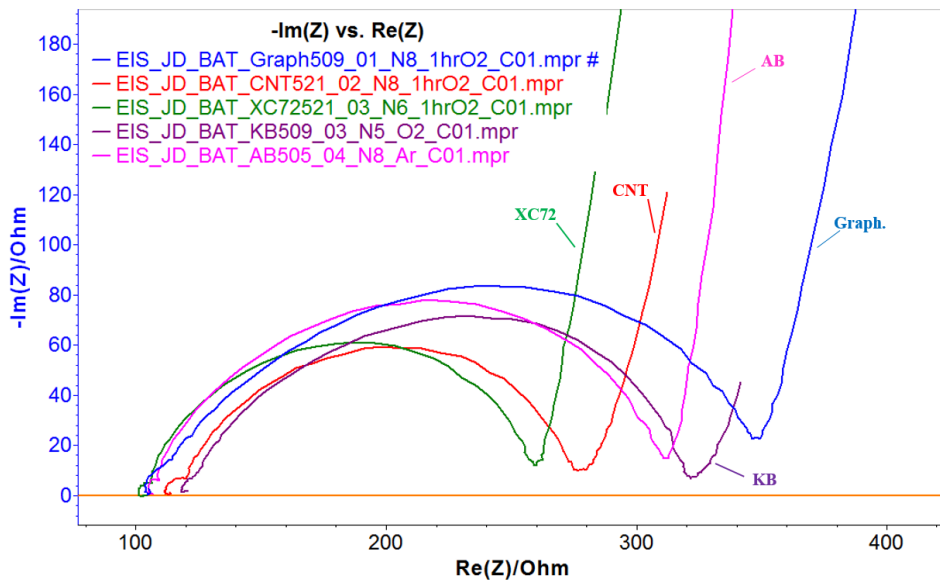
Figure 33: Initial impedance of various carbon cathode tested for three cycles. Graphene nanoplatelets (Blue). Multi-walled carbon nanotubes (Red). Vulcan XC72 (Green). Ketjen Black (Purple). Acetylene Black (Pink).

The second observation is the complex impedance after three discharges shown in Figure 34. As one may notice, the distinct half circle start to flatten with certain carbon cathodes. This is believed to be associated with the formation of side-reaction products on the carbon material. A comparison with the galvanostatic cycling and titration data did not reveal significant trends to generate a clear conclusive observation on the data. Many factors, such as cycling efficiency, quantity of discharge products, lithium peroxide yield, electrolyte decomposition, carbon loading or carbon morphology may affect the impedance spectrum of a cell. Although some of these factors are later studied in this section, additional testing isolating each parameter systematically is suggested to obtain a realistic understanding of the data.
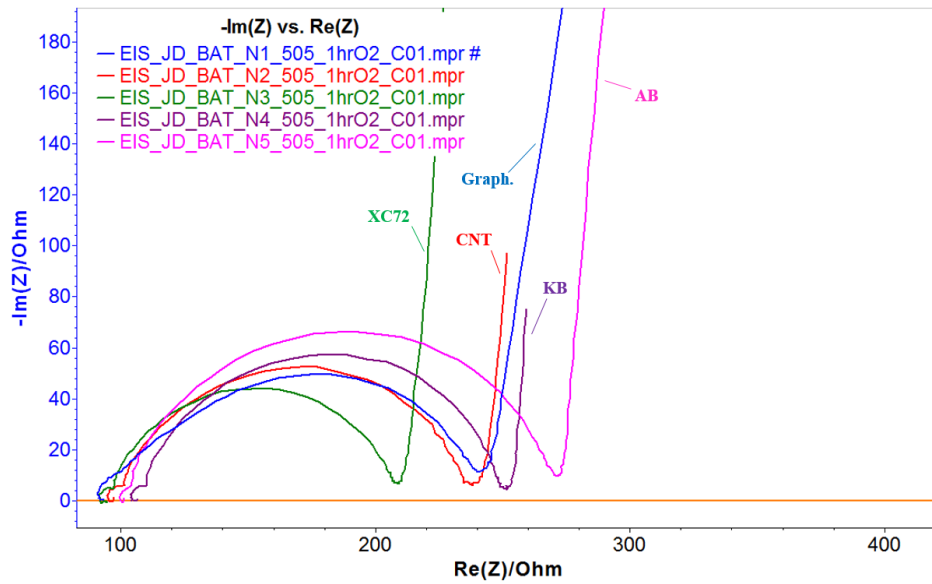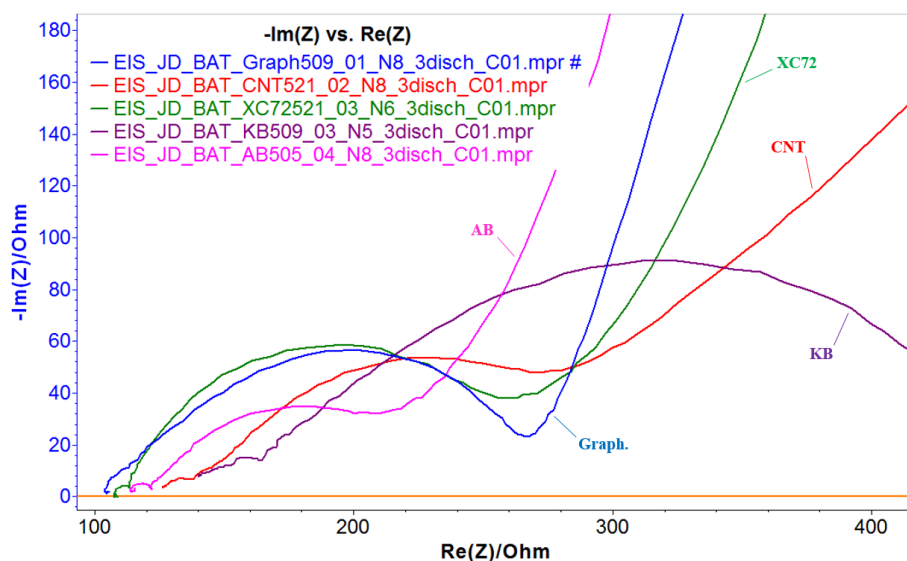

Figure 34: Impedance of various carbon cathode tested after three cycles. Graphene nanoplatelets (Blue). Multi-walled carbon nanotubes (Red). Vulcan XC72 (Green). Ketjen Black (Purple). Acetylene Black (Pink).

ii.   Electrolyte impedance

The impedance collected from various cells appeared to be relatively similar across carbon electrodes. However, the initial impedance around 100 Ω seems remarkably high to only be associated with the connection impedance of the Swagelok cell (refer to section iii in Chapter III). Thus, a number of variations on the electrolyte composition are tested to better understand the effect of each one. The liquid electrolyte used in this work is varied by

changing the solvent, the salt and the concentration of the salt. This test is only conducted to confirm that the electrolyte has an important effect on the overall cell impedance.

To eliminate variables, the same cell was reused for each test reducing the variation in the connection impedance. Each specimen was constructed similarly to what was discussed in an earlier chapter: a SS disk was used to support the lithium chip, a glass fiber with a Celgard was used as a separator soaked with 160 μL of electrolyte (1 M LiTf in tetraglyme). Finally, an activated carbon paper (Freubenger C2, Fuel Cells Etc) was used to eliminate any cathode preparation factors. Impedance spectroscopy measurements were taken after exactly two hours of rest in argon (for wetting purposes), after 30 minutes of exposure to UHP oxygen at 10 psi and after one hour of UHP O_2 exposure. The Nyquist plots for those cells are shown in Figure 35.

The first approach is to determine how the solvent effect the ionic conductivity of the cell. Thus, a less viscous solvent – dimethyl ether (monoglyme, DME, 1G) – replaces the solvent used in this study (tetraglyme, TEGDME, 4G). The salt and its concentration is kept constant with 1M lithium triflate. The results shows drastic improvement on the impedance of the cell as expected. The improvement is associated to the low viscosity of the solvent promoting the ionic conductivity.

Following this approach is studying the effect of the salt on the total impedance of the cell. Thus, one molar of LiTFSI replaced the LiTf in 4G. Again, the impedance of the cell drastically drops improving the ionic transport in the cell.

Lastly, the last variation that could be made with the electrolyte is the concentration of the salt. The objective behind this test was to demonstrate the effects from the salt concentration in the impedance response of the cell. As shown on the Nyquist plot, the high frequency resistance of a sample with 1.5 M LiTf in tetraglyme shows negligible improvement though the capacitive imaginary impedance (top of the half circle) is considerably lowered. Further investigations on the effects of the electrolyte is suggested to optimize its composition.

62
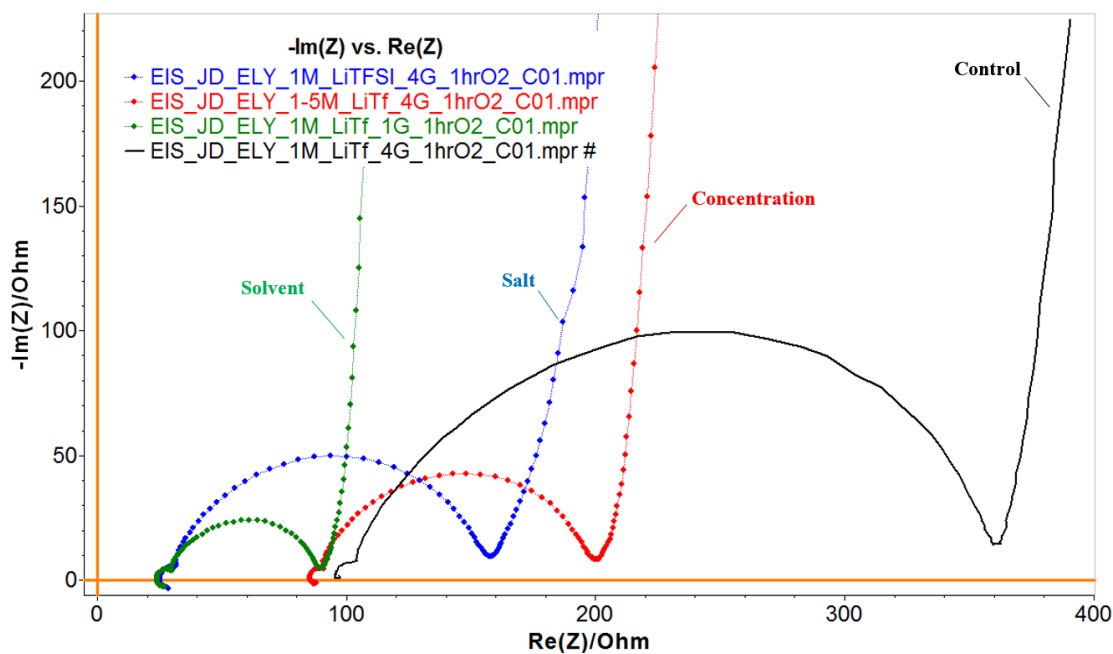
Figure 35: Effect of the electrolyte on the overall impedance of the cell. The cathode used in these samples was a commercially available carbon paper.

The test conducted above shows only the impedance spectrum of pristine cells. However, it is also important to investigate the effects of the electrolyte on the impedance of a discharge cell. XC72 cathodes were used for these samples due to their highly repeatable titration data. Figure 36 illustrates the impedance spectrum of XC72 cathode cells with different electrolyte composition.
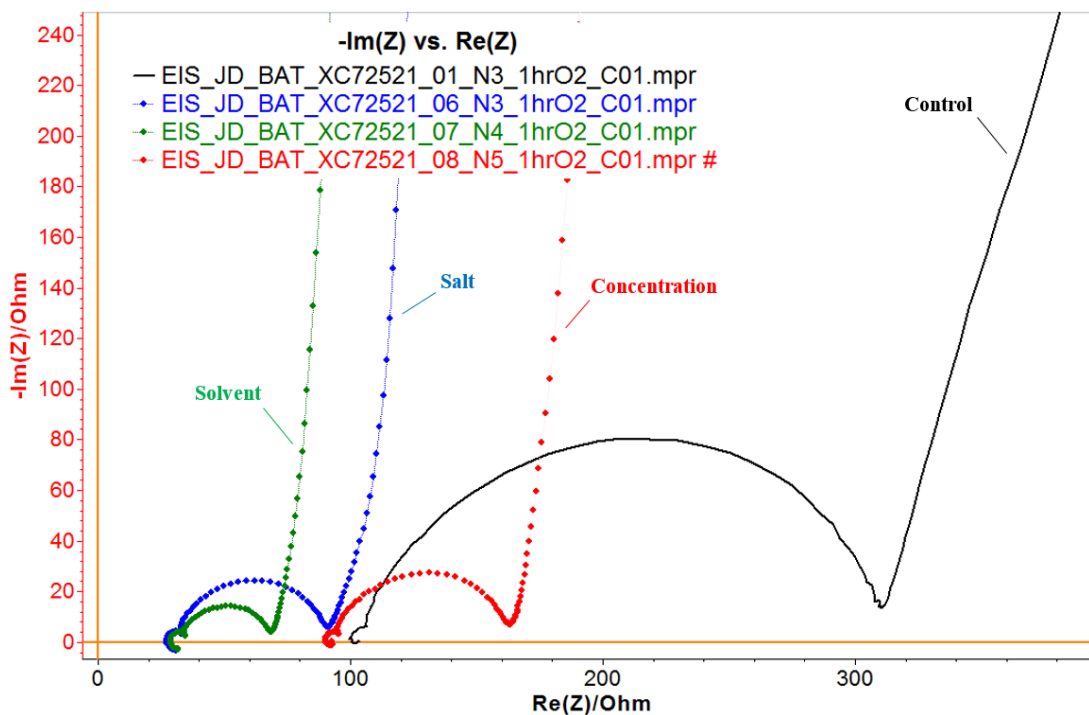
Figure 36: Impedance spectroscopy of samples with various electrolyte composition. The cathode in these cells was coated Vulcan XC72.

When comparing Figure 36 to Figure 35, the effect from the electrolyte shows very similar trends in the impedance even between the two different cathode materials. The slight variation present in this comparison is the lower capacitive impedance (demonstrated by the lower imaginary impedance on the Y-axis). The hypothesis may be associated with the loading of the cathode, the reactivity of the carbon material and the total carbon to binder ratio. Further testing is recommended to confirm the hypothesis behind this slight difference. Impedance measurements were also conducted on the discharged cells, as shown in Figure 37. The expected outcome of the test was a change in impedance related to the total specific capacity of the first discharge cycle and the yield of lithium peroxide.
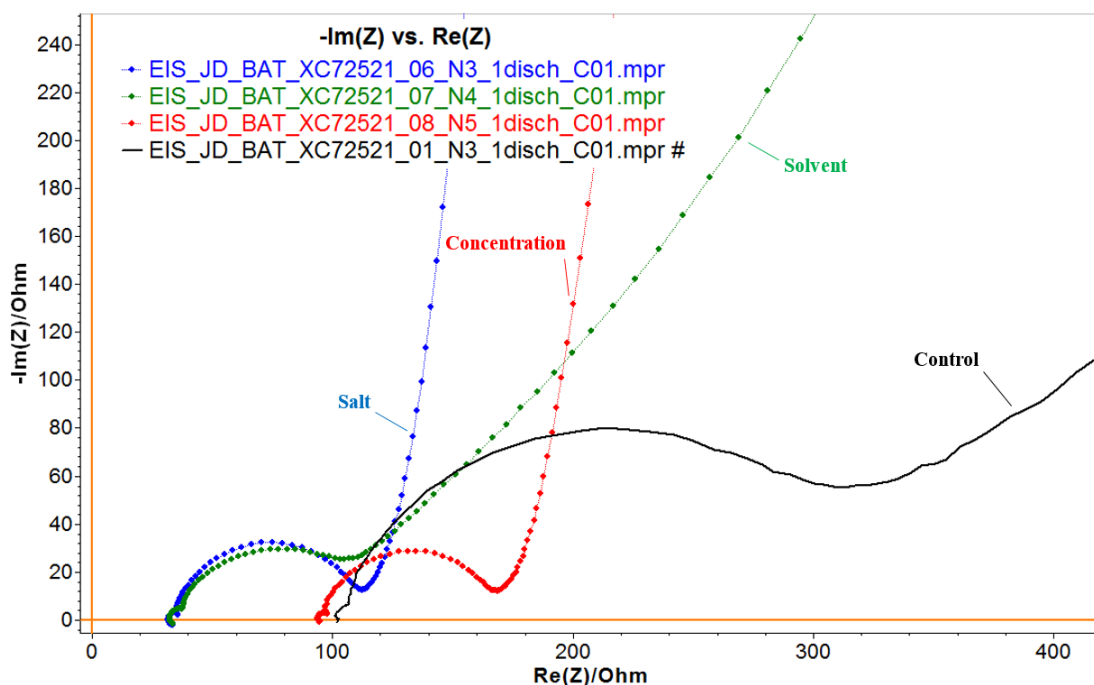
Figure 37: Impedance spectrum of samples with various electrolyte composition with Vulcan XC72 cathodes.

A minor increase in the capacitive impedance is observed but the foremost observation from the figure above is the distinct shift at low frequencies (high impedance). The Warburg impedance, characterized by the 45° slope at low frequency, is more significant in the samples with 1 M lithium triflate. In comparison, the samples with different salts or higher salt concentration show a more capacitive behavior, characterized by the steeper slope, at those frequencies. As previously discussed, this low frequency behavior is associated with lithium ion diffusion to the reaction sites. Thus, the second noteworthy observation that can be drawn from these samples is how an alternative salt or a higher concentration can reduce changes in the impedance of the cell. Moreover, the sample with a 1.5 M LiTf/4G shows a lower variation between the discharged and charge cell. Referring to Figure 28, the impedance at high frequencies correlates to the discharge capacity obtained from each sample. When comparing that to the peroxide yield, the samples with a more significant Warburg impedance have a higher lithium peroxide yield while the more

65

capacitive ones have lower yields. Further analysis between each test can be found in Chapter V.

iii.   Impedance after different testing conditions

The rate of discharge has been reported to affect the morphological formation of lithium peroxide [49]. However, the quantitative analysis of the peroxide formation has yet been reported. Thus, titration was conducted on a cell at higher discharge rate to assess the effect of the current density on the peroxide yield. The outcome of the test showed statistically higher yield at a higher current density (0.25 mAh/cm^2) – 78.1 % versus 70.9 %. The impedance of the discharged cell was also recorded to further understand the Li_2O_2 layer formation. A Nyquist plot between the control galvanostatic rate and the increase rate can be found in Figure 38.
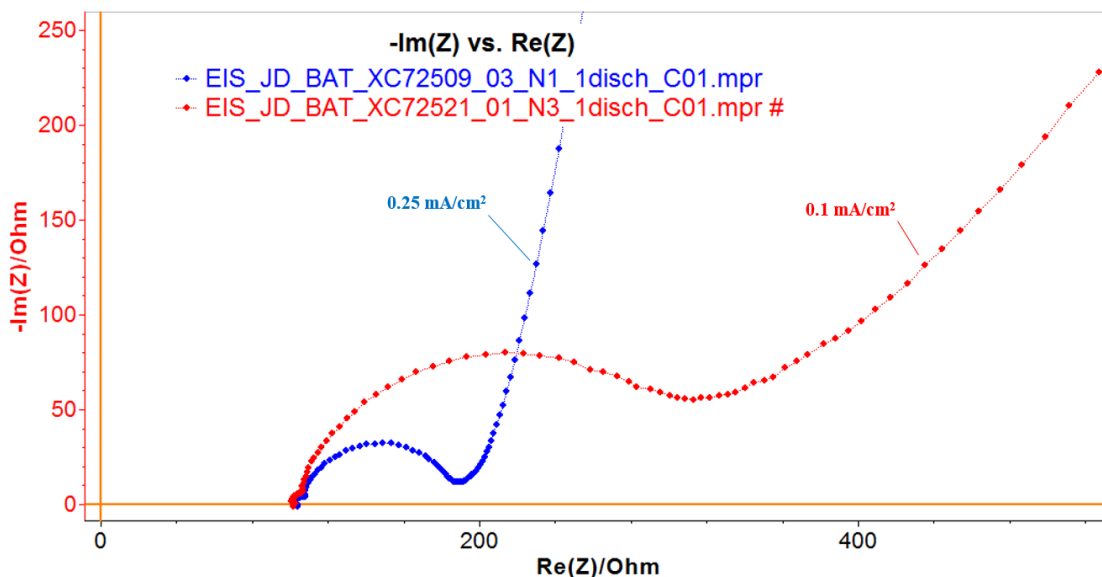
Figure 38: Impedance spectrum of discharged cells at various discharge rates.

The impedance from the fast discharge is drastically lower than the one from the control. Furthermore, the Warburg diffusion impedance is more noticeable at the lower discharge rate. Again, this is closely related to the total discharge capacity drawn from the cells (Figure 29). When compared to the titration data, this difference also correspond to the side reactions occurring in the cell. The increased impedance agrees with the formation of

insulating species in the cell. This behavior can be further confirmed when comparing the impedance of cells at their first and third discharge (refer to Chapter V.).

iv.   Additional EIS testing

The evolution of the impedance in the cells have been discussed in details in the previous sections of this chapter. In this subsection, the effects of various cell components are studied to provide further information on the factors of the observed evolution. Primarily, the low impedance semi-circle at high frequencies (below j5Ω) was a controversial topic in the literature. Adams et al. suggested that this high frequency response was associated with the ionic transfer at the lithium/electrolyte interface [52]. On the other hand, Mirzaeian et al. suggested that this response was related to the interfacial capacitance from an oxide surface film that increases with the carbon pore volume [50]. This theory was tested by comparing the impedance of pristine cells with carbons of various pore volume and surface area and very little variation across the samples suggests that the first semi-circle is independent of the carbon characteristics in this study. The following approach taken in this analysis was to determine the effect of the current collector in the overall impedance of the cell.

The current collector used for the majority of the study (Toray paper) was replaced with a stainless steel mesh of fine grade (500x500T0010W40T, TWP Inc.). The carbon material placed on both current collectors was 4:1 KB/PVDF layered from the same batch in parallel to neglect any processing variable. The electrolyte was kept consistent with 1 M LiTf/4G and both samples were soaked with 160 µL. As both materials have very different electrical property, the test was designed to assess the effect of the current collector on the impedance of the cell. The electrical resistivity is 80 mΩ·cm and 70 µΩ·cm for carbon paper and SS mesh respectively (manufacturer's specification). Since the electrical conductivity was increased with the SS mesh, the most significant changes were expected at high frequencies with the different carbon/current collector interface and/or the current collector/SS tube interface, used as electrical connection (refer to page 33). A zoom on the Nyquist plot of the high frequency response is shown in Figure 39.
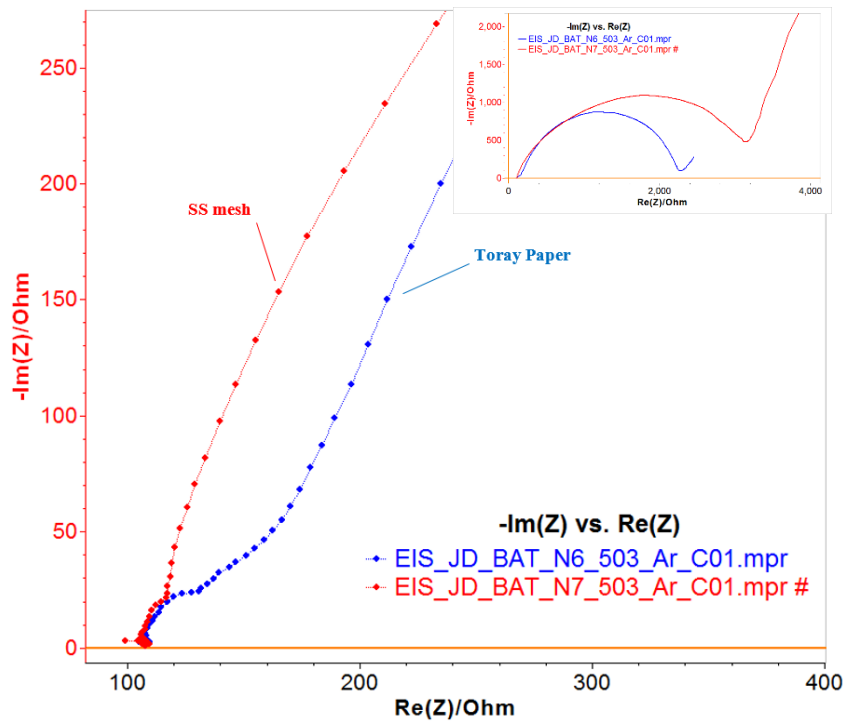
Figure 39: High frequency impedance plot for two cells with Ketjen Black carbon on different current collector. INSET: Full EIS spectrum.

The outcome of this EIS test showed evidence that the current collector has an effect on the impedance at high frequency. Moreover, this high frequency impedance was tested with a carbon-free Toray paper to determine if this response was related to the carbon to Toray paper interface. Since Figure 40 demonstrated otherwise, the last test conducted to establish the factors of this high frequency semi-circle was to test a carbon-coated Toray paper flipped over with the carbon layer facing the SS tube. This would assess whether the response is from the interface between the paper and the SS tube (used as electrode connection) or between the paper and the electrolyte. The presence of the high frequency response demonstrated by default that it was related to the interface between the electrolyte and the Toray paper.

68
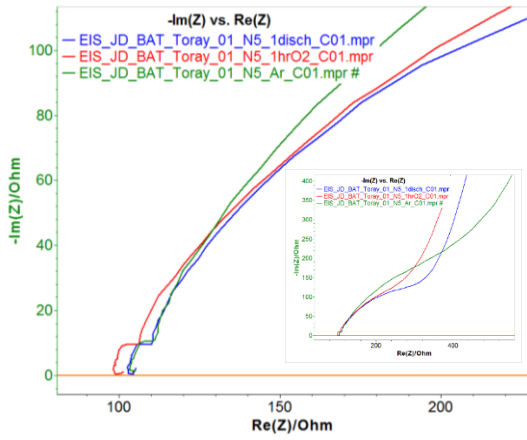
Figure 40: EIS of a full cell with carbon-free Toray paper. INSET: Full EIS spectrum.
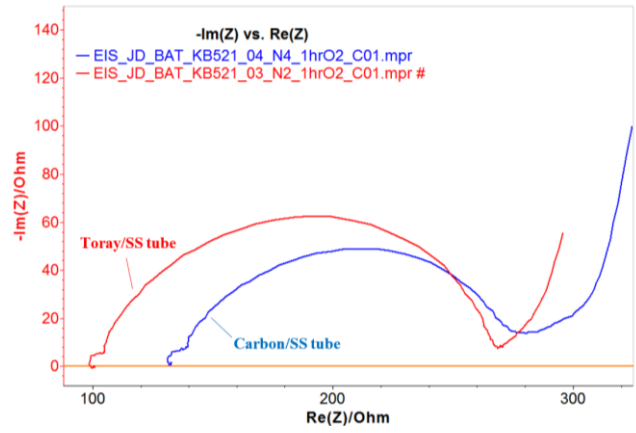
Figure 41: Impedance spectrum of two cells with the cathode position rotated to test interfaces on the current collector.

V. Discussion

The data presented in the previous section provides intriguing insights on complex lithium-oxygen batteries. Since the results are categorized by testing technique, preliminary trends in the data are discussed for each test separately (Results chapter) though no correlation between the data sets are discussed. Consequently, this chapter presents the different observations made from comparing the data of each testing techniques and addresses the questions defining this thesis. The discussion of the first question stated in the scope of work is divided into the first two section of this chapter. This allows to appropriately analyze the effect of the carbon material on the discharge capacity and the voltage profile separately. The second question concerning the lithium peroxide yield dependency on the carbon material is addressed in the third section. The correlation of the results to EIS data is commented both with respect to the discharge capacity and the Li_2O_2 yield of the battery in the fourth section. Finally, additional work for the extension of this work is suggested in the future work section of this chapter.

A. Carbon dependent capacity output

The carbon material demonstrated to affect the specific discharge capacity (refer to the Results chapter). However, some carbon materials showed performances below expectation and others showed improved performance. The first specific discharge capacity is plotted in terms of the carbon properties in Figure 42 and Figure 43. As the plots demonstrate, no clear trends can be drawn from this data. Thus, it suggests that the discharge capacity of $Li-O_2$ cells is not dependent only on the surface area and pore volume. A few contingencies with the data have to be considered. It is believed that cells with graphene nanoplatelets showed lower discharge capacity given its high surface area from the manufacturer's specifications. The hypothesis behind this result is that the graphene layers are too dense to allow fast ionic and gas diffusion to the active sites, suggesting that the material has small pore size. The sloped galvanostatic voltage profile presented earlier (refer to Figure 23) support this hypothesis.
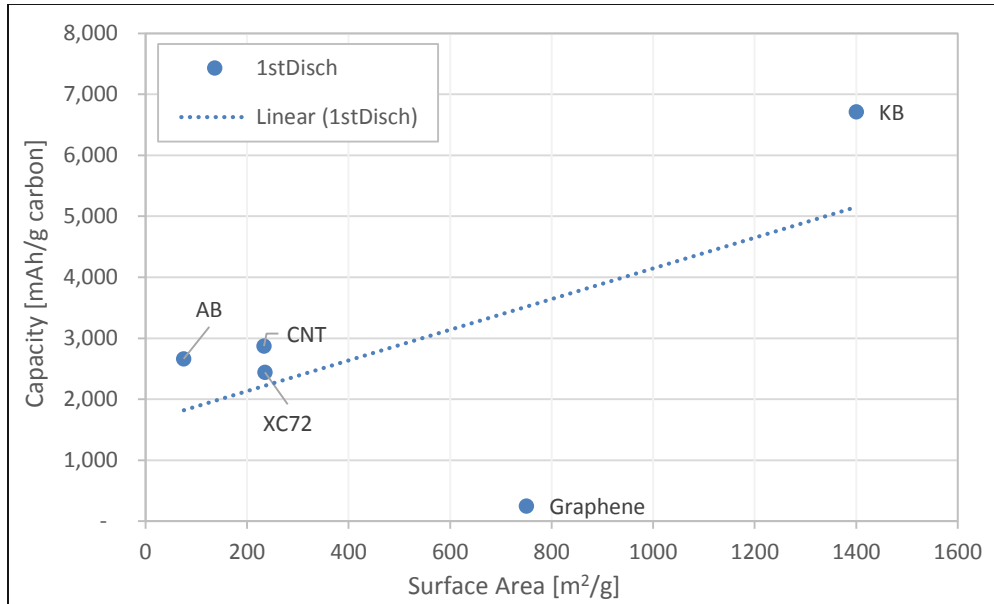
Figure 42: First discharge capacity for various carbon cathode in terms of surface area. The trend line is based on a linear fit.
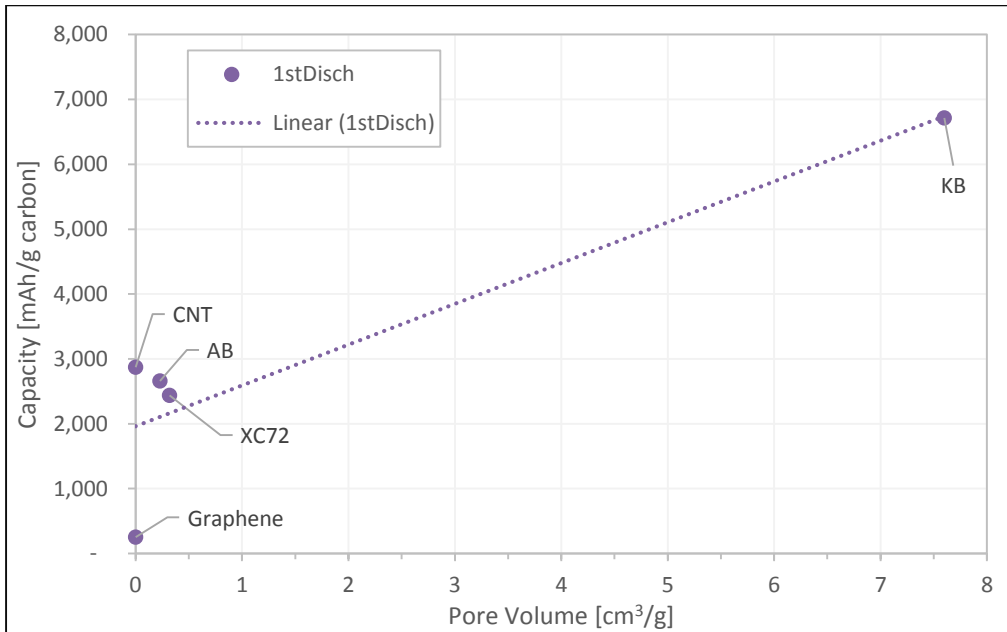
Figure 43: First discharge capacity for various carbon cathode in terms of pore volume. The trend line is based on a linear fit.

Although high pore volume provides high capacity to the battery, it becomes quickly clogged and the reaction side products partially filling those pores cannot be easily recycled [24, 38, 57]. Thus, pore size distribution becomes very important to avoid rapid capacity

drop with cycling. Another benefit of fully understanding the advantageous properties of the cathode material is to determine the qualities required to find an alternative material. This is especially important with recent publications confirming that carbon material may not be suitable for Li-O$_2$ cathodes [25, 34, 58].

B. Effect of carbons on voltage profile

Another observation taken from the galvanostatic cyclic test is the effect of carbons on the voltage profile. The carbon material is often associated with the performance and stability of a lithium-oxygen batteries [31, 34, 35, 57] though the voltage profiles are not often discussed in the literature. Previous results showed significant variation in the polarization of the cell when different carbon cathodes were tested. This section will focus on analyzing this variation and suggest a theory for it.

The polarization of batteries represents the effect of total internal impedance of the cells [8]. At rest, the experimental open circuit voltage (OCV) of lithium oxygen batteries approaches the redox potential of Li/Li$^+$ couple (3.06 V). As soon as the cells are exposed to a constant current load, the voltage drops rapidly to stabilize at potentials between 2.75 and 2.55 V. The interesting aspect shown in the data is that this voltage drop is repeatedly dependent on the carbon material. Table 6 shows the average values for the five carbon cathode studied in this work. The analysis of the data can be found on the next page.

Table 6: Average activation potential based on the theoretical redox potential of lithium of the first discharge of various carbon cathode.

Carbon Cathode	Activation potential
Graphene Nanoplatelets (Graphene)	470 mV
Multi-Walled Carbon Nanotubes (CNT)	380 mV
Vulcan XC72 (XC72)	440 mV
Ketjen Black (KB)	410 mV
Acetylene Black (AB)	480 mV

To aid the interpretation of this data, the voltage drop of cells with different current densities are tabulated in Table 7 showing more distinct changes in the data.

Table 7: Average activation potential based on the theoretical redox potential of lithium of the first discharge at different current density.

Current density	Activation potential
0.1 mA/cm^2	440 mV
0.25 mA/cm^2	550 mV

The first observation to be made is the 25 % increase in activation potential at higher current density, as expected [32]. This is due to lower effective concentrations of Li^+ and O_2 in the vicinity of electrode surface at higher current density [8]. Based on that observation, a different perspective can be taken on the tested carbon materials. In comparison to XC72, cathodes with CNT and KB have lower overpotential while graphene and acetylene black have a larger overpotential. This would imply that CNT and KB are two materials that relatively have higher reaction kinetics. EIS data, Li_2O_2 yield and material properties of the carbons were compared to this observation though no clear correlation with the different overpotentials could be drawn. Further work is suggested to investigate the effect from the actual surface area involved in the discharge and the surface properties of the carbon.

C. Lithium peroxide independency of the carbon material

Quantifying the Li_2O_2 yield in Li-O_2 battery has a great importance in understanding this complex system. By varying the carbon material in the cell, it was possible to analyze the effect of the carbon material on the yield of desired discharge product and determine how the carbon material affect the battery in general. As discussed in the first chapter, the carbon material has been demonstrated to affect the overall capacity of the battery and its cyclability. Although the carbon material affect specific energy from the battery, it is of great importance to quantify the capacity obtained from the formation of the desired discharge product in lieu of side products (see Experimental Work chapter).

The results presented in the previous chapter showed marginal deviation in the Li_2O_2 yield as the carbon material was varied. This observation suggests that the yield is independent of the carbon material and more specifically independent of its properties. The peroxide yield after the third discharge also demonstrated to be relatively consistent across the various carbon samples. This further suggests the Li_2O_2 yield independency of the carbon material. Additional tests on the electrolyte composition also suggested that the stability of the electrolyte is a bigger concern than that of the cathode composition.

The results and observation from this analysis highlights a new perspective on the effect of the carbon material on the stability of $Li-O_2$ batteries. As the data illustrate, the electrolyte composition shows a larger effect on yield of the desired discharge product and carbon material is shown to have minimal effect on the Li_2O_2 yield.

D. State-of-charge characterization using EIS

The second-to-last objective defining this thesis is to correlate the impedance spectrum of various batteries with their discharge capacity. Thus, a test was designed to collect impedance spectra throughout one discharge cycle with the objective to observe the evolution of the impedance as the cell is being discharged. The impedance spectrum of the cell was collected at three specific points during the first discharge: start, middle and end of the discharge (Figure 44). The impedance measurement in the middle of the cycle was conducted at open circuit voltage after a 20 minute rest to avoid voltage drift through the EIS test. The final EIS measurement was conducted after one hour of rest to allow the voltage to return to OCV. The reason of the rest time to be different is the voltage at which the rest started at (end of the cycle being at 2.0 V). The three impedance spectrum can be found in Figure 45. As expected, the high frequency response remains consistent throughout the cycle. The buildup of discharge product is found to affect the lower frequency and more specifically the relationship between the diffusion rates and the carbon/electrolyte interface. The shift in impedance can also be observed with the other cells tested in this thesis confirming that this shift is clearly related to the accumulation of discharge product (see Figure 31 and Figure 32).
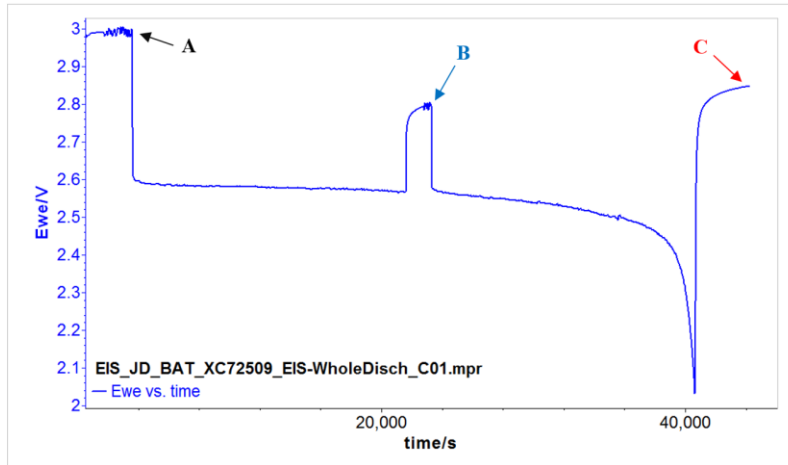
Figure 44: Discharge profile of a cell that was tested with EIS in the middle of the cycle. EIS at point A assessed the pristine cell after 2 hours of oxygen gas exposure. EIS at point B was taken in the middle of the discharge and point C shows EIS at the end of the first discharge.
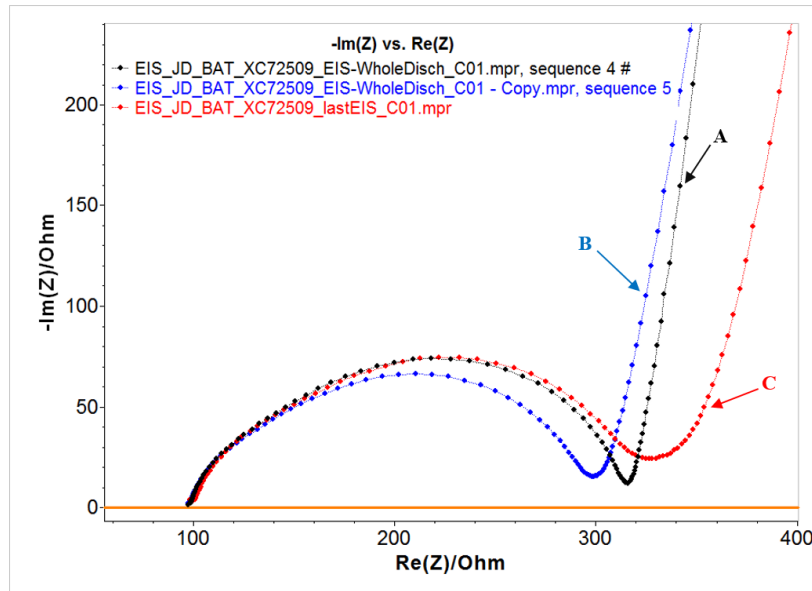
Figure 45: Impedance spectrum at different points of the discharge cycle: start (A), middle (B) and end (C) of the cycle.

Nevertheless, characterizing the impedance evolution in terms of state-of-charge and discharge capacity requires an extensive analysis of the equivalent model. A preliminary analysis of the different section on the impedance spectrum was pursued and can be found in the appendices. However, it was found that additional testing on the various components of the battery was required to appropriately propose a complete equivalent model.

75

E. Lithium peroxide characterization

The last topic to be discussed is this chapter is the correlation between the lithium peroxide yield in a cell and the other two tests used in this work – galvanostatic cycling and EIS. As previously discussed, the titration was used to quantify lithium peroxide present in a cell is a post-mortem test. This implies that each sample must be terminated to test the Li_2O_2 yield and discharge cannot be resumed afterward. Thus, this section attends to correlate this yield with post-mortem techniques.

The first approach taken was to compare the wide range of yield from the samples with various electrolyte compositions. Below is a figure with the respective peroxide yield (Figure 46). The correlation seems quite obvious: a steeper diffusion slope shows lower yields. Both the control (black) and the alternate solvent (green) cells experienced higher yields than the other two samples and they both seemed to have a lower slope. At first, the theory for this observation was that the higher ratio of lithium peroxide to other insulating discharge product would make the diffusion rate more resistive than capacitive (lower diffusion slope). However, the higher specific capacity of those samples also followed the same trend making this theory non-conclusive. This theory was applied to the samples of different discharge rates (Figure 47). The trend completely disagreed with the theory as the faster discharge sample showed a steeper slope and higher lithium peroxide yield. This difference in impedance could be associated with the quantity of lithium peroxide present but also with its morphology at different current density [49]. Consequently, the impedance spectrum of each carbon cathode was compared to the lithium peroxide yield of each cell, as shown in Figure 48. Once more, no correlations were found and the proposed theory was found to disagree with the data. The following approach was to confirm that the theory is not carbon dependent – implying that the diffusion slope could only be compared between the same carbon cathodes. Thus, the impedance spectrum of Vulcan XC72 carbon after the first discharge was compared to the measured peroxide yield. Figure 49 shows the EIS data and the lithium peroxide yield of four identical cells with Vulcan XC72 cathodes. Again, another trend can be observed between those cells.
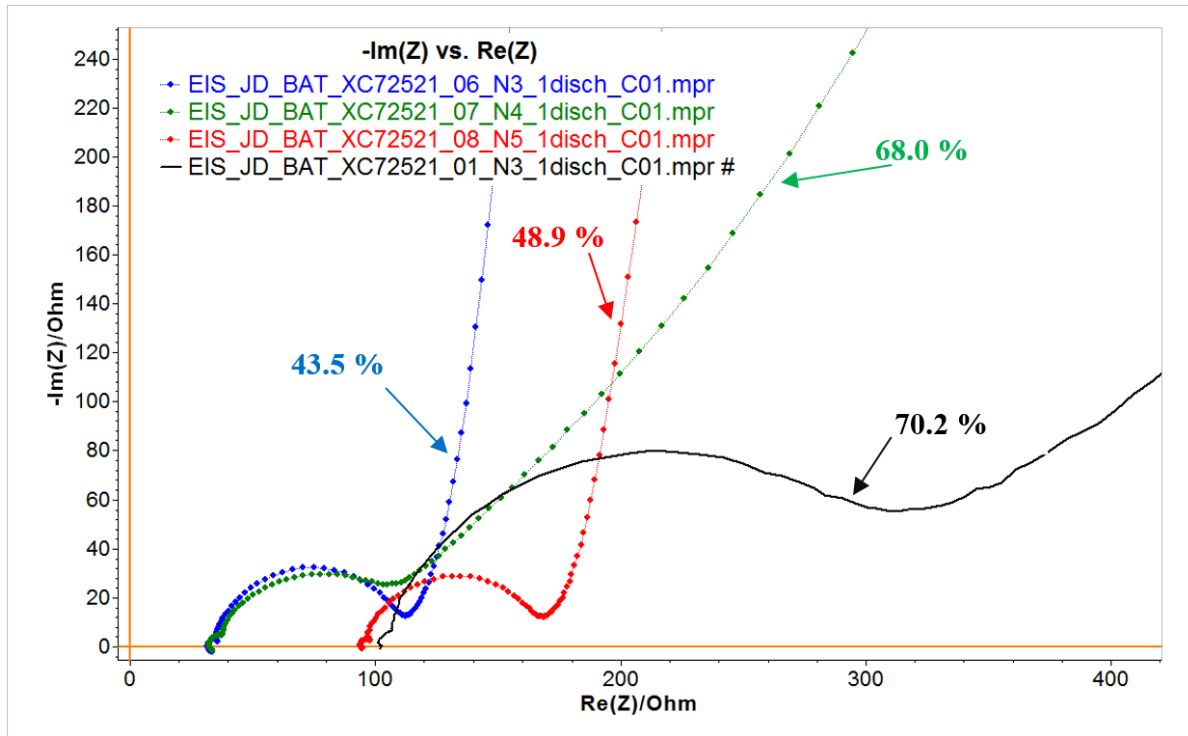
Figure 46: Lithium peroxide yield associated to the EIS data for cells with different electrolyte composition: 1 M LiTf/4G (black), 1 M LiTf/DME (green), 1 M LiTFSI/4G (blue) and 1.5 M LiTf/4G (red).
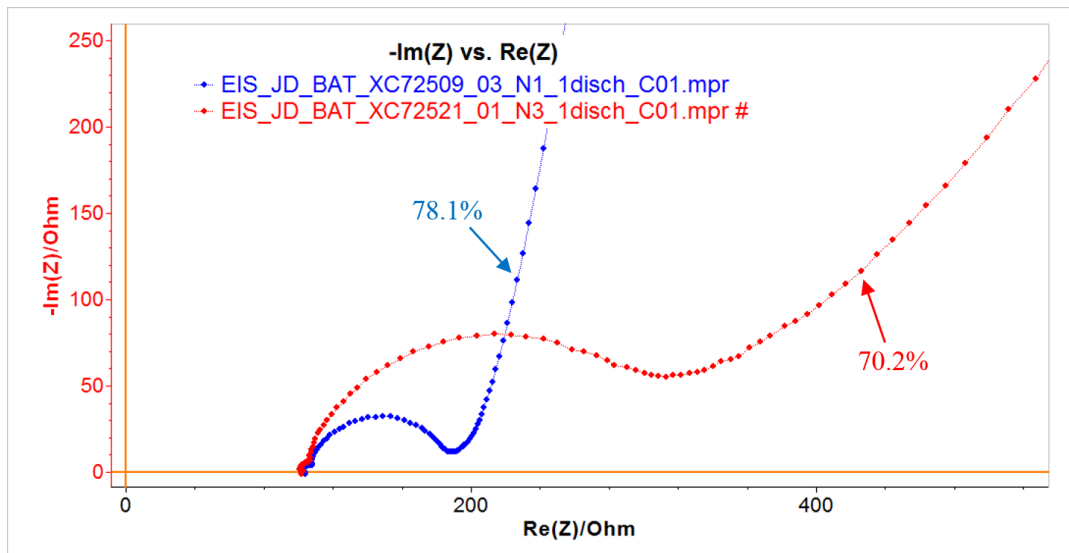
Figure 47: Lithium peroxide yield associated to the EIS data for cells with different current densities: 0.1 mA/cm^2 (red) and 0.25 mA/cm^2 (blue).
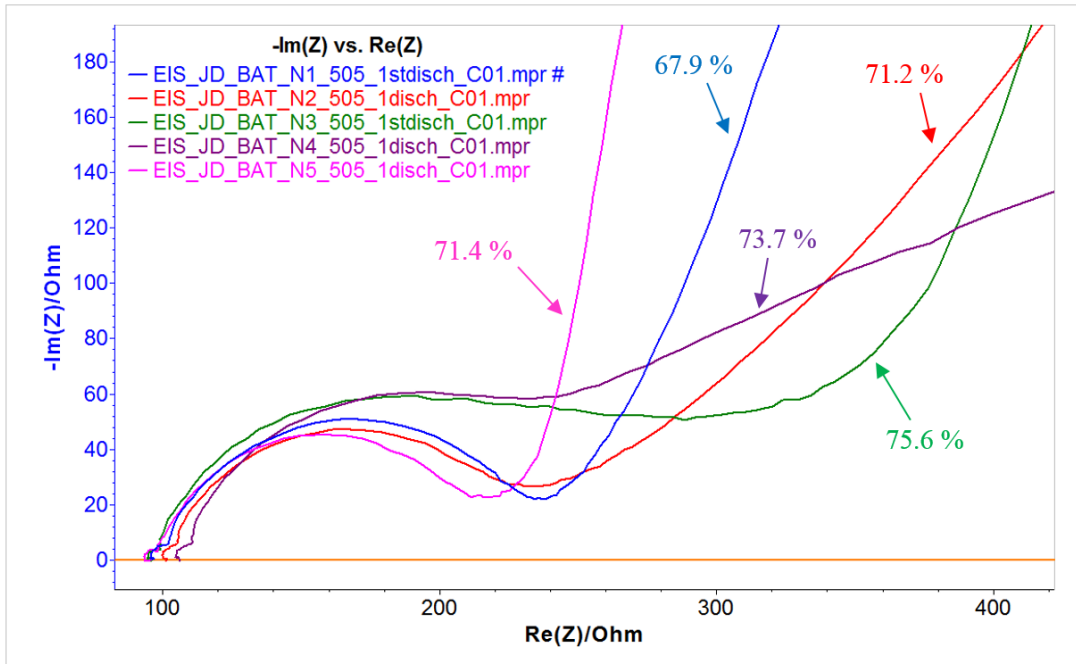
Figure 48: Lithium peroxide yield associated to the EIS data for cells with different carbon cathode. Graphene nanoplatelets (Blue). Multi-walled carbon nanotubes (Red). Vulcan XC72 (Green). Ketjen Black (Purple). Acetylene Black (Pink).
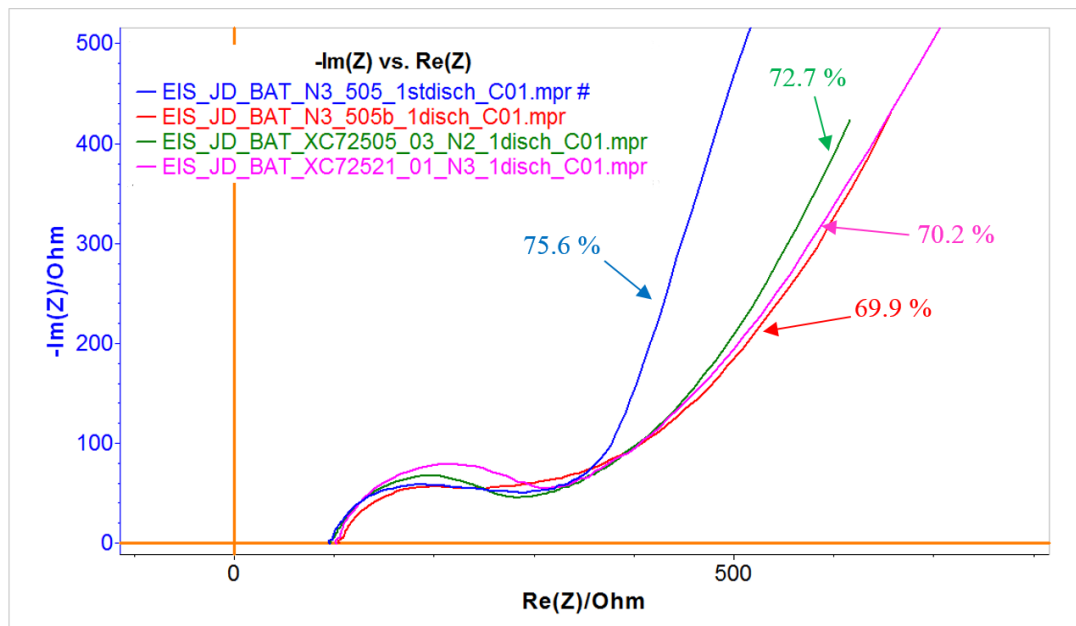
Figure 49: Lithium peroxide yield associated to the EIS data for identical cells with XC72 cathodes.

When comparing the four previous plots to one-another, no clear correlation between the cell's impedance spectrum and the yield of lithium peroxide yield can be made at this time. Isolating variation in the samples – such as loading, time between EIS and titration testing, oxygen pressure, purity of the glovebox or cell assembly – may highlight the ratio of lithium peroxide to other discharge product in the EIS data.

F. Future Work

A number of future directions have already been discussed in the previous section. Extension on the presented research should allow to confirm some of the hypothesis presented in the discussion area. For instance, additional variation on the cell composition could further characterize the lithium peroxide formation mechanisms. This section highlights techniques and cell compositions that could be pursued in the Oregon Tech Wilsonville laboratories given the equipment and materials available.

i. Laboratory station improvements

The first work presented in this thesis was the establishment of a laboratory station. Although its practicality was presented with the lithium-oxygen battery research, a few improvements are recommended in this section to better take advantage of the system.

Moisture ingress was remedied with a moisture capture system that can be easily regenerated over time. On the other hand, oxygen has not been able to be consistently removed without purging the chamber. This lack results in the large consumption of argon gas over time which could jeopardize the utility of the system. Designing a stand-alone, similar to the one for moisture, would remarkably reduce the argon gas required to maintain an operational system. A system without any oxygen may be challenging to obtain but a simple low cost design could provide sufficient capabilities.

The other improvement to the inert environment system is associated with the instrumentations. As discuss in Chapter II, the moisture, oxygen and pressure controllers have the capability to output an additional signal at programmable limits. By combining those signals into a central controller, the system could be automated to maintain

operational impurity levels. Limits on the oxygen and moisture concentration could trigger an automatic purge from the pressure controller. Additionally, these signals could be used to remotely monitor the performance of the system.

The two improvements on the laboratory station are strongly recommended to be pursued for their high practicality and low cost factors. Both of them would benefit current and future students requiring this type of equipment.

    ii.   Expansion on the current study

The expansion of the presented study could further confirm the proposed theories and observations. Besides the cathode material, characterization of the lithium peroxide could also be pursued with different electrolyte composition or testing condition. The solvent as well as the salt in the electrolyte were demonstrated in this work to affect drastically the lithium peroxide yield at the first discharge. Determining the optimized electrolyte properties with specific carbon cathodes could provide valuable insights on the carbon/electrolyte interface. High Li_2O_2 yield was also experienced in cells with a higher current density. Investigating the yield at various discharge rate and compare that to the capacity obtained from the cells could help understand the limits of the diffusion rates of lithium ion and oxygen gas.

Electrochemical impedance spectroscopy on Swagelok cells was pursued in this work. Three separate models were proposed for each range of impedance response. However, a combined model was found to be outside the scope of the work. Further characterization of the reaction mechanisms may help establish a full cell model that would simulate the formation of discharge products. Additionally, the impedance spectrum could be correlated to the lithium peroxide yield to allow non-post-mortem yield assessment.

    iii.   Cyclic voltammetry

One of the techniques found to be quite powerful but not performed during this thesis work was cyclic voltammetry (CV). The technique consists of a voltage sweep within a desired voltage window continuously measuring the current response. Generally speaking, the

outcome of this electrochemical technique is often used in the battery field to highlight reversible couples desired for the development of secondary batteries. Since lithium oxygen cells have complex reactions, this technique has been excessively used to analyze multiple reduction and oxidation reactions in the system [49, 61, 62].

A simple CV test was performed in the laboratory to demonstrate the potential of the technique. A simple three electrode air-tight cell was design to allow the connection of three independent electrodes and an additional variable oxygen gas supply. Figure 50 demonstrates the whole apparatus used for the test with a carbon working electrode and two separate lithium counter and reference electrodes.
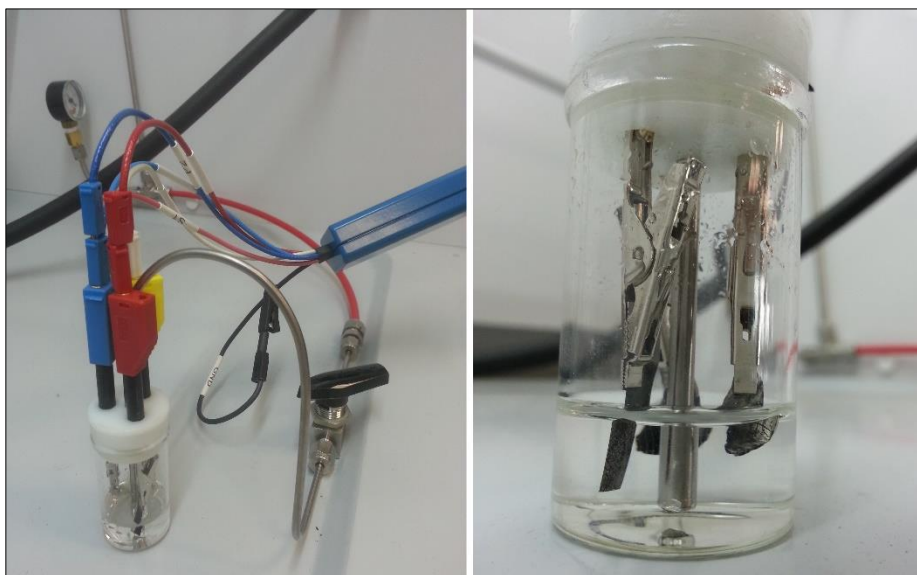
Figure 50: LEFT: Cyclic Voltammetry apparetus displaying the three electrode connections and the oxygen supply valve. RIGHT: Carbon working electrode and two lithium counter and reference electrodes.

The carbon electrode was prepared with the same method as previously discussed on a stainless steel mesh. The counter and reference electrodes were ~0.5 cm^2 lithium foil. The electrolyte used in this test was a 1.0 M LiTf in tetraglyme (4G). The cell was assembled inside the glovebox prior to testing it in a fume hood. The oxygen supply had a laboratory grade purity of 99.95% and was bubbled at a high rate for approximately an hour prior to collecting adequate data at a lower rate. It was found that the disturbance by the oxygen bubbling was providing noise in the data.

The testing conditions were adapted from the literature [59] by decreasing the voltage window (1.5 V – 4.0V) to avoid effects from the decomposition of the electrolyte. Data was collected over 200 cycles to observe the time dependency of the test and observe the evolution of the reaction peaks, as shown in Figure 51. Data at various scan rates were also collected to detect any relationships. A plot of two sample rates CV sweep as well as a plot of the anodic peaks at each rates (INSET) can be found in Figure 52.
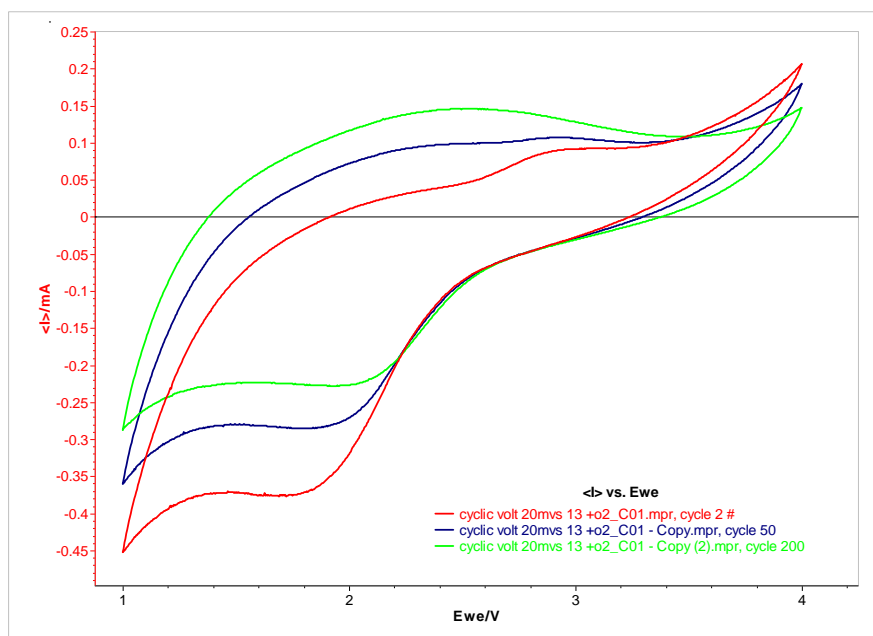
Figure 51: Cyclic Voltammetry. Voltage sweep of the same cell at 20 mV/s over numerous cycles: 2nd cycle (RED), 50th cycle (BLUE) and 200th cycle (GREEN)
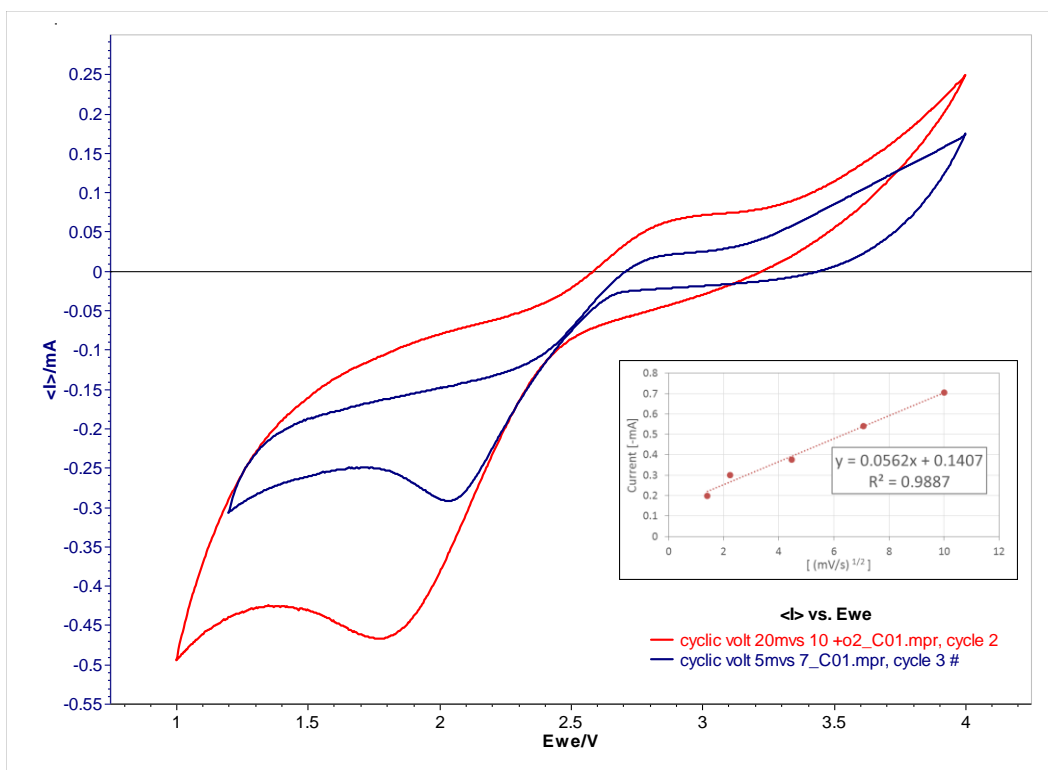
Figure 52: Cyclic Voltammetry Analysis. Repeated voltage sweep at two different rates: 5mV/s (RED) and 20mV/s (GREEN). INSET: Anodic peaks magnitude plots vs. the square root voltage sweep rate.

The reason this technique was not pursued in this work is due to the lack of electrical measurement feed-through in the glovebox. This technique is very powerful when a baseline control is conducted. For that reason, a cyclic voltammetry test in an argon environment would allow to assess the effect of the oxygen in the overall reaction. Without this baseline, it is challenging to associate any of the reaction peaks with the presence of oxygen. A simplistic electrical feed through was explored at the initial set up of the laboratory station though was found to be leak-prone. The initial design constituted of three separate stranded copper wires inside a small ¼" tube on the spare port on the glovebox. Through methodological observations, it was found that the leaks were too significant to maintain the pressure and the oxygen/moisture concentration. Additional testing with solid copper wire may prove to serve the purpose. The suggested work would be very powerful when applied to electrolyte composition studies and/or mediators (later discussed).

83

iv.   Additives

As observed in this study, the lithium oxygen battery can experience large under-potential and over-potential for the reaction to take place. This polarization can be detrimental for the chemistry of the battery because it often approaches the limits of the potential window of the electrolyte. The use of catalysts in lithium oxygen have shown to improve the voltage profile of lithium-oxygen batteries [19, 63]–[66]. However, the performance of catalysts in lithium oxygen batteries has yet been studied in terms of lithium peroxide yield. The suggested work would be to assess how catalyzers affect the lithium peroxide yield at different cycles.

Redox mediators facilitate the reactions within the cell similarly to catalysts. However, a mediator differs from a catalyst by where it is incorporated in the cell. As part of the electrolyte, a redox mediator is mainly used to aid the charge transport between the Li_2O_2 and the cathode surface by acting as an electron transfer agent [48]. During the charging cycle, the mediator is oxidized at the cathode material to then be reduced by the lithium peroxide. This process facilitates the oxidation of the lithium peroxide. A study by Peter Bruce's group [48] demonstrated how the introduction of a redox mediator would allow fast rate charging (1 mA/cm^2) at voltage slightly above 3.5 V. The characterization of the performance of this additive provided extensive insights on the kinetics of the reactions. The study mainly focused on nanoporous gold cathodes and briefly discusses the carbon cathode. One direction of future work would be to assess if the lithium peroxide yield in lithium oxygen systems with a redox mediator can be maintained over a number of cycles. The data presented in this study showed a rapid decrease of the Li_2O_2 yield after only three cycles.

VI. Conclusion

As discussed in the first chapter, the Li-O$_2$ battery has a great potential in the next generation of batteries. Their theoretical energy densities have shown to surpass any other types of energy storage system making it very attractive for portable energy storage. However, the contingency in making this technology commercial is primarily its stability over multiple cycle. From a literature review, multiple factors have been discussed to be the source of this instability. Furthermore, it is believed that the chemical stability of the electrolyte and cathode material are the two main components that have caused instability in the system. The aim of this dissertation has been to characterize the lithium peroxide formation in lithium oxygen battery electrodes in terms of the carbon material. Five carbon materials with different morphology, surface area and pore volume have been studied to better understand the effect of the material on the electrochemical reaction of Li-O$_2$ batteries. Three techniques (galvanostatic cycling, iodometric titration and EIS) were used to assess the discharge capacity, Li$_2$O$_2$ yield and impedance spectrum of each sample.

The nature of Li-O$_2$ battery research required delicate and precise laboratory equipment. Thus, this thesis has discussed the establishment of a new laboratory at the Oregon Tech Wilsonville campus. Featuring cathode preparation station, a refurbished glovebox and a battery cycling station, the laboratory shows innovative alternative solutions to a specialized state-of-the-art laboratory. The design decisions, based on available equipment and finite budget, and the performance verification of the laboratory stations have been presented in this dissertation to validate the results of the study. Given the laboratory parameters, the testing techniques were adapted to provide accurate, repeatable and significant measurements.

The key outcomes of this dissertation are highlighted below:

   a. The carbon material has been demonstrated to have a direct effect on the discharge capacity of the battery as expected. Although the surface area and pore volume of the carbon show to be a factor of the total discharge capacity, a direct correlation

cannot be suggested as it is suspected that other factors, such as pore size distribution and surface chemistry, are affecting the discharge capacity of the battery.

b. The yield of lithium peroxide in a discharged cell has been demonstrated to be relatively independent of the carbon material both after the first and third discharge. Furthermore, the electrolyte has been shown to have a greater effect on the Li_2O_2 yield after the first discharge. As discussed in chapter V., these observations suggests that the carbon material is not responsible for the instability in $Li\text{-}O_2$ battery.

c. Iodometric titration has also showed the presence of Li_2O_2 in a charge cell (4.55V), contrary of the literature [39].

d. The impedance spectrum of various cells has been shown to be closely related to the total discharge capacity of battery though no correlation to the Li_2O_2 yield was found at this time.

As discussed earlier, the finding on the Li_2O_2 yield independency from the carbon material has been the key contribution to the literature. The lack of stability in the $Li\text{-}O_2$ cell has often been associated with the carbon cathode and the electrolyte. From this study, the stability of the carbon material is shown to have negligible effect on the desired discharge product suggesting that the electrolyte has a greater impact on the lithium peroxide yield.

Although the outcome of this study did not present an improved system, its purpose was to further understand the nature of the degradation product in $Li\text{-}O_2$ batteries. As the origin of the instability of the system is further characterized, a practical oxygen battery can be designed to meet the technological demand of portable energy storage. Foremost, a stable lithium-air battery would drastically improve the advantages of electrical vehicles by providing a light and relatively affordable mean of storing energy.

VII. References

[1]   G. Craptree, "JCESR: One Year Later," in *Material Research Society*, 2014.

[2]   R. Rapier, "The Surprising Reason That Oil Subsidies Persist: Even Liberals Love Them," *Forbes*, 25-Apr-2012.

[3]   ARPAE, "Advanced Research Projects Agency - Energy," 2014. [Online]. Available: http://arpa-e.energy.gov/.

[4]   ARPAE, "Batteries for Electrical Energy Storage in Transportation," 2014. [Online]. Available: http://arpa-e.energy.gov/?q=arpa-e-programs/beest.

[5]   T. Reddy, *Linden's Handbook of Batteries, 4th Edition*. 2010, p. 1200.

[6]   A. K. Padhi, K. S. Nanjundaswamy, and J. B. Goodenough, "Phospho-olivines as Positive-Electrode Materials for Rechargeable Lithium Batteries," *J. Electrochem. Soc.*, vol. 144, no. 4, pp. 1188–1194, 1997.

[7]   J. Christensen, P. Albertus, R. S. Sanchez-Carrera, T. Lohmann, B. Kozinsky, R. Liedtke, J. Ahmed, and A. Kojic, "A critical review of Li/air batteries," *J. Electrochem. Soc.*, vol. 159, no. 2, pp. R1 − R30, 2012.

[8]   D. Linden and T. B. Reddy, *HANDBOOK OF BATTERIES*, 3rd Editio. McGraw-Hill.

[9]   J. B. Goodenough and Y. Kim, "Challenges for rechargeable batteries," *J. Power Sources*, vol. 196, no. 16, pp. 6688–6694, Aug. 2011.

[10]   J. B. Goodenough, "Cathode materials: A personal perspective," *J. Power Sources*, vol. 174, no. 2, pp. 996–1000, Dec. 2007.

[11]   J. P. Zheng, R. Y. Liang, M. Hendrickson, and E. J. Plichta, "Theoretical energy density of Li-air batteries," *J. Electrochem. Soc.*, vol. 155, no. 6, pp. A432 − A437, 2008.

[12]   G. Girishkumar, B. McCloskey, a. C. Luntz, S. Swanson, and W. Wilcke, "Lithium-air battery: Promise and challenges," *J. Phys. Chem. Lett.*, vol. 1, no. 14, pp. 2193–2203, Jul. 2010.

[13]   J. Dahn, "Electrically Rechargeable Metal-air Batteries Compare to Advanced Lithium-ion Batteries," 2011, pp. 1–52.

[14] C. O. Laoire, S. Mukerjee, K. M. Abraham, E. J. Plichta, and M. A. Hendrickson, "Influence of nonaqueous solvents on the electrochemistry of oxygen in the rechargeable lithium- air battery," *J. Phys. Chem. C*, vol. 114, no. 19, pp. 9178–9186, 2010.

[15] Z. Peng, S. a Freunberger, Y. Chen, and P. G. Bruce, "A reversible and higher-rate Li-O2 battery.," *Science*, vol. 337, no. 6094, pp. 563–6, Aug. 2012.

[16] S. a Freunberger, Y. Chen, N. E. Drewett, L. J. Hardwick, F. Bardé, and P. G. Bruce, "The lithium-oxygen battery with ether-based electrolytes.," *Angew. Chem. Int. Ed. Engl.*, vol. 50, no. 37, pp. 8609–13, Sep. 2011.

[17] K. M. Abraham and Z. Jiang, "Polymer electrolyte-based rechargeable lithium/oxygen battery," *J. Electrochem. Soc.*, vol. 143, no. 1, pp. 1–5, 1996.

[18] J. Read, "Ether-based electrolytes for the lithium/oxygen organic electrolyte battery," *J. Electrochem. Soc.*, vol. 153, no. 1, pp. A96 – A100, 2006.

[19] T. Ogasawara, A. Debart, M. Holzapfel, P. Novak, and P. G. Bruce, "Rechargeable Li2O2 electrode for lithium batteries," *J. Am. Chem. Soc.*, vol. 128, no. 4, pp. 1390–1393, 2006.

[20] F. Mizuno, S. Nakanishi, Y. Kotani, S. Yokoishi, and I. Hideki, "Rechargeable li-air batteries with carbonate-based liquid electrolytes," in *Electrochemistry*, 2010, vol. 78, no. 5, pp. 403–405.

[21] N. Imanishi, S. Hasegawa, T. Zhang, A. Hirano, Y. Takeda, and O. Yamamoto, "Lithium anode for lithium-air secondary batteries," *J. Power Sources*, vol. 185, no. 2, pp. 1392–1397, Dec. 2008.

[22] G. Yu. Aleshin, D. A. Semenenko, A. I. Belova, T. K. Zakharchenko, D. M. Itkis, E. A. Goodilin, and Y. D. Tretyakov, "Protected anodes for lithium-air batteries," *Solid State Ionics*, vol. 184, pp. 62–64, 2011.

[23] T. Zhang, N. Imanishi, S. Hasegawa, A. Hirano, J. Xie, Y. Takeda, O. Yamamoto, and N. Sammes, "Water-Stable Lithium Anode with the Three-Layer Construction for Aqueous Lithium–Air Secondary Batteries," *Electrochemical and Solid-State Letters*, vol. 12. p. A132, 2009.

[24] A. Kraytsberg and Y. Ein-Eli, "Review on Li-air batteries - Opportunities, limitations and perspective," *J. Power Sources*, vol. 196, no. 3, pp. 886–893, 2011.

[25] B. D. McCloskey, A. Speidel, R. Scheffler, D. C. Miller, V. Viswanathan, J. S. Hummelshøj, J. K. Nørskov, and A. C. Luntz, "Twin Problems of Interfacial Carbonate Formation in Nonaqueous Li–O 2 Batteries," *J. Phys. Chem. Lett.*, vol. 3, no. 8, pp. 997–1001, Apr. 2012.

[26] Y.-C. Lu, B. M. Gallant, D. G. Kwabi, J. R. Harding, R. R. Mitchell, M. S. Whittingham, and Y. Shao-Horn, "Lithium–oxygen batteries: bridging mechanistic understanding and battery performance," *Energy Environ. Sci.*, vol. 6, no. 3, p. 750, 2013.

[27] E. Nasybulin, W. Xu, M. H. Engelhard, Z. Nie, S. D. Burton, L. Cosimbescu, M. E. Gross, and J. Zhang, "Effects of electrolyte salts on the performance of Li-O2 batteries," *J. Phys. Chem. C*, vol. 117, no. 6, pp. 2635–2645, 2013.

[28] W. Walker, V. Giordani, J. Uddin, V. S. Bryantsev, G. V Chase, and D. Addison, "A Rechargeable Li − O 2 Battery Using a Lithium Nitrate /," *J. Am. Chem. Soc.*, vol. 135, pp. 3–6, 2013.

[29] B. D. Adams, C. Radtke, R. Black, M. L. Trudeau, K. Zaghib, and L. F. Nazar, "Current density dependence of peroxide formation in the Li–O2 battery and its effect on charge," *Energy Environ. Sci.*, vol. 6, p. 1772, 2013.

[30] B. D. McCloskey, D. S. Bethune, R. M. Shelby, G. Girishkumar, and A. C. Luntz, "Solvents critical role in nonaqueous Lithium-Oxygen battery electrochemistry," *J. Phys. Chem. Lett.*, vol. 2, pp. 1161–1166, 2011.

[31] W. Xu, J. Hu, M. H. Engelhard, S. A. Towne, J. S. Hardy, J. Xiao, J. Feng, M. Y. Hu, J. J. Zhang, F. Ding, others, and M. E. Gross, "The Stability of Organic Solvents and Carbon Electrode in Nonaqueous Li-O< sub> 2</sub> Batteries," *J. Power Sources*, vol. 215, pp. 240–247, 2012.

[32] C. Ó. O. Laoire, S. Mukerjee, E. J. Plichta, M. A. Hendrickson, and K. M. Abraham, "Rechargeable lithium/TEGDME-LiPF6/O2 battery," *J. Electrochem. Soc.*, vol. 158, no. 3, pp. A302 − A308, 2011.

[33] M. M. Ottakam Thotiyl, S. a Freunberger, Z. Peng, and P. G. Bruce, "The carbon electrode in nonaqueous Li-O2 cells.," *J. Am. Chem. Soc.*, vol. 135, no. 1, pp. 494–500, Jan. 2013.

[34] S. Meini, M. Piana, H. Beyer, J. Schwammlein, and H. a. Gasteiger, "Effect of Carbon Surface Area on First Discharge Capacity of Li-O2 Cathodes and Cycle-Life Behavior in Ether-Based Electrolytes," *J. Electrochem. Soc.*, vol. 159, no. 12, pp. A2135–A2142, Oct. 2012.

89

[35] J.Read and J. Read, "Characterization of the lithium/oxygen organic electrolyte battery," *J. Electrochem. Soc.*, vol. 149, no. 9, pp. A1190 – A1195, 2002.

[36] J. Xiao, D. Wang, W. Xu, D. Wang, R. E. Williford, J. Liu, and J.-G. Zhang, "Optimization of Air Electrode for Li'Air Batteries," *J. Electrochem. Soc.*, vol. 157, no. 4, pp. A487–A492, 2010.

[37] J. Xiao, D. Mei, X. Li, W. Xu, D. Wang, G. L. Graff, W. D. Bennett, Z. Nie, L. V Saraf, I. a Aksay, J. Liu, and J.-G. Zhang, "Hierarchically porous graphene as a lithium-air battery electrode," *Nano Lett.*, vol. 11, no. 11, pp. 5071–5078, 2011.

[38] D. Wang, J. Xiao, W. Xu, and J.-G. Zhang, "High capacity pouch-type Li-air batteries," *J. Electrochem. Soc.*, vol. 157, no. 7, pp. A760 – A764, 2010.

[39] B. D. McCloskey, A. Valery, A. C. Luntz, S. R. Gowda, G. M. Wallraff, J. M. Garcia, T. Mori, and L. E. Krupp, "Combining Accurate O2 and Li2O2 Assays to Separate Discharge and Charge Stability Limitations in Nonaqueous Li–O2 Batteries," *J. Phys. Chem. Lett.*, vol. 4, pp. 2989–2993, 2013.

[40] P. G. Bruce, Y. Chen, L. Johnson, C. Li, Z. Liu, S. a Freunberger, M. M. Ottakam Thotiyl, and Z. Peng, "The Rechargeable Aprotic Lithium-O2 Battery," in *RS Spring Meeeting & Exhibit*, 2014.

[41] Innovative Technology, "Glovebox Glove Material Compatibility Guide," *Glovebox Glove Material Compatibility Guide - White Paper*. [Online]. Available: www.isolatorgloves.com/docs/Material-Compatibility.pdf.

[42] G. S. Chai, S. B. Yoon, J.-S. Yu, J.-H. Choi, and Y.-E. Sung, "Ordered Porous Carbons with Tunable Pore Sizes as Catalyst Supports in Direct Methanol Fuel Cell," *J. Phys. Chem. B*, vol. 108, no. 22, pp. 7074–7079, Jun. 2004.

[43] X. L. Wang, H. M. Zhang, J. L. Zhang, H. F. Xu, Z. Q. Tian, J. Chen, H. X. Zhong, Y. M. Liang, and B. L. Yi, "Micro-porous layer with composite carbon black for PEM fuel cells," *Electrochim. Acta*, vol. 51, no. 23, pp. 4909–4915, Jun. 2006.

[44] N. Tachikawa, K. Yamauchi, E. Takashima, J.-W. Park, K. Dokko, and M. Watanabe, "Reversibility of electrochemical reactions of sulfur supported on inverse opal carbon in glyme-Li salt molten complex electrolytes.," *Chem. Commun. (Camb).*, vol. 47, no. 28, pp. 8157–9, Jul. 2011.

[45] S. D. Beattie, D. M. Manolescu, and S. L. Blair, "High-capacity lithium--air cathodes," *J. Electrochem. Soc.*, vol. 156, no. 1, pp. A44–A47, 2009.

[46]   L. Wang, M. Ara, K. Wadumesthrige, S. Salley, and K. Y. S. Ng, "Graphene nanosheet supported bifunctional catalyst for high cycle life Li-air batteries," *J. Power Sources*, vol. 234, pp. 8–15, Jul. 2013.

[47]   X. H. Yang and Y. Y. Xia, "The effect of oxygen pressures on the electrochemical profile of lithium/oxygen battery," *J. Solid State Electrochem.*, vol. 14, pp. 109–114, 2010.

[48]   Y. Chen, S. A. Freunberger, Z. Peng, O. Fontaine, and P. G. Bruce, "Charging a Li – O 2 battery using a redox mediator," vol. 5, no. June, pp. 1–6, 2013.

[49]   R. R. Mitchell, B. M. Gallant, Y. Shao-Horn, and C. V. Thompson, "Mechanisms of morphological evolution of Li2O2 particles during electrochemical growth," *J. Phys. Chem. Lett.*, vol. 4, pp. 1060–1064, 2013.

[50]   M. Mirzaeian and P. J. Hall, "Characterizing capacity loss of lithium oxygen batteries by impedance spectroscopy," *J. Power Sources*, vol. 195, no. 19, pp. 6817–6824, Oct. 2010.

[51]   S. Rodrigues, N. Munichandraiah, and A. K. Shukla, "Review of state-of-charge indication of batteries by means of a.c. impedance measurements," *J. Power Sources*, vol. 87, pp. 12–20, 2000.

[52]   J. Adams, M. Karulkar, and V. Anandan, "Evaluation and electrochemical analyses of cathodes for lithium-air batteries," *J. Power Sources*, vol. 239, no. 0, pp. 132–143, Oct. 2013.

[53]   M. Eswaran, N. Munichandraiah, and L. G. Scanlon, "High capacity Li-O2 cell and electrochemical impedance spectroscopy study," *Electrochem. Solid-State Lett.*, vol. 13, no. 9, pp. A121 – A124, 2010.

[54]   J. Kumar and B. Kumar, "Development of membranes and a study of their interfaces for rechargeable lithium-air battery," *J. Power Sources*, vol. 194, no. 2, pp. 1113–1119, Dec. 2009.

[55]   L. O. L. Crystallization, R. Black, S. H. Oh, J. Lee, T. Yim, B. Adams, and L. F. Nazar, "Screening for Superoxide Reactivity in Li-O 2 Batteries : Effect on," *J. Am. Chem. Soc.*, vol. 134, pp. 2902–2905, 2012.

[56]   Z. Chan, F. Miao, Z. Xiao, H. Juan, and Z. Hongbing, "Effect of doping levels on the pore structure of carbon nanotube/silica xerogel composites," *Mater. Lett.*, vol. 61, no. 3, pp. 644–647, Feb. 2007.

[57] B. M. Gallant, R. R. Mitchell, D. G. Kwabi, J. Zhou, L. Zuin, C. V. Thompson, and Y. Shao-Horn, "Chemical and Morphological Changes of Li–O 2 Battery Electrodes upon Cycling," *J. Phys. Chem. C*, vol. 116, no. 39, pp. 20800–20805, Oct. 2012.

[58] D. Capsoni, M. Bini, S. Ferrari, E. Quartarone, and P. Mustarelli, "Recent advances in the development of Li-air batteries," *J. Power Sources*, vol. 220, pp. 253–263, 2012.

[59] E. J. Nemanick, "Electrochemistry of lithium–oxygen batteries using microelectrode voltammetry," *J. Power Sources*, vol. 247, pp. 26–31, Feb. 2014.

[60] A. Debart, J. Bao, G. Armstrong, and P. G. Bruce, "Effect of catalyst on the performance of rechargeable lithium/air batteries," in *ECS Transactions*, 2007, vol. 3, no. 27, pp. 225–232.

[61] A. Debart, J. Bao, G. Armstrong, P. G. Bruce, and A. Débart, "An O2 cathode for rechargeable lithium batteries: The effect of a catalyst," *J. Power Sources*, vol. 174, no. 2, pp. 1177–1182, Dec. 2007.

[62] A. Débart, A. J. Paterson, J. Bao, and P. G. Bruce, "Alpha-MnO2 nanowires: a catalyst for the O2 electrode in rechargeable lithium batteries.," *Angew. Chem. Int. Ed. Engl.*, vol. 47, no. 24, pp. 4521–4, Jan. 2008.

[63] Y.-C. Lu, Z. Xu, H. A. Gasteiger, S. Chen, K. Hamad-Schifferli, and Y. Shao-Horn, "Platinum-gold nanoparticles: A highly active bifunctional electrocatalyst for rechargeable lithium-air batteries," *J. Am. Chem. Soc.*, vol. 132, no. 35, pp. 12170–12171, 2010.

[64] J. L. Jespersen, A. E. Tønnesen, K. Nørregaard, L. Overgaard, and F. Elefsen, "Capacity Measurements of Li-Ion Batteries using AC Impedance Spectroscopy," *World Electr. Veh. J.*, vol. 3, pp. 1–7, 2009.

[65] A. Dobley, R. Rodriguez, and K. M. Abraham, "High Capacity Cathodes for Lithium-Air Batteries," in *Yardney Technical Products, Inc./Lithion, Inc. Pawcatuck, CT Electrochemical Society Conference,(May 20, 2004)*, 2004.

VIII.   Appendices

This section is used to group additional information that were not included in the rest of the document. Technical drawings, additional figures of data, sample table and practical experimental information can be found in this section.

i.   Equivalent circuit model

Electrochemical impedance spectroscopy can provide a tremendous amount of information about the dynamics of a specific electrochemical reaction without terminating a sample. EIS data can be collected at various times throughout the life of a battery with negligible effects on the cell. Thus, it is a very powerful technique to assess the health of the battery [64] and monitor reaction evolution [50]. By exposing it to a sinusoidal signal, the impedance response from the cell can be plotted as a Nyquist plot – real and imaginary impedances on the x- and y-axis, respectively and the battery can be modeled with an equivalent electrical circuit. Although the technique is quite insightful, modeling the equivalent circuit can be quite challenging and time consuming. In this section, an equivalent model is proposed for the samples used in this work. The three areas of focus shown in Figure 53 are discussed and associated with various factors of the battery.
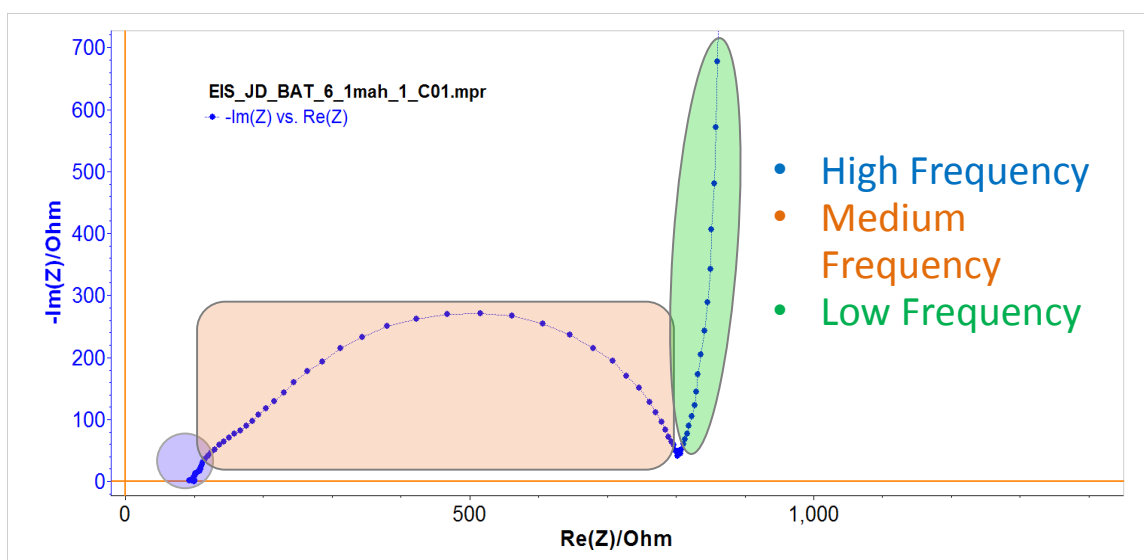

Figure 53: Nomenclature used in this paper to describe three areas of focus with EIS data: high frequency response, medium frequency response and low frequency response.

93

The high frequency response is mainly associated with static cell impedance. This includes the ohmic resistance of the cell and most importantly the ionic resistance of the electrolyte [51, 53], [60]. The medium frequency response mainly comprises of the effect between the carbon cathode and the electrolyte [51, 53]. Finally, the low frequency response corresponds to the diffusion rates associated with the lithium-oxygen cell [50]. Based on the results presented in the previous chapter and theoretical reaction mechanisms, each area of focus is modeled to better interpret the EIS data.

High frequency response

The ohmic resistance of the cell was characterized in an earlier chapter (section iii in Chapter III) to be a small fraction of the initial impedance experienced in the majority of the samples (a few ohms versus ~100 Ω). Thus, by definition, the initial impedance had to be related to the ionic resistance of the electrolyte. This was confirmed when variants were included in the electrolyte (refer to page 61). The last component that was investigated at high frequency was the consistent semi-circle present in all the tests at frequencies above 20 kHz. Since this was not discussed in the literature, variation in the cathode composition helped determine that this response was associated with the Toray paper current collector. Additional testing suggested it to be related to the interface between the carbon paper and the electrolyte (see page 68). The proposed model for this high frequency response can be found in Figure 54.
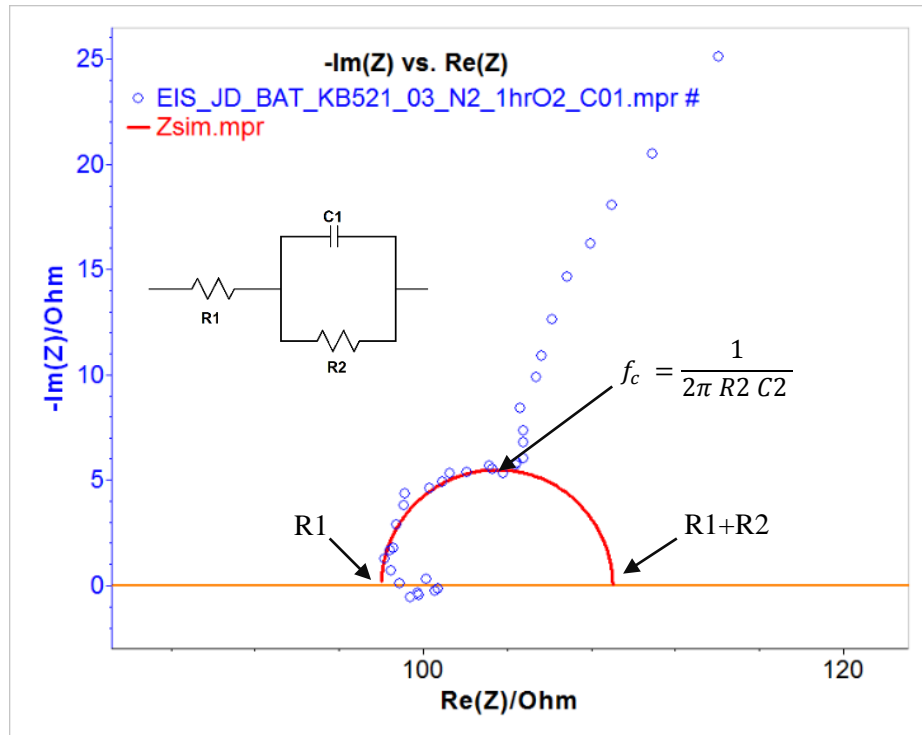
Figure 54: Simulated equivalent circuit for the high frequency response. INSET: equivalent electrical circuit

Medium frequency response

The medium frequencies of the whole spectrum is related to the interaction between the electrolyte and the electrodes [50]. The effect from the carbon morphology is not as distinctive as from the electrolyte composition. To confirm that, experimental testing varying both the carbon morphology and the electrolyte composition was pursued in this work (refer to page 61 for EIS data about the electrolyte composition). The morphology of the carbon material has been discussed in the literature to have an impact on the impedance spectrum of the cell [50]. Mirzaeian et al. discuss the effect of the pore size on the impedance and suggest that the pores and the surface area should be modeled separately [50]. Based on the literature [51, 53, 54], a graphical representation of an adapted equivalent circuit can be found in Figure 55. Note that the proposed model is an addition to the high frequency response model and the R1, R2 and C2 values are different in both models. Q2 is a constant phase element (CPE) that acts as a restricted capacitor. Finally,

W_d3 is a diffusion convection that affects the way both module interact between one-another.
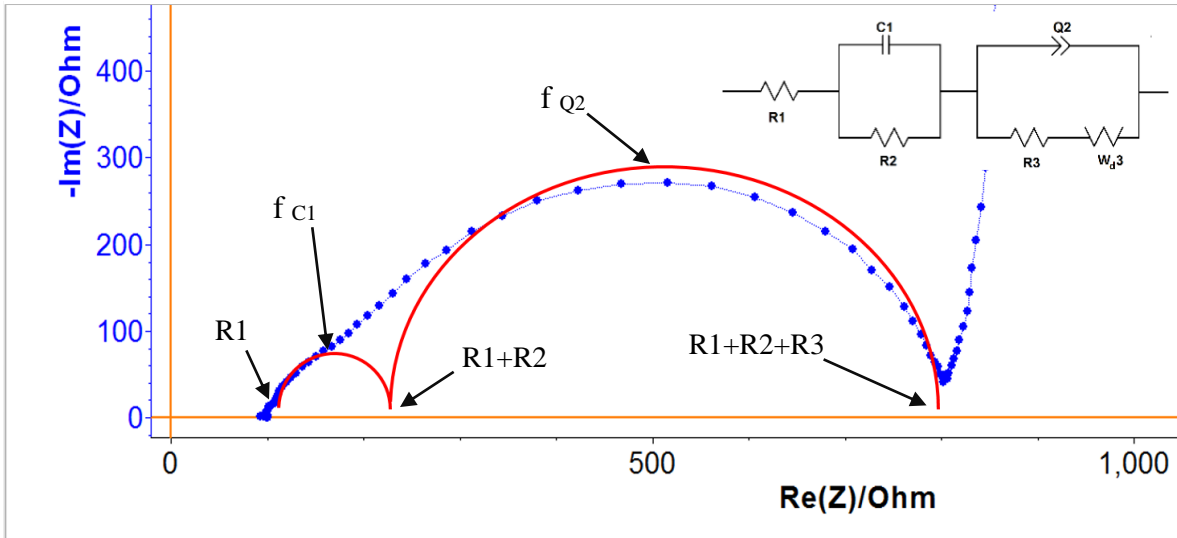

Figure 55: Graphical equivalent circuit for the medium frequency response. INSET: equivalent electrical circuit

The same circuit was modeled in the Biologic software and fitted to a random experimental result. Figure 56 shows a sample with the fitted model (INSET). The R-squared value showed above 0.99 for all the samples demonstrating an adequate model.
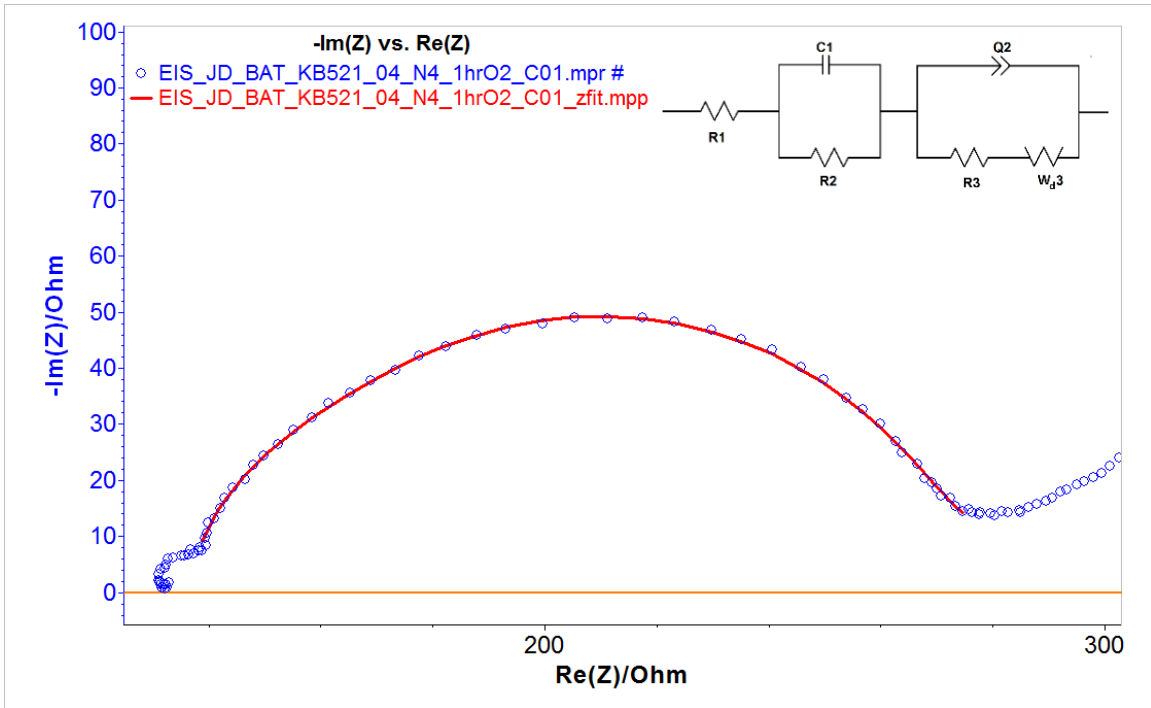
Figure 56: Medium frequency response equivalent model fitted to experimental data between 25 kHz and 25 Hz. INSET: equivalent circuit used for the model.

The proposed model showed good agreement with the experimental data; nonetheless, a number of other models could fit the experimental data similarly. Thus, a more elaborate equivalent circuit may be designed in future work to further detail the interaction between the electrolyte and the electrodes.

Low Frequency response

The impedance response at low frequencies (below 25 Hz) is often limited by the diffusion rates in the system. At those frequencies, the time for a full sinusoidal wave to occur is slow enough that capacitive charges are not affecting the cell and the charge transfer associated with diffusion rates become the limiting factors. As a result, a characterizing real and imaginary impedance increases at a relatively constant rate as the frequency is dropped. The diffusion characteristics can be found from where this trend starts and from the slope angle of the impedance [8]. In conventional batteries, the diffusion is solely associated with the ionic diffusion through the electrolyte between the two electrodes. From the data collected across the various cells, the trend shows a complex diffusion that

97

suggests an additional diffusion rate. Thus, this section focuses on a preliminary characterization of the diffusion rates in lithium oxygen cells with electrochemical impedance spectroscopy.

An equivalent circuit model proposed two diffusions rates in parallel to allow them to operate independently from each other. The model was then fitted to the experimental data of various cells to find a good agreement ($R^2 > 0.99$), as shown in Figure 57. This dual diffusion rate model has not yet been proposed in the literature for lithium oxygen batteries. Additional work is suggested to further investigate this complex diffusion rate prior to proposing an equivalent model for the full spectrum.
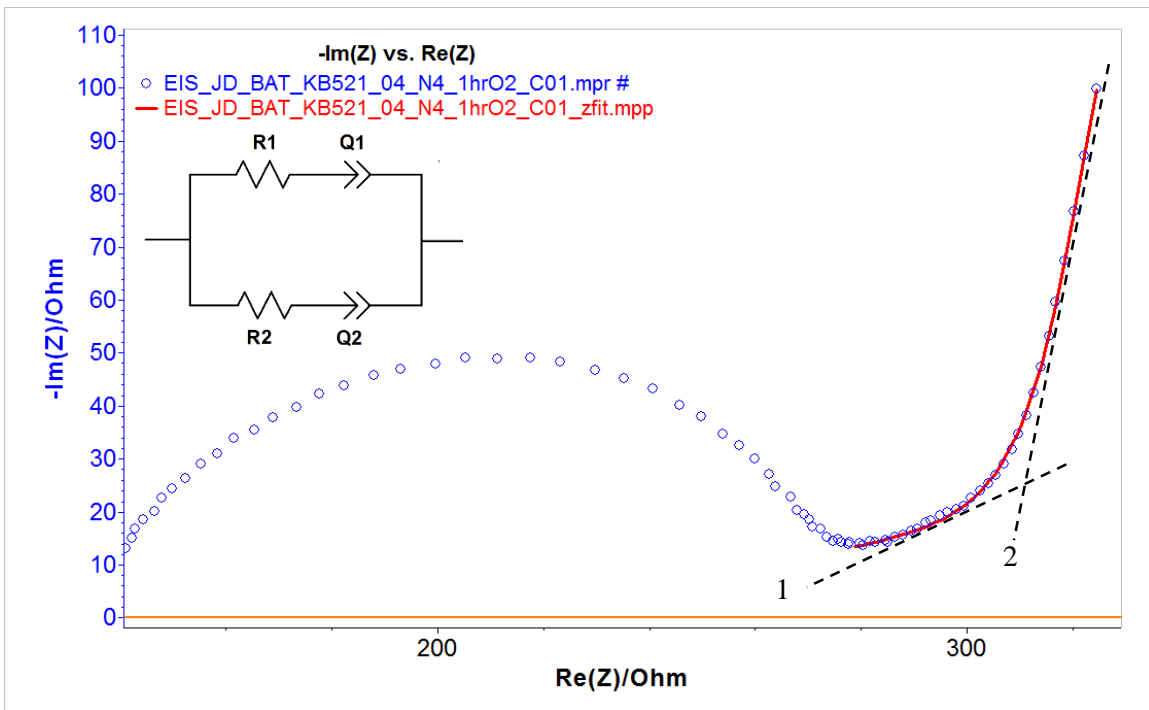

Figure 57: Low frequency response equivalent model fitted to experimental data under 25 Hz. INSET: equivalent circuit used for the model.

ii.   Airgas specification sheet

Pure Gases

Airgas.

Argon (Ar)

A colorless, odorless, nonflammable gas or a colorless, odorless, nonflammable cryogenic liquid.

Purity Specifications	Minimum Purity	O_2	H_2O	THC	CO	CO_2	N_2
BIP® Technology	99.9999%	< 10 ppb	< 20 ppb	< 100 ppb			< 5
Research Plus	99.9999%	< 0.1	< 0.2	< 0.1	< 0.1	< 0.1	< 0.8
Research	99.9997%	< 0.2	< 0.5	< 0.2	< 0.5	< 0.5	< 3
Ultra Pure Carrier (UPC)	99.9996%	< 0.5	< 0.5	< 0.3	< 1	< 1	< 5
Ultra High Purity (UHP)	99.999%	< 1	< 1	< 0.5	< 0.5*	< 0.5*	
Zero	99.998%	< 4	< 3	< 0.5			
Prepurified (PP)	99.998%	< 3	< 3				
High Purity (HP)	99.998%	< 4	< 3				
High Pressure/High Purity	99.999%	< 4	< 3				

Concentrations given are ppm by volume unless otherwise specified.

*CO + CO_2 < 1 ppm.

PRODUCT	Ordering Information					Equipment Recommendations		
	Cylinder Size	Contents (ft³)	Standard Valve Outlet (CGA)	Product Number	Cylinder Pressure at 70°F (psig)	Description Product Number	Delivery Pressure Range (psig)	Page Number
BIP® Technology	300	336	580	AR BIP300	2,640			
	Certificate of Conformance included.							
Research Plus	300	336	580	AR RP300	2,640	Two-Stage Regulators Y12-N145 *580 Y12-SR145 *580 Single-Stage Regulator Y11-N145 *580	A = 0-25 B = 0-50 D = 0-100 E = 0-150 F = 0-250	E14 E19 E13
	200	251	580	AR RP200	2,200			
	150A	152	580	AR RP15A	2,000			
	Total impurities guaranteed < 1 ppm. Individual Certificate of Analysis included.							
Research	300	336	580	AR R300	2,640			
	200	251	580	AR R200	2,200			
	150A	152	580	AR R15A	2,000			
	80	99	580	AR R80	2,200			
	35	39	580	AR R35	2,200			
	Total impurities guaranteed < 3 ppm. Individual Certificate of Analysis or rigorous application of SPC provided upon request.							
Ultra Pure Carrier (UPC)	300	336	580	AR UPC300	2,640			
	200	251	580	AR UPC200	2,200			
	80	99	580	AR UPC80	2,200			
	35	39	580	AR UPC35	2,200			
	An individual or batch analysis is available upon request at a nominal charge. Certificate of Conformance provided upon request.						* Insert Delivery Pressure Range Code	
Ultra High Purity (UHP)	300	336	580	AR UHP300	2,640	Two-Stage Regulator Y12-244 * 580 Single-Stage Regulator Y11-244 * 580	A = 0-25 B = 0-50 D = 0-100 E = 0-150 F = 0-250 G = 0-500**	E11 E10
	200	251	580	AR UHP200	2,200			
	80	99	580	AR UHP80	2,200			
	35	39	580	AR UHP35	2,200			
	An individual or batch analysis is available upon request at a nominal charge. Certificate of Conformance provided upon request.							
Zero	300	336	580	AR Z300	2,640			
	200	251	580	AR Z200	2,200			
	80	99	580	AR Z80	2,200			
	35	39	580	AR Z35	2,200			
	An individual or batch analysis is available upon request at a nominal charge. Certificate of Conformance provided upon request.						* Insert Delivery Pressure Range Code ** Single Stage Only	

BIP® purifier technology is an PRODUCTS innovation.
BIP® is a registered trademark of Air Products and Chemicals, Inc.
(US Trademark 2,521,752).
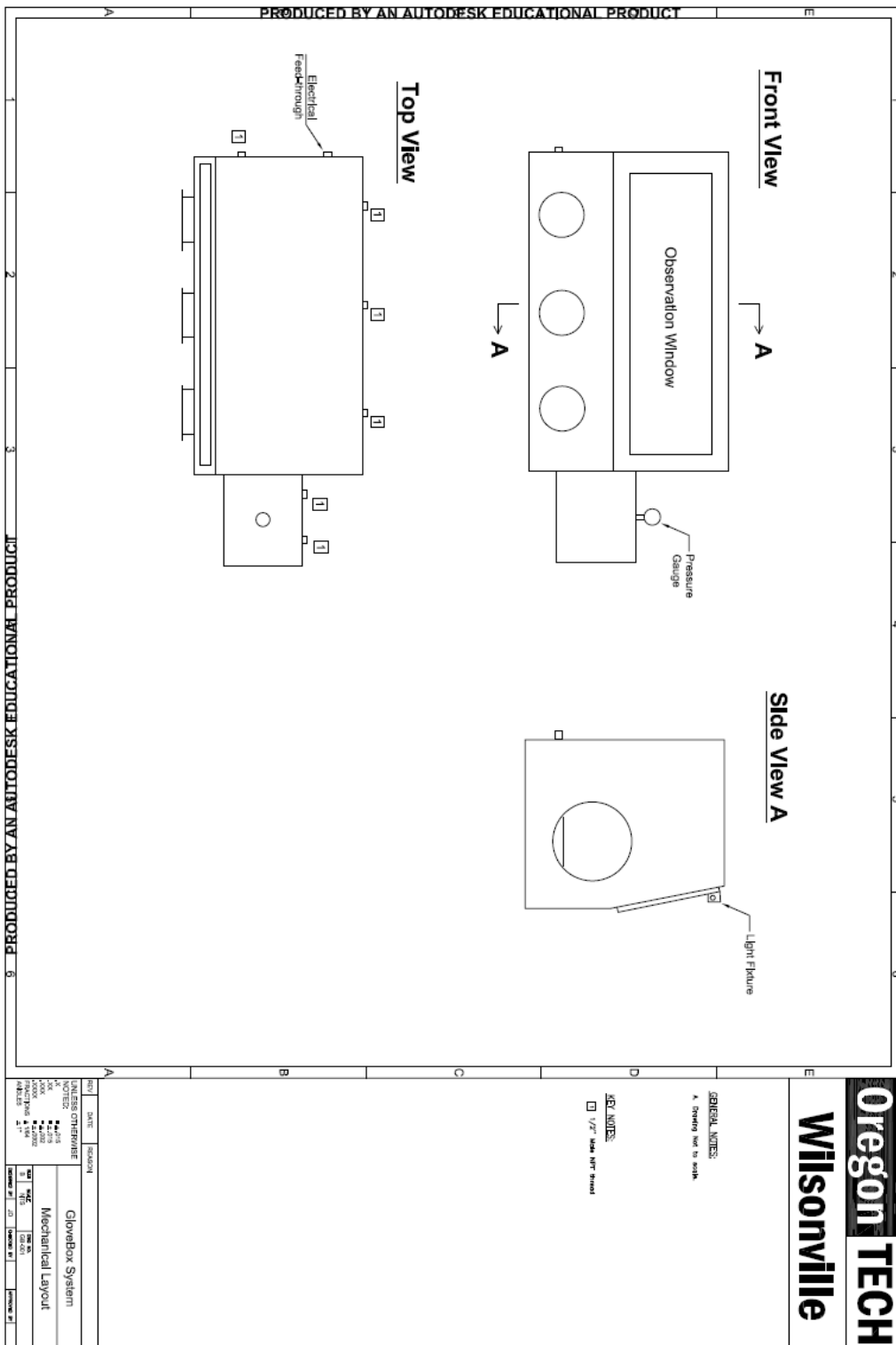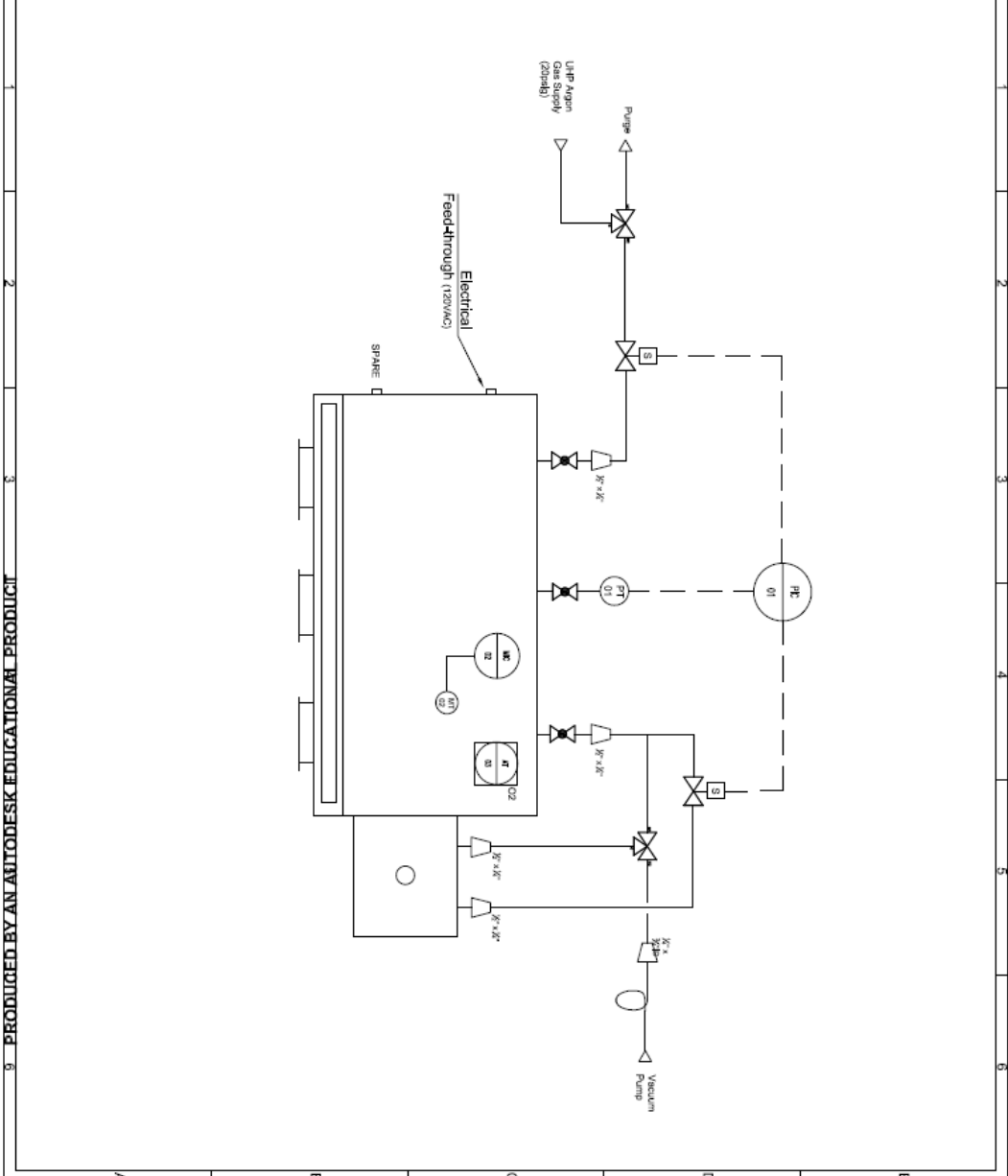BIP® purifier technology is protected by US patent no. 0591840.

www.airgas.com

99

iii.   Sample matrix for titration

1st disch.	Sample 1	Sample 2	Sample 3
Graphene	Graph505-01-N1 67.9 %	Graph505-02-N1 69.5 %	Graph505-03-N8 67.1 %
CNT	CNT505-01-N2 71.2 %	CNT521-01-N7 68.1 %	CNT605-01-N5 72.3 %
XC72	XC72505-02-N3 69.9 %	XC72521-03-N2 72.7 %	XC72521-01-N3 70.2 %
KB	KB505-01-N4 73.7%	KB505-03-N3 73.4 %	KB521-04-N4 71.1 %
AB	AB505-01-N5 71.4 %	AB505-02-N5 73.9 %	AB505-03-N6 70.8 %

3rd disch.	Sample 1	Sample 2	Sample 3	Sample 4
Graphene	Graph509-01-N8 38.2 %	Graph509-03-N6 36.4 %	Graph521-01-N6 44.8 %	
CNT	CNT505-03-N1 28.9 %	CNT505-02-N2 34.7 %	CNT521-02-N8 41.9 %	CNT605-01-N5 54.3 %
XC72	XC72509-01-N6 39.1 %	XC72509-02-N8 45.1 %	XC72521-03-N6 36.0 %	XC72521-02-N5 38.2 %
KB	KB509-01-N3 35.1 %	KB509-03-N5 37.4 %	KB509-02-N4 45.7 %	
AB	AB505-04-N8 31.8 %	AB509-01-N6 39.9 %	AB505-0b-N7 49.3 %	

iv.   Technical drawings

Oxygen Service Only:

This system has been designed with components that are UHP-oxygen-rated for safety purposes. Modifications must be made with care.

Oregon TECH
Wilsonville

GloveBox System

Oxygen Supply System

v.   First discharge voltage profile by carbon material

Discharge Profile of Graphene nanoplatelets

Discharge Profile of Carbon Nanotubes

Discharge Profile of Volcan XC72

Legend:
- XC72505-01-N3
- XC72505-02-N3
- XC72505-03-N2
- XC72521-01-N3

Y-axis: Voltage [V]
X-axis: Specific Capacity [mAh/gcarbon]

Discharge Profile of KB Carbon

Legend:
- KB505-01-N4
- KB505-02-N4
- KB505-03-N3
- KB505-02-N3

Y-axis: Voltage [V]
X-axis: Specific Capacity [mAh/gcarbon]

Discharge Profile of AB Carbon

vi.   Relevance of cathode preparation

Composition of the cathode has been demonstrated to have a great effect on the performance of the battery. Furthermore, the process of layering the carbon onto a current collector can also have an effect on the battery. Experimental data showed that testing cathodes that were slightly cracking would not provide accurate and repeatable data. The foremost observation is the discharge cycle of a cracked cathode. A CNT sample was assembled to acquire data over three consecutive cycles and after which to quantify lithium peroxide yield. The following figure shows the first discharge cycle.
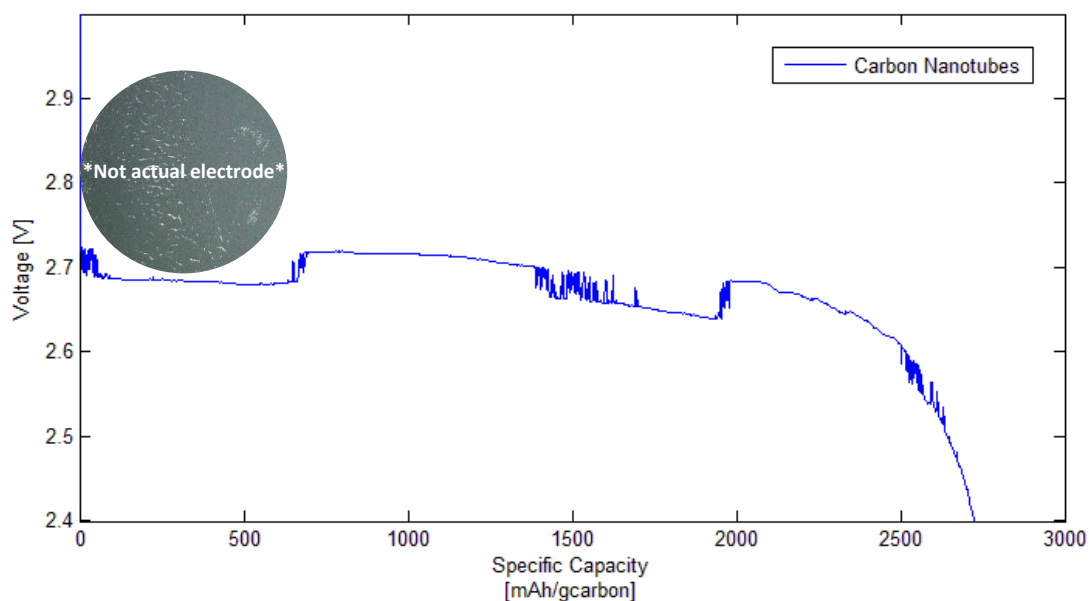
Figure 58: Discharge cycle of a cracked cathode illustrating the sporadic connection to the current collector.

As observed in the figure, rapid change in the voltage magnitude occurs throughout the discharge. The suggested hypothesis for this abnormal behavior is related to observing relatively high cracking on the cathode before assembling it. Due to a lack of time and available cathodes, this non-optimum sample was assembled to acquire one more data point on the titration plot. Although not titrated for obvious reasons, this sample raised an important concern on the integrity of the cathode. The cracking on the deposited layer may not provide a good electron path during cycling. Furthermore, build-up of lithium peroxide may form on a detached section of carbon and lose its electron path during charging cause the peroxide not to be recycled. This bring erratic data when titration is performed on a later cycle since lithium peroxide may not have been cycled three times (i.e. lithium peroxide might be from the first discharge).